Power uprates
and plant life extension

CASL-U-2012-0045-000

Consortium for Advanced Simulation of LWRs

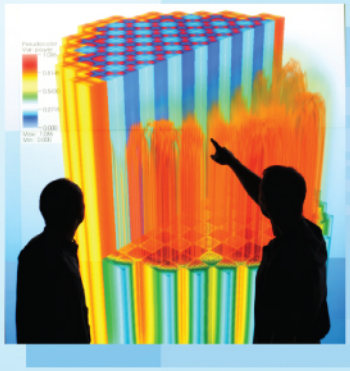

Engineering design
and analysis

Proof-of-Concept of DeCART/STAR-CCM+/MAMBA Coupled Simulation for the Prediction of Crud Deposition on a Fuel Pin with Grid Spacers

Science-enabling
high performance
computing

Brian Kendrick, Los Alamos National Laboratory
Dan Walter, University of Michigan
Ben Collins, University of Michigan
Victor Petrov, University of Michigan
Annalisa Manera, University of Michigan
Thomas Downar, University of Michigan

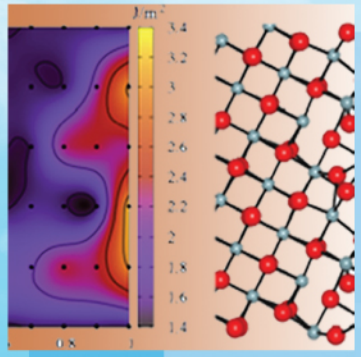

Fundamental science

January 20, 2012

Plant operational data

U.S. DEPARTMENT OF ENERGY | Nuclear Energy

Consortium for Advanced Simulation of LWRs

Consortium for Advanced Simulation of Light Water Reactors
Bldg. 2040, Room E-170, MS 6290
P.O. Box 2008
Oak Ridge, TN 37831-6290
Email: casl-info@ornl.gov

Proof-of-concept of DeCART/STAR-CCM+/MAMBA Coupled Simulation for the prediction of crud deposition on a fuel pin with grid spacers

by

Brian Kendrick, Los Alamos National Laboratory
Dan Walter, University of Michigan
Ben Collins, University of Michigan
Victor Petrov, University of Michigan
Annalisa Manera, University of Michigan
Thomas Downar, University of Michigan

CASL-U-2012-0045-000

Introduction

Optimal PWR performance relies on the consideration of a variety of design parameters, risk assessments, constraints, and trade-offs. One of the most important risk assessments is for CIPS (Crud Induced Power Shift) also known as AOA (Axial Offset Anomaly). CIPS originates from an axially asymmetric boron deposit which resides in the crud layer coating the surfaces of the fuel rods. The asymmetry in the boron concentration along the axial direction is directly correlated with the increase in the crud thickness along the axial direction. The crud deposit is typically thicker on the upper regions of the fuel rods due to the higher temperature of the surrounding coolant and the fuel rods with highest power (heat flux) are typically the ones with the thickest crud. A typical crud layer observed in a PWR is shown in Figure 1.

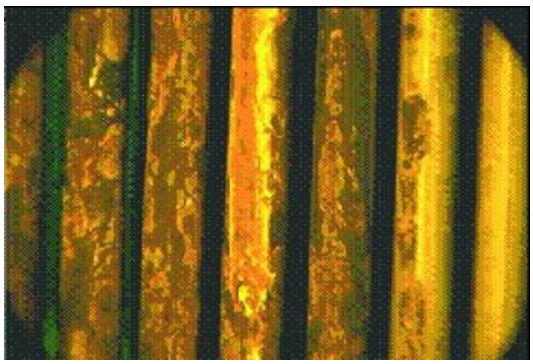

Figure 1 Typical crud loading in a PWR (NEI, 2012)

The boron concentration within the crud layer increases with increasing crud thickness due to the higher cladding temperatures and increased internal boiling within the crud layer. The increased boiling inside the crud draws in boric acid from the coolant, which subsequently precipitates and deposits within the pores of the crud, most often in the form of lithium tetraborate ($Li_2B_4O_7$). The highly concentrated boron within the thicker crud layers reduces the neutron flux in those regions which can then lead to a significant axial power shift (CIPS). The risk for CIPS increases with power uprates and longer cycles due to the increased potential for thicker crud deposits. Variations in coolant chemistry (Li, B, H_2, pH, etc.) can also increase or decrease the potential for CIPS. The concentrations of Ni and Fe in the coolant due to the corrosive release from other ex-core surfaces (such as steam generator tubing) directly impact the rate of crud growth and therefore the risk for CIPS. A coupled simulation approach including crud growth, thermal hydraulics and neutronics is required in order to treat the complex coupled physics and chemistry associated with CIPS. Coupled simulation capabilities will improve the risk assessment for CIPS resulting in optimized PWR performance.

This report documents the completion of an initial advanced (pin scale) multiphysics simulation by coupling the results of three different computer codes: MAMBA (crud), DeCART (neutronics), and STAR-CCM+ (thermal hydraulics) in fulfillment of the CASL Milestone L1.CASL.P4.02:

> "Conduct a CRUD investigation on representative clad surface regions within a 3D subassembly configuration using baseline VERA capabilities, and compare to higher

> resolution analysis (pin scale) using initial advanced and advanced VERA capabilities. Base the subassembly analysis on a relevant reactor environment and assess the resulting CIPS risk due to phenonemona such as asymmetric boron uptake".

The primary goals (completion criteria) for this L1 milestone were the following:

> "Complete an initial demonstration simulation for a 3D subassembly of a 3x3 pin geometry. Minimum is baseline: ANC/VIPRE/BOA + MAMBA, initial advanced (pin scale) is DeCART/STAR-CCM+/BOA/MAMBA, and advanced is Denovo/Hydra3D/BOA/MAMBA. Compute thickness/composition of crud layer, temperature, heat flux in/out, and boron distribution within the crud layer along the surface (or selected surface regions) of a single pin within the 3x3 pin geometry. An initial integration of 3D MAMBA v2.0 into VERA will be implemented. "Optional (desired) result: "The initial demonstration simulation for a 3x3 include couplings between MAMBA and BOTH CFD (STAR-CCM+) and neutronics (DeCART)."

In summary, both the primary and optional goals of this L1 have been met using the initial advanced (pin scale) coupled DeCART/STAR-CCM+/MAMBA multiphyiscs simulation approach. A preliminary two-way coupling between each of the three codes has been implemented and applied to the assessment of CIPS risk for a 3D geometry consisting of a single fuel rod with three spacers (each spacer contains four mixing vanes). This particular geometry was chosen for the initial proof-of-principle coupled demonstration simulation in order to minimize the computational requirements and to focus on the physics and the coupling interfaces. Future studies will include the treatment of additional spacers and multiple fuel rods within a larger sized sub-assembly (i.e., a 4x4 pin geometry), as well as the development of a more sophisticated coupling interface between the codes.

The crud thickness and boron uptake within the three-dimensional crud layer along the entire surface of the pin was computed as a function of time by the MAMBA 3D v2.0 computer code. The cladding surface heat flux, crud surface temperature, and the surface turbulent kinetic energy required by MAMBA were computed by a coupled DeCART/STAR-CCM+ calculation. The resulting 3D boron distribution computed by MAMBA was used by DeCART to assess the effects of the boron layer on the power distribution along the length of the pin (i.e., the CIPS risk). The coupling (data exchanges) between the three codes was initiated at 25 and 50 day time intervals extending over a 400 day cycle. A high-resolution ("zoomed in") MAMBA/STAR-CCM+ coupled simulation for the region around the first spacer grid was also performed.

Interesting azimuthal variations due to the mixing vanes were observed. The swirling/turbulent flow through the mixing vanes leads to significant azimuthal temperature variations on the cladding surface as well as to increased surface erosion of the crud layer. Both of these fluid-induced effects alter the local crud deposition rate and thickness, giving rise to "streak" deposits which have been observed in operating PWRs. "Hot spots" on the cladding surface were also observed in regions of thicker crud deposits which increases the risk for CILC (Crud Induced Localized Corrosion). The preliminary results from this study demonstrate the importance of a coupled simulation approach for capturing observed reactor core phenomena leading to CIPS and

CILC and mostly importantly for improving the risk assessment of these industrial relevant effects.

The report is organized as follows. The next section will review some of the basic multiphysics phenomena which require the use of coupled codes for modeling crud deposition and describe the strategy used for coupling and iterating between the DeCART, STAR-CCM+, and MAMBA codes. Subsequent sections will describe the model used to demonstrate the coupling and the simulation, and the results will then be presented sequentially for CCM+, MAMBA, and DeCART. The final section will summarize the results and discuss future work.

Crud Deposition Modeling with DeCART/STAR-CCM+/MAMBA

Modeling of crud deposition requires the accurate prediction of axial and azimuthal distributions of power and cladding temperature, as well as the accurate modeling of the swirling induced by the grid spacers. Furthermore, the accurate description of crud erosion also requires detailed information about the local turbulent kinetic energy or shear stresses at the cladding surface. The feedback between the neutronics and thermal-hydraulics field solutions on the crud deposition is depicted in Figure 2.

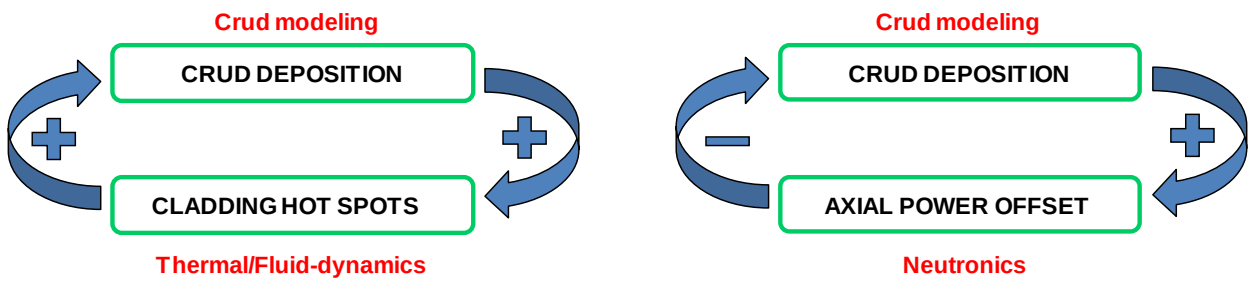

Figure 2 Feedback mechanisms between crud modeling and thermal/fluid-dynamic (left) and neutronics (right) parameters.

The presence of hot spots on the cladding surface triggers the deposition of crud, which in turn yields an increase of the thermal resistance between cladding and coolant. This leads to an increase of the cladding temperature at the location where crud has already been depositing, causing more crud deposition at the same location. In other words, a positive feedback exists between formation of hot spots on the cladding surface and crud deposition. An additional thermal-hydraulic feedback not illustrated in Figure 2 is caused by the shear stress (or turbulent kinetic energy) in the proximity of the cladding surface. This quantity is positively correlated to the erosion of the crud surface. On the other hand, where the turbulent kinetic energy is high, good heat transfer conditions between cladding and coolant are established, so that crud erosion is high at locations where crud deposition is generally low because of good cladding coolability. The combination of these two positive thermal-hydraulic feedback mechanisms have a strong contribution to the classical striping patterns of crud deposition observed downstream from grid spacers. Conversely, the neutronics provides a negative feeback. Because of the neutron absorbers present in the crud, the deposition of crud on the cladding surface yields a local decrease of the power. A decrease of the local power will lead to a decrease of the local cladding

temperature and thus to less crud formation. Therefore in contrast to the thermal-hydraulic feedback, the feedback from the neutronics is negative.

Accurate modeling of the phenomena involved in crud deposition requires the use of high fidelity, multiphysics codes such as CFD (RANS) modeling for high fidelity spatial thermal-hydraulic representation and a neutron transport code for high fidelity spatial pin power predictions. In order to demonstrate high fidelity crud modeling, a preliminary coupling between MAMBA, DeCART, and STAR-CCM+ was developed using a sequence of three separate two-way coupling interfaces.

- **DeCART/STAR-CCM+**

  In this coupling interface DeCART provides STAR-CCM+ with the volumetric heat rate in the fuel pin for each CFD mesh, while STAR-CCM+ supplies DeCART with fuel temperature and fluid density distributions for each neutronics mesh. This coupling interface with DeCART acting as the interface master for the data exchange, was previously implemented and demonstrated within the LIME environment. However, depletion had not previously been performed when using the LIME interface, so an offline coupling was used between DeCART and STAR. During the depletion, the temperatures and power densities were exchanged and iterated upon until converged. In the future, the coupling will be performed using LIME.

- **STAR-CCM+/MAMBA**

  In this coupling interface MAMBA provides the additional thermal resistance between the cladding and fluid introduced by the crud formation on the cladding surface. The crud thermal resistance is a function of the thickness of the crud layer and the crud thermal conductivity. The accumulation of a crud layer on the cladding surface has also an influence on the wall roughness. This effect is however not taken into account in the current investigation. Future studies will be performed in order to analyze the importance of this effect on the thermal-hydraulic predictions. STAR-CCM+ provides the heat flux, the cladding temperature and the fluid temperature distributions needed for the calculation of the crud growth. The turbulent kinetic energy in the proximity of the cladding surface needed for the estimation of the crud erosion is also provided.

  The STAR-CCM+/MAMBA interface is currently not implemented within LIME. It is foreseen, however, that in the final implementation MAMBA will act as the interface master for data files exchange. In the present work, the data exchange between the two codes was performed manually.

- **DeCART/MAMBA**

  In this coupling interface MAMBA provides the boron concentration in the crud, the crud thickness and its composition (in the current implementation both the $NiFe_2O_4$ concentration and boron concentrations are provided. Other relevant species will be added in the future). At present no information is passed from DeCART to MAMBA, however it is planned to implement a data exchange for the computed boron destruction

rate due to neutron absorption. The DeCART/MAMBA interface is currently not implemented within LIME. It is foreseen, however, that in the final implementation DeCART will act as the interface master for data files exchange. In the present work, the data exchange between the two codes has been performed manually.

The overall coupling of DeCART/STAR-CCM+/MAMBA for this preliminary demonstration is shown in Figure 3.

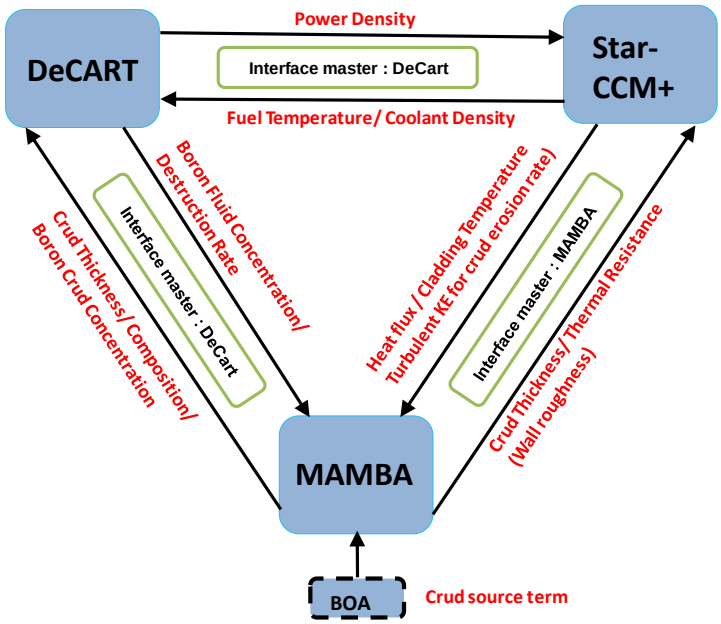

Figure 3 Coupling components and data exchange

Coupled Code Iteration Scheme

The coupling between DeCART and STAR-CCM+ was developed and described in a previous CASL milestone (Kochunas, 2012). As illustrated in Figure 4, the current scheme is simply a fixed-point Gauss-Seidel iteration in which the I/O data transfer between the two codes is based on the exchange of data files. At each iteration, DeCART updates the fuel power density distribution on the basis of the fuel temperatures and coolant density distributions computed by STAR-CCM+.

Next the STAR-CCM+ solution is updated on the basis of the fuel power density distribution supplied by DeCART. The iterations between the two codes continue until a user defined convergence criterion is satisfied, i.e. when the power computed by DeCART does not change beyond a specified convergence threshold after updating the STAR-CCM+ fluid-dynamic solution.

In the coupling between DeCART/STAR-CMM+/MAMBA, at first the initial steady-state is computed by iterating between DeCART and STAR-CCM+ (see Figure 5). At this point,

information on the cladding temperature, heat flux and turbulent kinetic energy in the proximity of the cladding surface are passed to the MAMBA code. MAMBA is then used to calculate the formation of crud at 25 day and 50 day time intervals. The information at these two time steps is used to update the crud composition for the DeCART depletion calculation. The depletion calculation is performed assuming a quasi-static approximation (i.e. fixed temperature fluid solution).

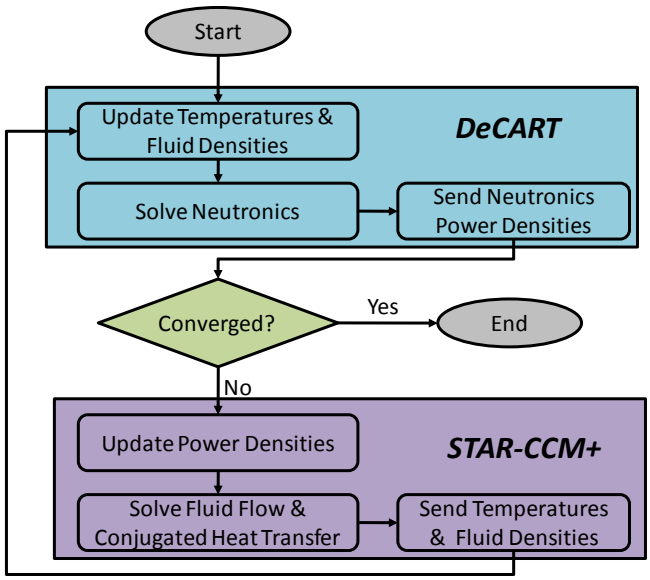

Figure 4 Coupled fixed point Gauss-Seidel iteration (Kochunas, 2012)

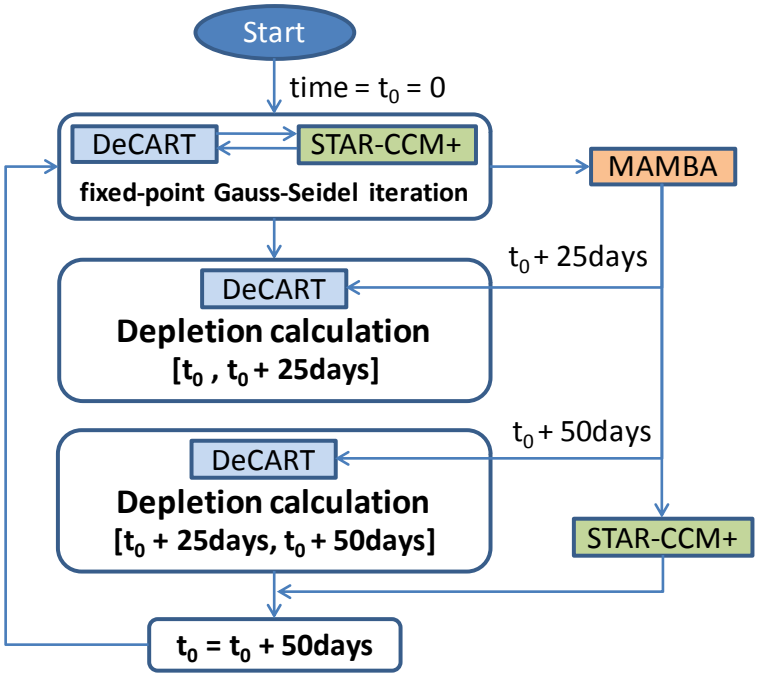

Figure 5 Coupling components and data exchange

Once the depletion calculation is completed over a time interval of 50 days, the MAMBA crud information is used to update the fluid-dynamic solution computed by STAR-CCM+. A new

time-step cycle is initiated using another new fixed-point Gauss-Seidel iteration between DeCART and STAR-CCM+. The results obtained over a total time interval of 400 days are presented in the results section. In future work, a more complex iteration procedure will be developed and implemented between MAMBA and the CFD/neutronics, to include a more sophisticated time stepping algorithm which is based on the time evolution of relevant physical parameters.

Description of Test Problem Models

For the purposes of the initial demonstration, a typical PWR pin cell test problem was developed with fixed inlet flow and temperature conditions. As shown in Figure 6, three grid spacers were modeled in the upper regions of the pin. The model parameters are as follows:

Pin radius	0.4025 cm
Clad radius	0.4759 cm
Active fuel height	365.76 cm
Pin Enrichment	4.9 w/o
Inlet velocity	5.278m/s
Inlet Temperature	556.76K
Pressure	15.51 MPa
Boron concentration	1600 ppm

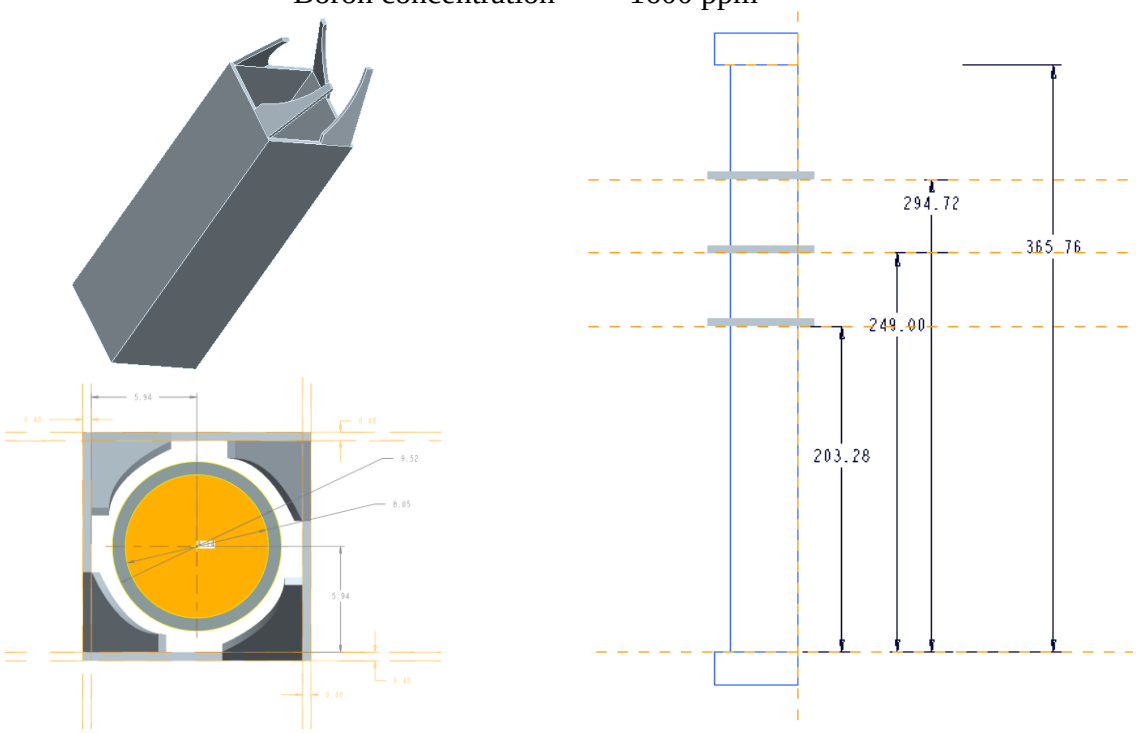

Figure 6 Pin cell model

Models of the pin cell were developed for each of the codes, STAR-CCM+, DeCART, and MAMBA. Each of the following subsections will provide a brief description of the codes and some of the details of the pin cell model.

Star-CCM+ Thermal-Fluids Model

STAR-CCM+ is a commercial computational fluid dynamics (CFD) code that solves the transport equations for continuity, 3-D momentum, and enthalpy on a very fine 3-D mesh. STAR-CCM+ is capable of modeling conjugate heat transfer, such that the conduction process is modeled within the fuel pellet and cladding and the convective heat transfer is modeled in the cooling fluid that surrounds the pin. There are several options for modeling turbulent momentum and energy transport available in STAR-CCM+. The Reynolds-Averaged Navier-Stokes (RANS) approach for the solution of the k-ε transport equations was used in the work here for turbulence modeling.

The CFD domain includes the model of the solid structure constituting the fuel pellet and cladding, the water domain in the subchannel surrounding the fuel pin, and the grid spacers. Inlet velocity and pressure boundary conditions were imposed for the inlet and outlet axial planes of the coolant domain respectively. Symmetric boundary conditions were imposed on the lateral surfaces of the water domain (coolant subchannel). No-slip conditions were imposed on the spacers walls and on the cladding surface. A volumetric power source was used in the fuel domain. The coolant density was calculated according to the following third-order polynomial:

$$\rho(T) = -0.0000116905 \cdot T^3 + 0.01225 \cdot T^2 - 4.84697 \cdot T + 1670.325859$$

A detailed representation of the boundary conditions is shown in Figure 7.

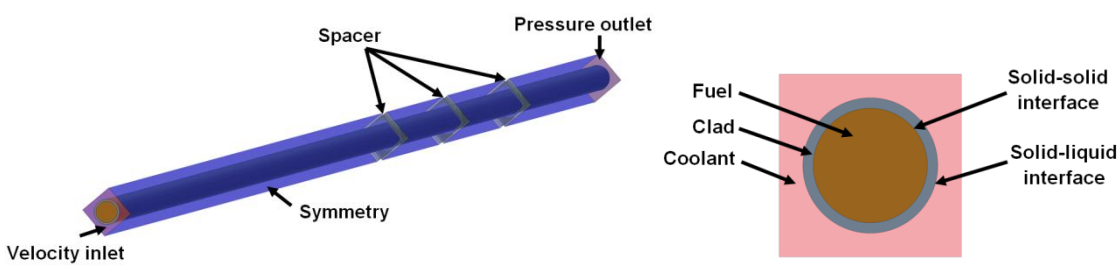

Figure 7 CFD model configuration

The realizable k-ε was used for the modeling of turbulence. The fluid-dynamic simulation included conjugate heat transfer for the calculation of the temperature distribution in the fuel and cladding domains.

Table 1 - Summary of CFD model elements by region

Region	Cells	Faces	Vertices
Fluid	776,970	3,401,427	2,283,715
Fuel	430,803	2,642,496	2,214,928
Fuel Rod Cladding	454,521	1,915,847	1,371,250
Total	1,662,294	7,959,770	5,869,893

The CFD domain was meshed by means of polyhedral cells. The grid spacer regions were discretized using polyhedral cells together with three layers of prismatic cells at the wall. The computational mesh upstream and downstream of grid spacers was generated by extrusion, applying the hyperbolic tangent law. Solid-solid and solid-liquid interfaces were kept conformal.

The data exchange between MAMBA and STAR-CCM+ was performed via ASCII files. The ASCII file generated by STAR-CCM+ and passed to MAMBA includes XYZ tables for the crud layer surface temperature, the cladding surface temperature (below the crud layer), the turbulent kinetic energy in the boundary layer and the surface heat flux. The ASCII file generated by MAMBA and passed to STAR-CCM+ includes a XYZ table for the crud thickness and thermal resistance between cladding surface and coolant introduced by the crud layer. The thermal resistance provided by MAMBA was mapped at the solid-fluid interface using the Star-CCM+ XYZ table tool. The origin of the coordinate system for both codes (MAMBA and Star-CCM+) is located in the center of the fuel pin at the inlet section. A summary of the mesh size is shown in Table 1. Details of the CFD mesh are shown in Figure 8.

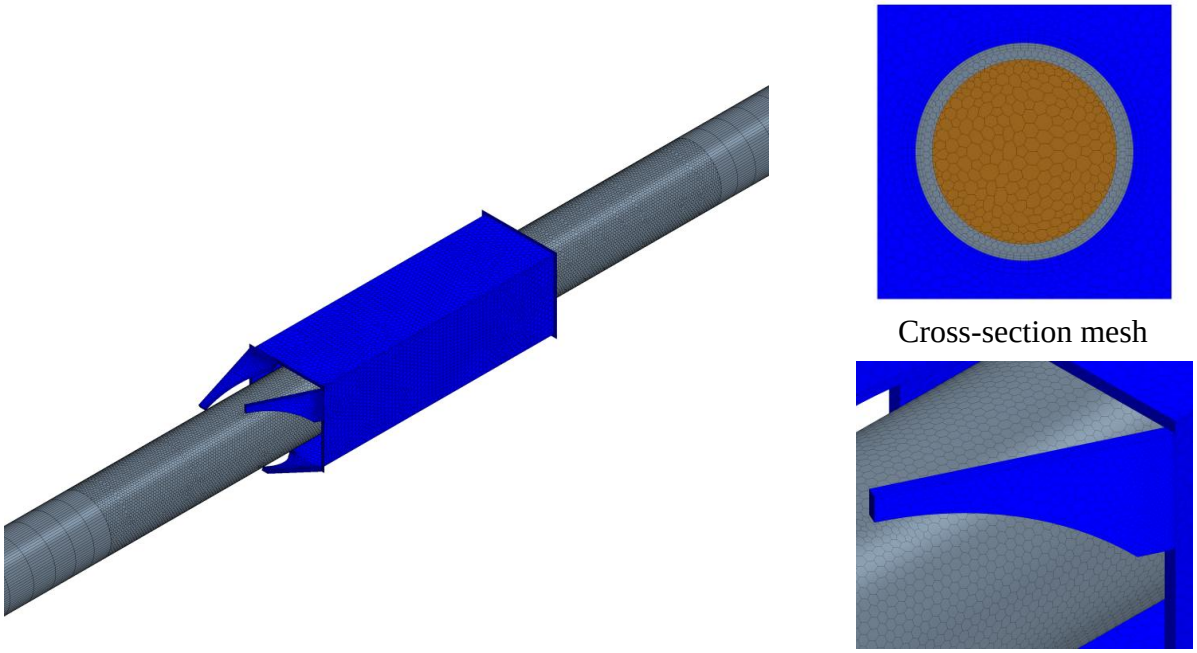

Cross-section mesh

Spacer region

Zoomed vane

Figure 8 CFD mesh

DeCART Neutronics Model

DeCART (Deterministic Core Analysis based on Ray Tracing) is a whole core neutron transport code capable of direct sub-pin level flux calculation at power generating conditions of a LWR. It requires neither a priori homogenization nor group condensation as needed in conventional reactor physics calculations. DeCART solves the three-dimensional neutron transport problem employing a 2D-1D method in which the planar solution is performed using the Method of Characteristics (MOC) solutions and the axial solution is performed using the Nodal Expansion

Method (NEM) based kernel. The DeCART code has various computational capabilities to solve not only the steady state eigenvalue problems but also the transient fixed source problems. The steady state calculation can be performed in various modes which may consist of a criticality search, branch restart, and/or depletion. The depletion calculation is performed using the predictor/corrector method and has been well validated for a wide range of PWR and BWR applications. More details can be found in [Hursin et al., 2010].

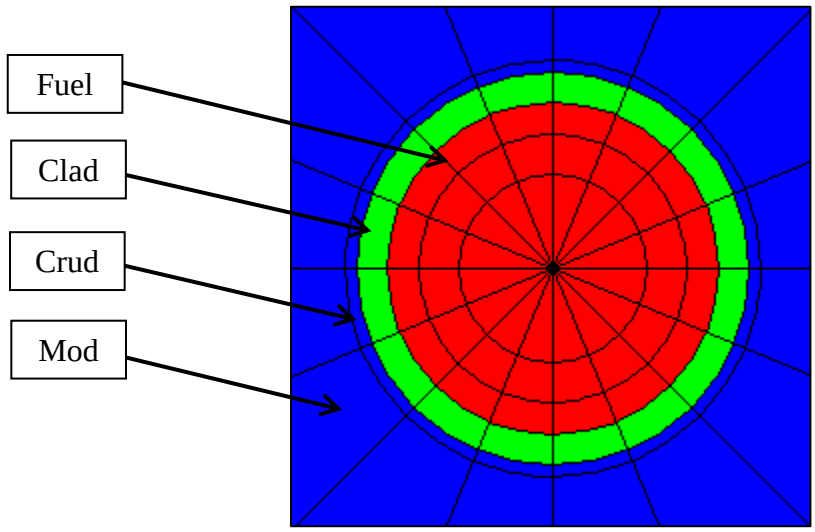

Figure 9 DeCART pin cell model showing radial ring reserved for crud

The DeCART pin cell model consists of a 3D pin of length 405.76 cm with an active fuel height of 365.76 cm. A 20 cm water reflector is at each end. The side boundary conditions are reflective, while the axial boundary conditions are vacuum. Figure 9 shows the pin cell geometry with all flat source regions explicitly shown: 48 within the fuel and 16 within each the cladding, crud region and moderator region. The outermost radial division is a region that is initially filled with moderator and is reserved for crud; the crud is deposited after input processing.

Two different boron cases were run: (1) boron concentration set to 1600 ppm throughout all 400 days, and (2) a boron letdown curve beginning at 1200 ppm and ending at 0 ppm at 400 days. All STAR-CCM+ (Figure 16 to Figure 21 and Appendix 1) and MAMBA (Figure 22 to Figure 32) results presented in the chapters "STAR-CCM+ results" and "MAMBA results" respectively have been obtained for a constant boron concentration of 1600 ppm (case 1). The DeCART results for case 2 were obtained with a boron letdown curve of 1200 ppm at beginning of cycle and 0 ppm at 400 days. The letdown data is shown in Table 2 and plotted in Figure 10.

The crud composition of nickel ferrite ($NiFe_2O_4$) and boron were provided to DeCART by MAMBA in three-dimensional space along the length of the fuel rod. DeCART was modified to read the crud data, and then deposit the crud mixture in the appropriate locations along the cladding surface. The crud data (concentration and location) mapping from MAMBA to DeCART was performed in the same manner as the temperature/fluid mapping was performed from STAR-CCM+ to DeCART. The radial DeCART mesh for the pin cell is shown in Figure 9 and in Figure 11. The outermost radial division is reserved for the crud deposition and is set to 300 microns in this study. The crud deposition is azimuthally dependent (see Figure 11) and the

crud concentration varied circumferentially around the rod. Within the each region in which the crud is deposited, it displaces the moderator and the remaining mixture is homogenized within the 300 micron thick region. The crud is also mapped into each DeCART axial mesh (plane) from the MAMBA axial mesh.

.

Table 2 - Boron letdown curve

Day	Boron (ppm)
0	1200.0
25	1165.7
50	1159.5
75	1118.5
100	1058.2
125	991.20
150	916.60
175	836.60
200	751.40
225	660.50
250	565.60
275	466.50
300	365.30
325	259.80
350	152.20
375	43.500
400	0.0000

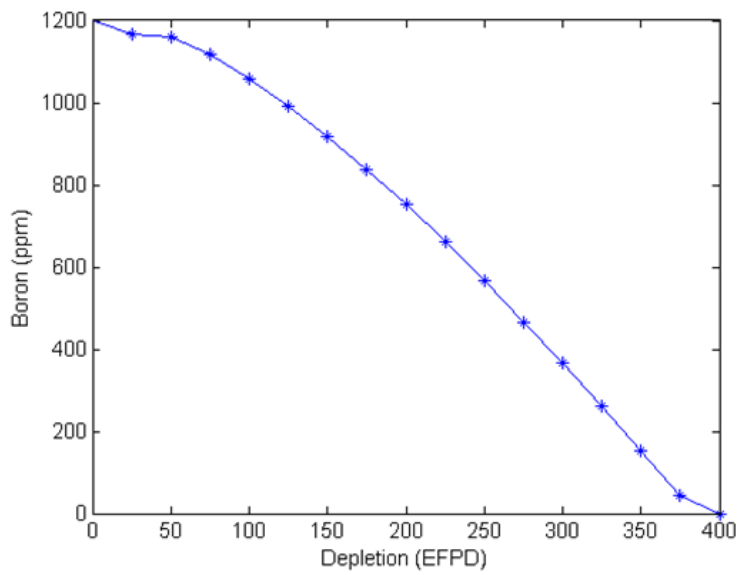

Figure 10 Boron letdown curve

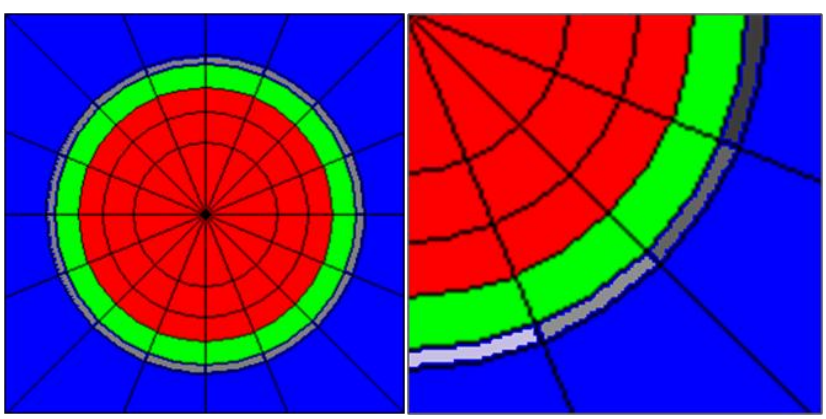

Figure 11 DeCART pin cell model with crud in outermost radial division (left), and azimuthally dependent crud concentration with homogenized crud region thickness constant (right).

The current DeCART model does not include a neutronics model of the grid spacers since some minor modifications to the DeCART mapping scheme is required to accommodate both a crud region and a grid spacer region. These modifications were not tested in time for the current project; therefore the increase in neutron absorption in the vicinity of the grid spacer materials is

not represented in the results shown here. However, all aspects of the grid spacers are represented in the STAR-CCM+ model and therefore the most important physics of grid spacers for crud deposition modeling are present which include crud removal due to increased fluid turbulence. As noted previously, in this preliminary implementation data is not transferred from DeCART to MAMBA and therefore the effect of boron depletion within the crud is also not modeled. Both the effects of grid spacer on the neutronics and the boron depletion will be included in the next phase of the project.

MAMBA Model Description

Background

MAMBA (MPO Advanced Model for Boron Analysis) v2.0 is a Fortran based computer code which simulates three-dimensional crud growth along the surface of a single fuel rod. The primary coupled physics and chemistry associated with crud formation that are currently treated in MAMBA include: (1) solving a general non-linear 3D heat transport equation for the crud layer including localized heat sinks due to the internal boiling within the crud layer, (2) an adaptive grid which grows radially in time as mass deposits on the surface of the crud, (3) time evolving microstructure (porosity) of the crud layer due to localized deposition and precipitation of nickel ferrite ($NiFe_2O_4$) and lithium tetraborate ($Li_2B_4O_7$) within the pores of the crud, (4) time evolving lithium and boric acid coolant chemistry both at the crud surface and inside the pores of the crud, (5) mass transport of various soluble coolant species into the interior of the crud due to boiling induced Darcy flow, (6) diffusion of various soluble species inside the crud due to the flow induced concentration gradients within the crud layer, and (7) mass evaporation in the form of steam vapor due to the localized boiling inside the crud layer. MAMBA utilizes a cylindrical coordinate system (r, θ, z) and is capable of simulating crud deposition along the entire surface of a 400cm long fuel rod. It can also "zoom in" and treat selected regions of the fuel rod in high resolution.

The crud surface deposition rate is governed by two rate parameters, one for boiling regions which is multiplied by the local mass evaporation rate (i.e., the steaming flux leaving the boiling chimneys), and one for non-boiling regions. In boiling regions, the crud growth rate is enhanced due to the boiling induced flow of coolant into the crud's surface which increases the flux of particulates onto the crud's surface. The crud surface deposition rate also includes a user selectable option for including an erosion (loss) term. The functional form for the erosion rate can be supplied by the user or chosen to be proportional to the STAR-CCM+ computed turbulent kinetic energy. The coolant chemistry is supplied by the user or an ex-core model (i.e., BOA) and consists of the standard inputs: (1) boron concentration (ppm), (2) lithium concentration (ppm), (3) H_2 concentration (cc/Kg), (4) soluble Ni (ppb), (5) soluble Fe (ppb), and (6) particulate $NiFe_2O_4$ concentration (ppb). The external boundary conditions which are needed by the 3D heat transport solver include: (1) the heat flux at the cladding surface, and (2) the temperature or heat transfer coefficient at the crud/coolant interface. The various crud properties used by MAMBA are based on the Westinghouse WALT loop studies (EPRI, 2011). These include porosity ($\varepsilon = 0.6$), crud density ("solid skeleton" 5.33 g/cm^3), crud thermal conductivity ("solid skeleton" 0.011 W/cm-K), average chimney radius (4 microns), and average chimney density (1.6 x 10^5 per cm^2). The bulk properties of the crud such as its thermal conductivity are

computed using a standard "mixing fraction": $k = (1 - \varepsilon)\, k_s + \varepsilon\, k_w$ where k_s is the thermal conductivity of the solid crud ($NiFe_2O_4$) and k_w is the temperature dependent thermal conductivity of the water filling the pores of the crud and ε is the time-dependent local porosity.

Coupling strategy

As mentioned above, MAMBA requires external boundary conditions consisting of the heat flux at the cladding surface and the temperature (or heat transfer coefficient) at the crud/coolant interface. These external boundary conditions represent the interface between MAMBA and a thermal hydraulics code such as STAR-CCM+ (see Figure 3). In order to account for the temperature drop across the crud layer within STAR-CCM+, MAMBA computes an effective thermal resistance and the crud thickness at each surface grid point and passes this information to STAR-CCM+. The effective thermal resistance includes the heat flux due to local boiling within the crud layer. In this way, two-phase boiling phenomena can be accounted for within a single-phase fluid code. For example, localized boiling in the crud layer will reduce the effective thermal resistance in that region which in-turn increases the heat flux from the cladding surface into the fluid. This additional heat flux increases the fluid temperature mimicking the effects of the heat flux (steam vapor) escaping from the boiling chimneys. In the present work, the coupling or data exchange between MAMBA and STAR-CCM+ was performed at 50 day intervals via file transfer over email. The mapping of the STAR-CCM+ grid onto the MAMBA grid was performed by MAMBA.

The coupling between MAMBA and a neutronics code such as DeCART revolves around the 3D boron distribution within the crud layer. The present interface between MAMBA and DeCART is implemented via a file transfer of the MAMBA computed 3D boron distribution. The mapping of the MAMBA grid onto the DeCART grid is performed by DeCART. The file exchange between MAMBA and DeCART was performed at the same time as the STAR-CCM+ file exchange via email. The MAMBA computed 3D boron distribution was supplied to DeCART at 25 day intervals.

In summary, the MAMBA calculations were run for 50 day intervals for the fixed boundary conditions computed by STAR-CCM+ based on the MAMBA data from the previous 50 day interval. The boron distribution was supplied to DeCART at 25 day intervals. The coolant conditions including soluble and particulate concentrations were held fixed over the 400 day simulation but in general these will be time varying and supplied by the "ex-core" reactor model (such as BOA), which includes the "sources" of nickel and iron in the coolant due to corrosive release from the various reactor surfaces in contact with the coolant (such as the steam generator tubes). Once all of these codes and interfaces are integrated within VERA, a much tighter and efficient coupled calculation can be pursued (see previous chapter on "Coupled Code Iteration Scheme" for more details).

The crud surface deposition rates in MAMBA were chosen to produce a thick crud layer (~190 microns) by the end of the 400 day simulation. The boron concentration in the coolant was also held fixed at 1600ppm. The aggressive combination of a thick crud layer and high boron concentration was chosen for this initial demonstration simulation in order to ensure significant boron deposition within the crud and increase the chances for a detectable power shift in the

single rod neutronics calculation. More realistic scenarios based on plant data will be pursued in future work.

Results of Crud Deposition Simulation

This section will provide results for the simulation of a burnup cycle using the coupled MAMBA/DeCART/STAR-CCM+ codes described in the previous section. The first subsection will summarize the initial conditions for the simulation calculated with the DeCART/STAR-CCM+. The subsequent sections will present results for 100 day steps of the burnup cycle obtained from each of the three codes, STAR-CCM+, MAMBA, and DeCART. In the sections were STAR-CCM+ and MAMBA results are presented, only the simulations for the boron case corresponding to a constant coolant boron concentration of 1600 ppm over the cycle are presented.

Initial (t=0) Solution

A coupled DeCART/STAR-CCM+ simulation was performed on the pin cell model shown in the previous sections in order to compute the initial steady-state solution for the distributions of power, fuel and cladding temperatures, and coolant fluid-dynamic conditions. The standard tolerances were imposed on the STAR-CCM+ enthalpy residual and the DeCART power density.

The resulting axial power profile is reported in Figure 12, while the corresponding cladding temperature distribution is shown in Figure 13 (with the coolant flowing from left to right). The effect of the mixing vanes on the heat transfer between fuel pin and coolant is clearly visible, with the cladding temperature dropping after each grid spacer. It should be noted that the power is slightly bottom peaked at the beginning of cycle because of the slightly higher moderator density at the inlet of the channel and the bottom of the pin.

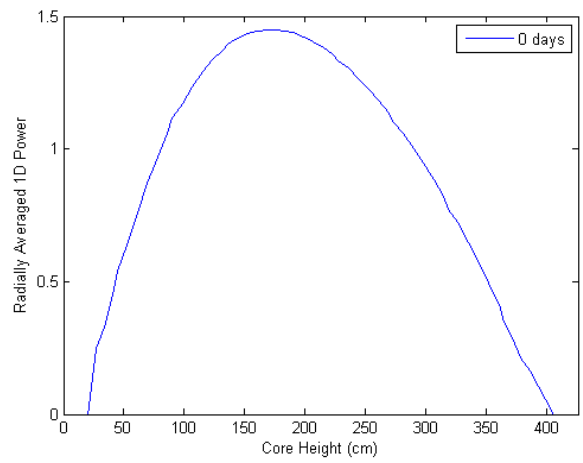

Figure 12 Axial power profile at time t = 0

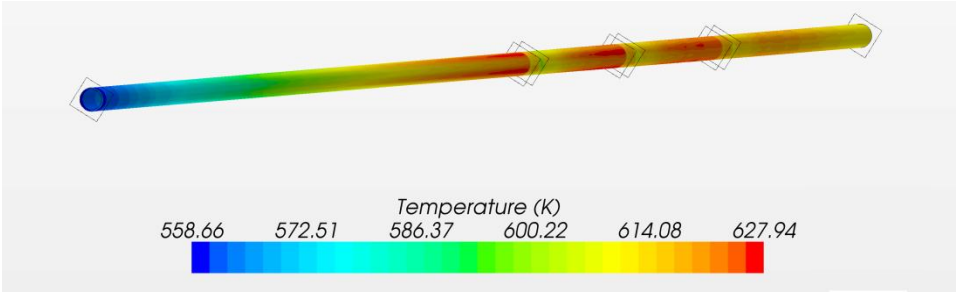

Figure 13 Cladding temperature distribution at time t = 0

Figure 14 shows the azimuthally dependent power density profile of the converged DeCART/STAR-CCM+ solution at 0 days. The power is averaged over the individual flat source regions within DeCART. Figure 15 shows the azimuthally dependent temperature profile for the converged solution as well.

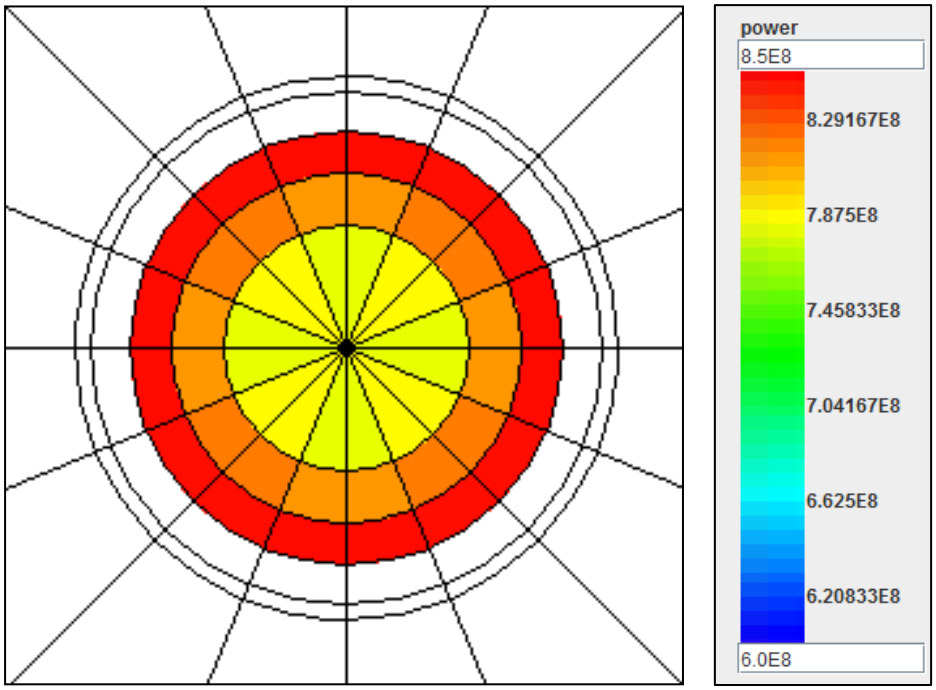

Figure 14: Azimuthally dependent power density profile at the fuel rod mid plane.

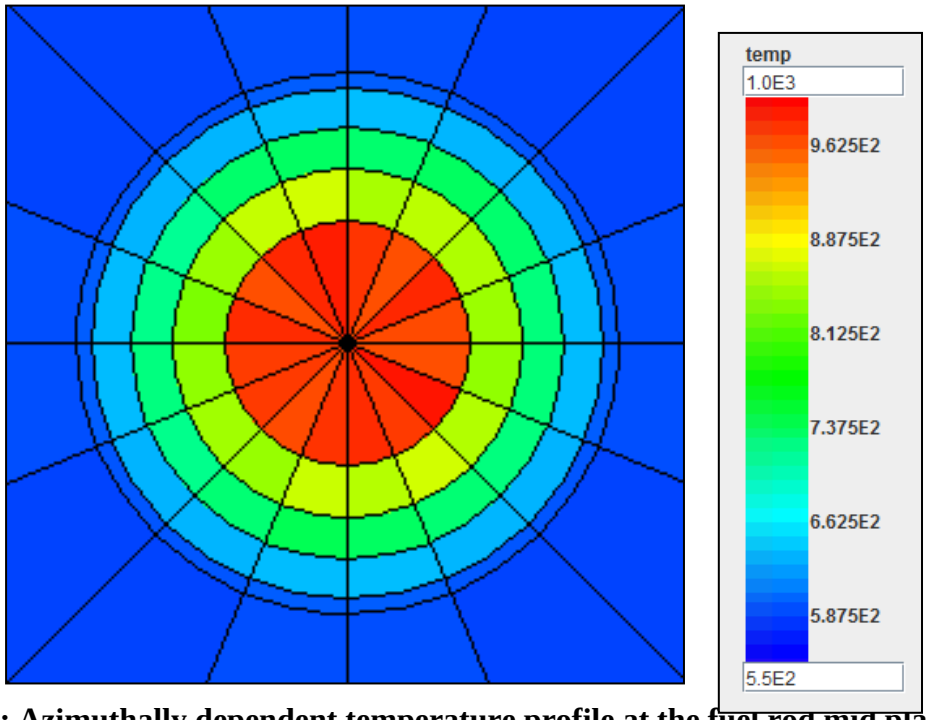

Figure 15: Azimuthally dependent temperature profile at the fuel rod mid plane.

MAMBA/DeCART/STARCCM+ Coupled Simulation Results

Results are presented in this section for coupled MAMBA/DeCART/STAR-CCM+ simulations. The results presented here correspond to the crud deposition predicted by MAMBA in which the boron in the coolant was maintained at 1600 ppm throughout the cycle. The DeCART depletion was performed with a typical PWR boron letdown curve shown in Figure 10.

STAR-CCM+ results

Detailed STAR-CCM+ results are reported in Appendix I from time t = 0 days to time = 400 days. 3D illustrations are shown of crud layer temperature distribution and turbulent kinetic energy in the boundary layer around the fuel pin at the location of each of the three spacers respectively, as well as the azimuthal variation of cladding surface and crud layer surface temperature profiles before, after and in the middle section of each of the three spacers respectively. In this section, only major results will be discussed.

In Figure 16 the temperature distribution on the crud layer surface and the turbulent kinetic energy in the boundary layer are presented at time t = 100 days for pin regions around the grid spacers 1 and 3 respectively. As expected, higher temperatures are observed in regions corresponding to lower turbulent kinetic energy. This is because the lowest heat transfer coefficients occur in the regions of lowest turbulent kinetic energy. At the same time the lowest crud erosion rates occur at these locations, which means thicker crud deposits and therefore higher thermal resistances, which in turn will result in higher cladding temperature. This effect is important, because higher cladding temperatures will yield an even higher crud deposition which will provide a positive feedback between crud deposition and cladding temperature. This will lead to a continuous growth of the crud layer and to the characteristic "striping" of crud deposits observed in practice (see Figure 1).

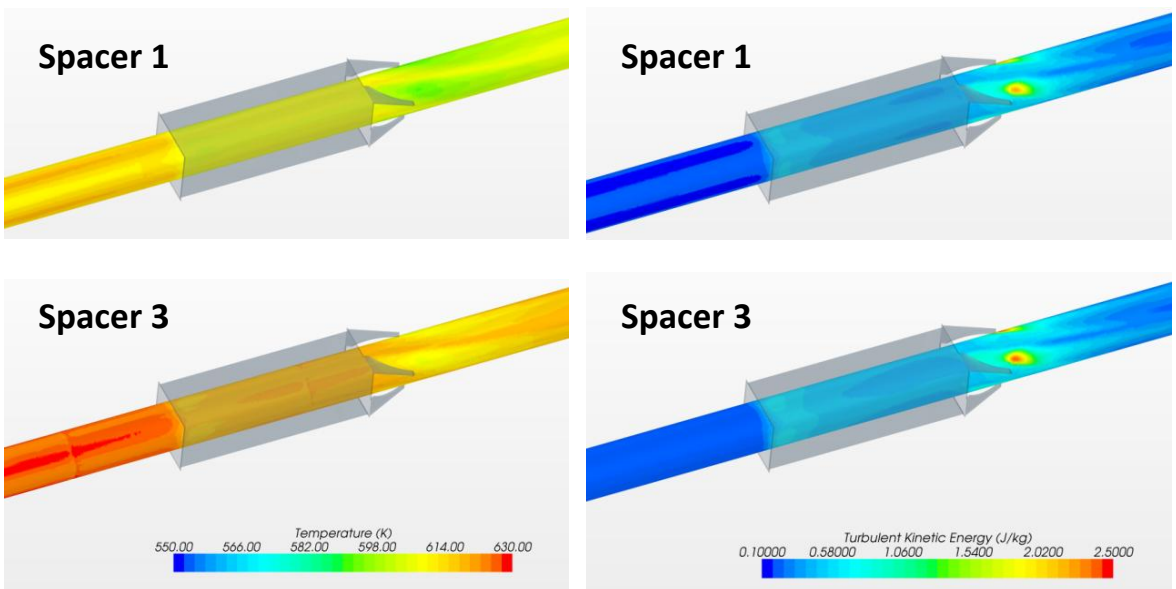

Figure 16 Crud temperature distribution (left) and turbulent kinetic energy (right) for grid spacer 1 and 3 respectively - t = 100 days.

The axial variation of turbulent kinetic energy is shown in Figure 17. Turbulence is generated at the inlet of the grid spacers (low spikes in Figure 17) and by the mixing vanes (high spikes in Figure 17) and decays exponentially with increasing distance from the vanes. Therefore, higher erosion rates and thus lower crud deposit thicknesses are expected soon after the mixing vanes. Similarly lower erosion rates and thus higher crud deposit thicknesses are expected before the grid spacers, where the turbulent kinetic energy is the lowest. This is confirmed by the crud deposit predicted by MAMBA, which are presented in the next chapter.

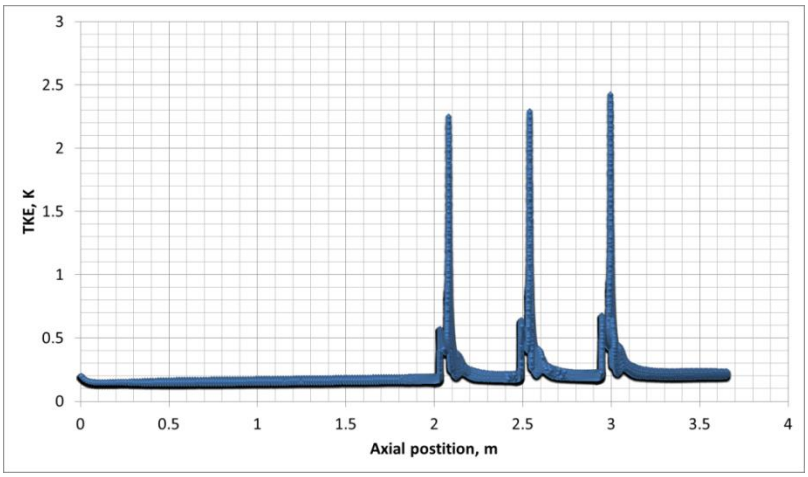

Figure 17 Axial variation of turbulent kinetic energy - t = 100 days.

Detailed azimuthal profiles of relevant parameters are extracted at three axial locations in the proximity of the spacer grids, namely in the middle plane and 40 mm downstream and upstream of each spacer respectively (see Figure 18). In Appendix I the detailed results obtained in the proximity of each spacer are shown. For the sake of simplicity only the results obtained in the proximity of spacer 1 are presented here (see Figure 19).

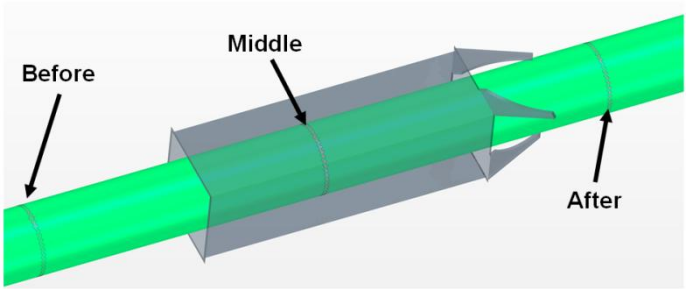

Figure 18 Positions for azimuthal temperature variation

In Figure 19 the azimuthal temperature profiles on the cladding surface (i.e. below the crud layer) and of the crud layer surface in contact with the coolant obtained in proximity of spacer 1 at time t = 100 days are presented at the three axial locations illustrated in Figure 18 (see Figure 19 a-c respectively). The turbulent kinetic energy downstream of spacer 1 is shown in Figure 19 (d).

(a)

(b)

(c)

(d)

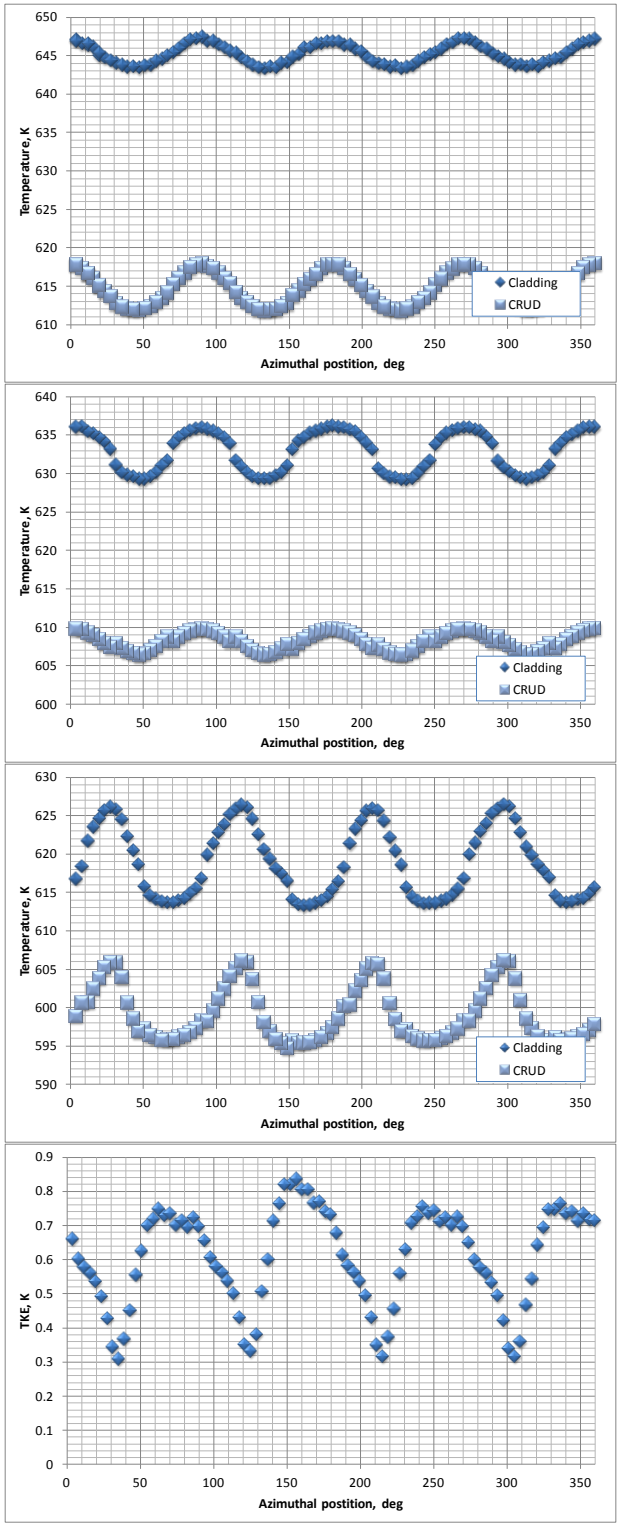

Figure 19 Azimuthal cladding and crud surface temperatures (a) before spacer (b) at the spacer (c) after spacer, and (d) turbulent kinetic energy in the boundary layer after grid spacer – spacer 1. Results at t = 100 days.

It can be observed that after 100 days a temperature difference of more than 20 K is predicted across the crud layer. At this time, MAMBA predicts a maximum crud thickness of 50 μm (see next chapter). It is observed that even these small crud thicknesses can give rise to large temperature increases of the cladding temperature, therefore significantly contributing to the formation of hot spots on the cladding surface. Comparing Figure 19 (a) to (c), it also possible to observe an azimuthal shift in maximum cladding/crud temperatures. This is due to the flow swirl induced by the mixing vanes of the spacer grid. The effects of the flow swirl are clearly observed in Figure 16 as well.

Comparing Figure 19 (c) and (d), it can be seen that turbulent kinetic energy (TKE) and cladding/crud surface temperatures are out-of-phase, i.e. a maximum of TKE corresponds to a minimum in the cladding/crud surface temperatures. This is because of the enhancement of heat transfer within the coolant.

It should be noted that, in order to reduce the CPU requirements, the coupled MAMBA/STAR-CCM+/DeCART simulations were carried out with a relatively coarse axial mesh in MAMBA. This generates some discontinuities in the thermal fluid-dynamic parameters computed by STAR-CCM+, especially when the crud thicknesses become large. This can be clearly observed in Figure 20, where the crud temperature distribution is reported in the proximity of the grid spacer 3 at a time t = 400 days (the axial mesh adopted in MAMBA extends above the axial dimension of a single grid spacer).

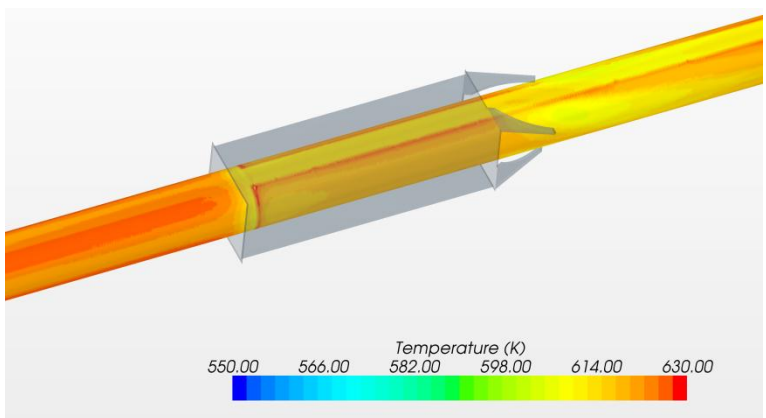

Figure 20 Crud temperature distribution for grid spacer 3 - t = 400 days

A substantial reduction in discontinuities is achieved by refining the MAMBA mesh close to the grid spacers. This can be observed in Figure 21 where the results obtained with a MAMBA/STAR-CCM+ coupled simulation for a limited axial domain of the entire pin are shown, where a finer MAMBA axial mesh has been used (the cladding temperature Figure 21 is lower than the one presented in Figure 16 because the power distribution imposed as boundary conditions for the finer-mesh MAMBA/STAR-CCM+ simulation was slightly lower than the power distribution obtained with the coupled MAMBA/STAR-CCM+/DeCART coupled code).
Analyzing Figure 21 it is possible to observe that the highest crud erosion (and thus the lowest thermal resistance) occurs in regions corresponding to the maximum turbulent kinetic energy. In future work, consistent resolutions of the CFD and MAMBA mesh will be performed, with particular attention to the axial nodalization in the proximity of grid spacers.

(a)

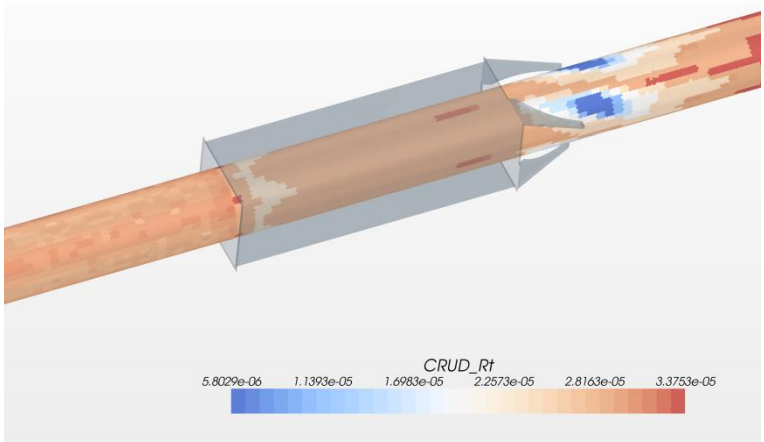

(b)

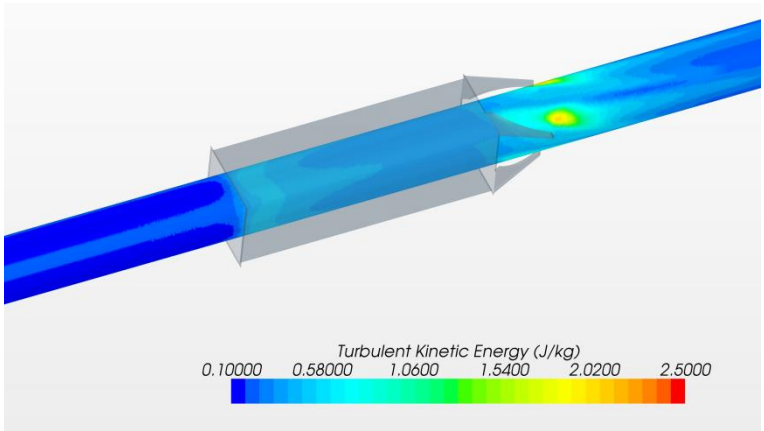

(c)

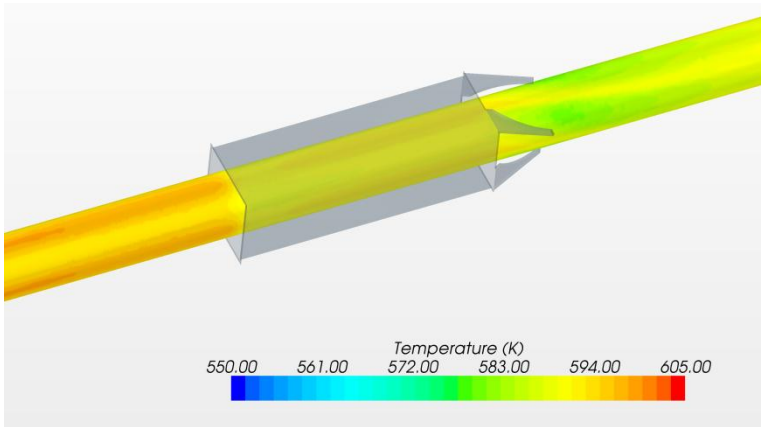

Figure 21 (a) Crud thermal resistance [m^2K/W], (b) Turbulent kinetic energy, (c) Cladding temperature - simulation with MAMBA refined mesh at time t = 80 days.

MAMBA results

As noted previously, the results presented in this section correspond to the crud deposition predicted by MAMBA in which the boron in the coolant was maintained at 1600 ppm throughout the cycle. This high boron concentration, together with a high crud surface deposition rate, was

chosen for this initial demonstration in order to ensure significant boron deposition within the crud and to increase the likelihood or a detectable power shift in the single rod neutronics calculation. More realistic PWR scenarios will be pursued in future work.

A 3D perspective plot of the crud thickness along the surface of the fuel rod is shown in Figure 22. The coolant flow is from left to right and the effects of the three spacers are clearly visible in the three blue "rings" towards the upper right section of the rod. The blue rings represent regions of thin crud (< 5 microns). These regions of thinner crud are due to both surface erosion and a lower surface temperature originating from the turbulent flow through the four mixing vanes attached to each spacer. The surface erosion rate in MAMBA is taken to be proportional to the STAR-CCM+ computed turbulent kinetic energy (TKE). The TKE is largest immediately behind the mixing vanes which results in both a higher erosion rate and a cooler surface temperature. In contrast, the crud layer is thickest (red) in the flow "stagnation" regions just below the three spacers. The bottom panel of Figure 22 shows a magnified region around the first spacer. A very high resolution MAMBA simulation was performed for this region. Interesting crud formation patterns ("swirling" and "streaking") are clearly visible which directly correlate with the temperature and TKE surface distributions computed by STAR-CCM+.

Figure 23 plots the effective thermal resistance and crud temperature (10 microns above the cladding surface) for the region around the first spacer. The effective thermal resistance is used by STAR-CCM+ in its conjugate heat transfer calculation in order to account for the temperature drop across the crud layer. As expected, the crud temperature near the cladding surface is hottest in regions of thicker crud which results in even faster crud deposition (i.e., "positive feedback"). The hotter (red) region below the spacer is approaching the saturation temperature (~ 346°C) which indicates that boiling within the crud layer in that region is imminent (boiling is already occurring in that region at the cladding/crud interface). The thicker and hotter crud regions can lead to enhanced boron deposition and cladding surface corrosion increasing the risk for CIPS and CILC, respectively.

Figure 24 plots the crud thickness at 100 day intervals for the 400 day coupled simulation. As expected, the crud is thickest in the hotter portions of the rod especially in the regions just below each spacer. The thinner regions of crud associated with the mixing vanes (blue rings) remain visible. However, the region behind the first mixing vane begins to "fill-in" somewhat by 300 days and the regions behind the first and second mixing vanes have filled in by 400 days although part of the "filling in" for the 400 day results is due to the lower axial resolution (dz=10cm instead of 5cm) used for the 300-400 day time period. Figure 25 plots the boron surface density at 100 day intervals for the 400 day coupled simulation. The boron surface density is computed by integrating the three-dimensional boron density in the radial direction through the crud layer at each axial and azimuthal grid point. The boron density is largest in the regions of thicker crud (as expected) and clearly exhibits an axial asymmetry. The axial asymmetry in boron uptake along the rod is the root cause of the CIPS (see Figure 34).

Figure 26 plots the mass evaporation rate along the surface of the rod due to boiling within the crud layer. The mass evaporation rate is important since it determines the velocity of coolant being drawn into the surface of the crud due to the boiling occurring inside the crud. The coolant flow into the crud enhances the deposition of particulates onto the crud's surface further

accelerating its growth (more positive feedback). As expected, the boiling rate is largest for the thicker and hotter crud regions.

Figure 27 plots the MAMBA computed crud temperature at 100 day intervals for the 400 day coupled simulation for a two-dimensional slice through the 3D crud layer in the axial direction. The azimuthal angle is fixed at zero degrees which corresponds to x=0.476 cm and y=0.0 cm in STAR-CCM+ coordinates. The coolant flow is from bottom (z=0) to top (z=370cm) and the cladding surface is along the left edge (y-axis) of the plots. The erosion effects due to the localized increase in the turbulent kinetic energy associated with the mixing vanes on each of the three spacers are clearly evident by the three "valleys" which occur at approximately z = 210, 255, and 300 cm. The temperature distribution within the crud is computed by MAMBA once the boundary conditions at the cladding surface and crud/coolant interface are specified. In the coupled simulation, these boundary conditions (the heat flux at the cladding surface and the temperature at the crud/coolant interface) are provided by STAR-CCM+. The MAMBA heat transfer calculation also includes local heat sinks due to boiling within the crud layer. As time evolves, the crud layer thickens due primarily to the surface deposition of particulate nickel ferrite ($NiFe_2O_4$). The surface deposition rate is enhanced above boiling regions of the crud due to the boiling induced flow of coolant into the crud's surface. As the crud layer thickens and the boiling rate increases, the concentration of boric acid near the cladding surface increases. Once the concentration exceeds the precipitation threshold, lithium tetraborate ($Li_2B_4O_7$) rapidly precipitates out of the solution and deposits within the available volume in the pores of the crud. This reduces the porosity of the crud and increases its local thermal conductivity. The "hot fingers" protruding upwards from the cladding surface starting at 300 days and very evident at 400 days are the result of lithium tetraborate precipitation within the crud. At 400 days, the cladding surface temperature has become quite hot and exceeds 460°C in the region between z=275 and 315 cm. Localized hot spots such as these can lead to accelerated corrosion of the cladding surface and an increased risk for CILC.

The porosity of the crud layer is plotted in Figure 28 at 100 day intervals. The porosity slowly changes in time due to the continual precipitation and deposition of soluble nickel ferrite ($NiFe_2O_4$) within the pores of the crud. The rate of nickel-ferrite deposition within the crud is enhanced by localized increases in temperature and boiling. The local porosity can also quickly change due to the rapid precipitation of lithium tetraborate (once the appropriate conditions for precipitation are reached). Figure 28 shows a decrease in porosity near the cladding surface for the 100 and 200 day time slices due primarily to Nickel-Iron oxide deposition (yellow-green regions). By 300 and 400 days, the precipitation of lithium tetraborate has occurred near the cladding surface and filled a significant volume of the crud reducing its porosity to nearly zero (blue regions). Figure 29 plots the boron concentration at 100 day intervals. The lower boron concentrations (blue regions) for the 100 and 200 day time slices correspond to boron in the form of soluble boric acid (BO_3H_3). As the crud layer thickens, the temperature near the cladding surface increases leading to boiling within the crud layer. This internal boiling induces significant flow of coolant into the crud's surface which ultimately circulates back out of the crud layer in the form of steam vapor exiting via the chimneys. The flow of coolant increases the concentration of boric acid near the cladding surface which eventually leads to the precipitation of lithium tetraborate. The large boron concentration (green-yellow-red) seen in the 300 and 400 day time slices corresponds to boron in the form of solid lithium tetraborate ($Li_2B_4O_7$.). The

soluble boric acid layer (blue region) has move further away from the cladding surface. The two notable "fingers" of lithium tetraborate extending outwards from the cladding surface near z=285 and 310 cm are due to the enhanced internal boiling occurring in those two regions due to thicker crud.

Figure 30 plots the local boiling heat power density due to internal boiling within the crud layer. This boiling heat power density represents the local heat flux leaving a given volume element due to steam vapor exiting via the chimneys in that region. Thus, this heat flux corresponds to the "heat sinks" mentioned in the above discussion on MAMBA's internal heat transport calculation (see above discussion of Figure 27). The boiling regions typically occur within the crud layer near the cladding surface. The crud surface itself is mostly sub-cooled. However, some superheating at the crud's surface is observed in a couple of regions near z=290 and 330-360 cm (see the small "islands" of boiling flux near the crud's surface in these regions). This surface superheating also increases the surface deposition rate of the crud in those regions. As the porosity of the crud decreases near the cladding surface over time, the boiling region moves away from the surface into the more porous crud layer. The regions with largest boiling flux (yellow-red) correlate with the regions of highest boric acid concentration (the blue regions in Figure 29). The boiling within the crud layer induces substantial coolant flow into the surface of the crud.

Figure 31 plots the velocity of the fluid flow inside the crud layer due to internal boiling. This "boiling velocity" provides an important mechanism for mass transport of the various soluble species deep into the hotter regions of the crud layer where the various chemical reactions leading to precipitation and deposition can occur. Important soluble species transported from the coolant into the crud include: boric acid, lithium, nickel and iron. As expected, the boiling velocity is largest over regions with substantial boiling heat power density (see Figure 30).

Figure 32 plots the integrated boron mass over the entire volume of the crud layer on the fuel rod for the 200 - 300 day period. The total boron mass is computed as a function of time for three different grid resolutions. The green curve corresponds to the highest resolution grid: dr= 5 microns, $d\theta=20°$, and dZ=5 cm. The red curve corresponds to dZ=10cm (with dr and $d\theta$ unchanged) and the blue curve corresponds to $d\theta=40°$ (with dr and dZ unchanged). A Mamba-DeCart-StarCCM+ data exchange occurs at 250 days. The computed boron concentration increases relatively smoothly with time. A small "bump" is barely visible in the full resolution (green) curve at 250 days due to the data exchange and Mamba restart which occurred there. The three results are in good overall agreement. The largest differences occur at 300 days for which the red and blue curves differ from the full resolution (green) curve by 17% and 9%, respectively.

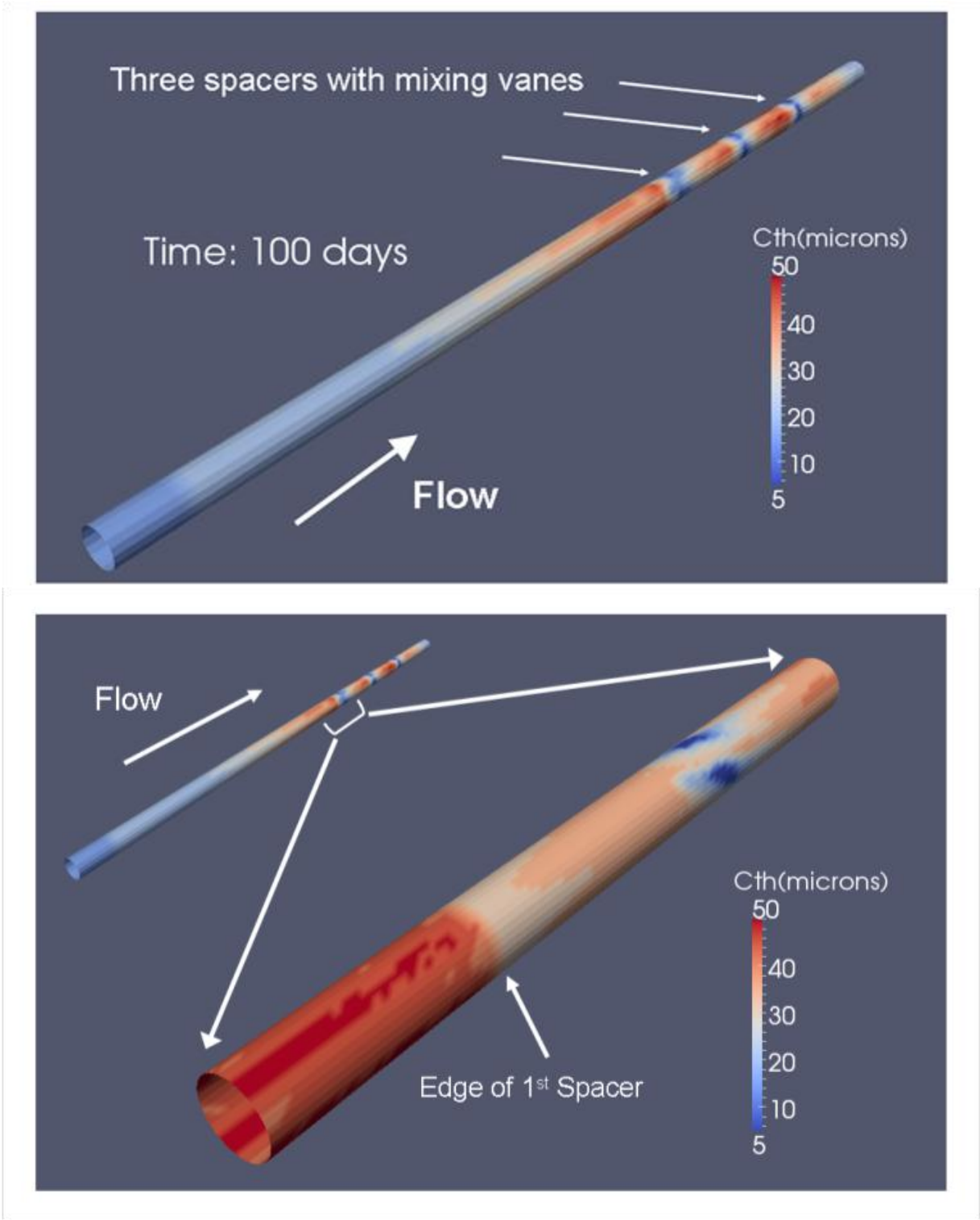

Figure 22 Coupled Mamba/DeCart/StarCCM+ simulation of crud formation on a single fuel rod with three spacers and four mixing vanes on each spacer. The effects of the three spacers are clearly visible by the three blue "rings" in the upper/right portion of the rod (top panel). A magnified view of the region around the first spacer grid is show in the bottom panel. The crud thickness correlates with the fluid flow patterns.

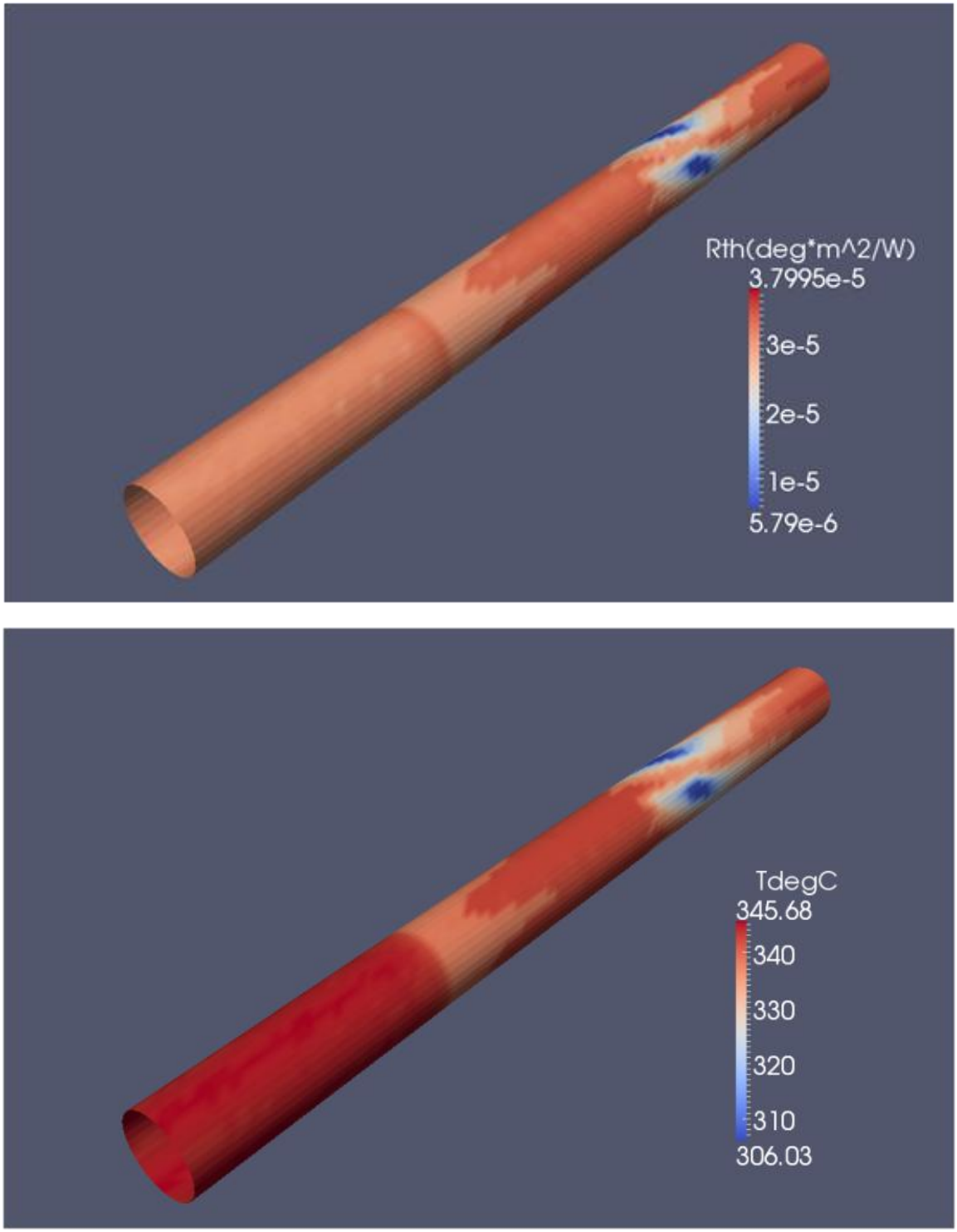

Figure 23 The effective crud thermal resistance (top panel) and the crud temperature 10 microns above the cladding surface (bottom panel) are plotted in the region around the first spacer grid. As expected, the temperature is highest in the regions of thicker crud. Significant azimuthal and axial variations in crud deposition behavior are clearly visible due to the complex flow patterns.

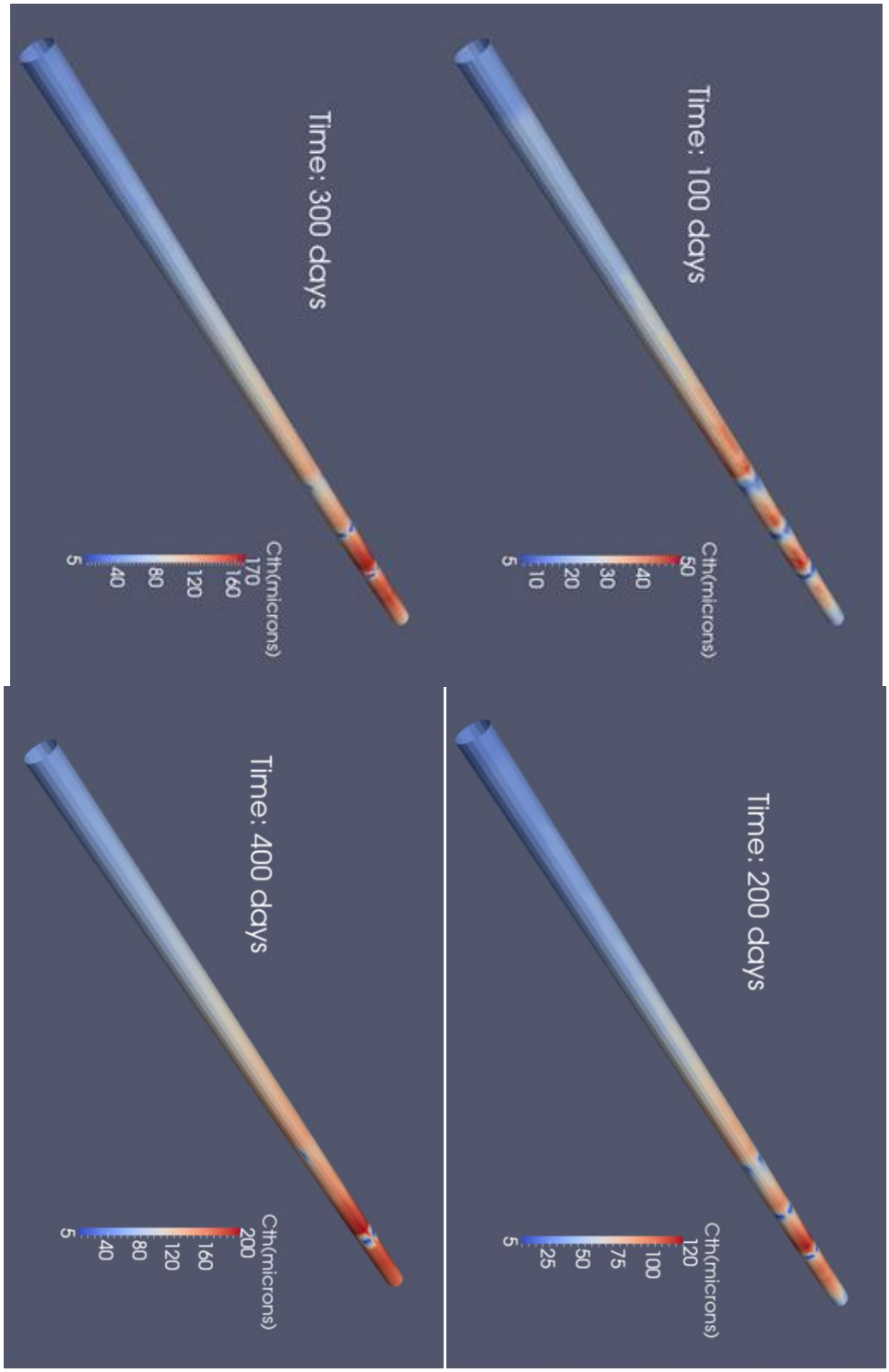

Figure 24 The crud thickness is plotted at 100 day intervals for the coupled Mamba/DeCart/StarCCM+ simulation. The crud is thickest in the hotter portions of the rod especially in the regions just below the spacers. The turbulent mixing due to the mixing vanes on each spacer retards the crud formation in the regions near the mixing vanes (blue rings).

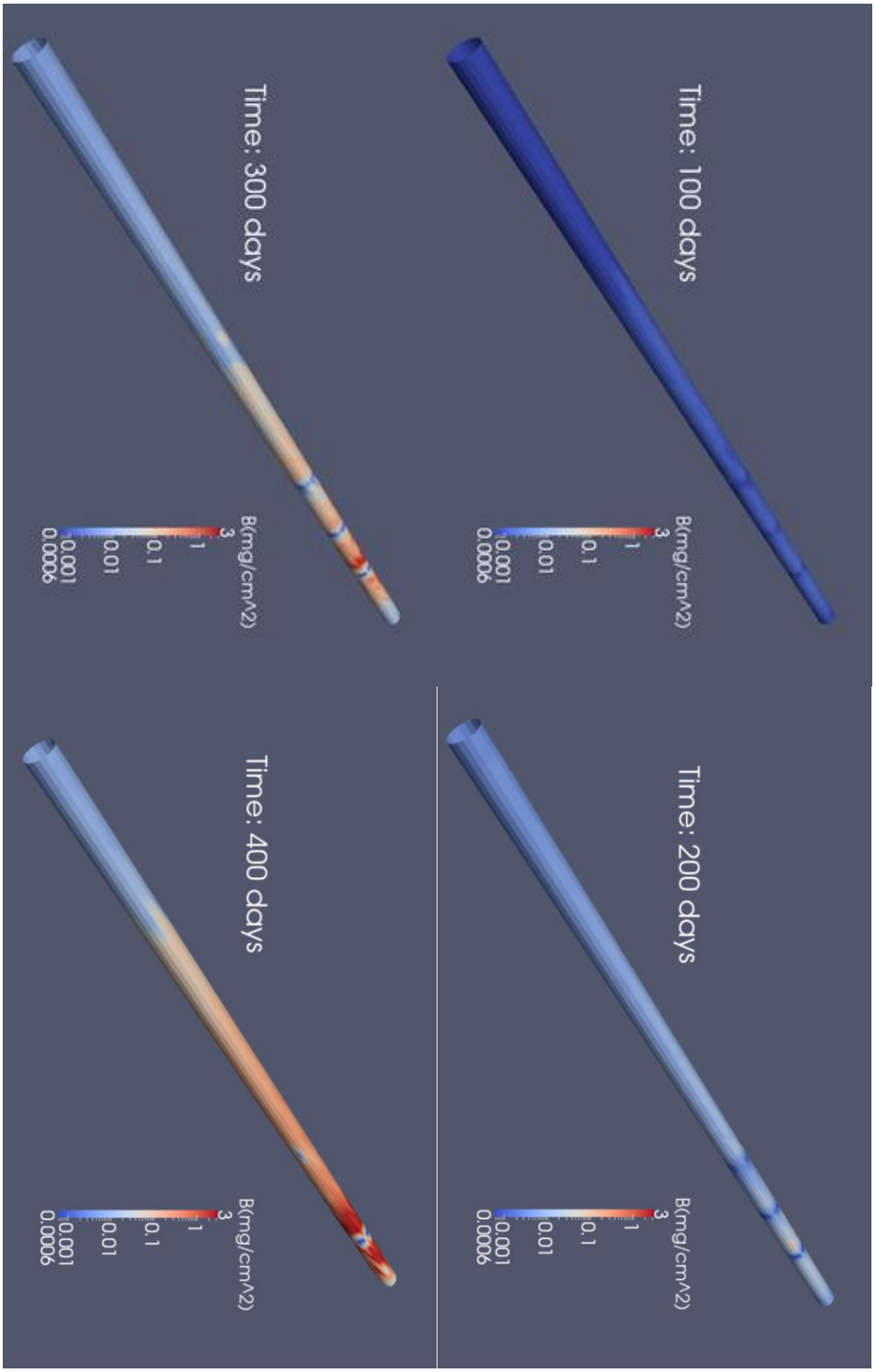

Figure 25 The boron surface density is plotted at 100 day intervals for the coupled Mamba-DeCart-StarCCM+ simulation. The boron density is largest for the thicker crud regions and its axial distribution is clearly asymmetric.

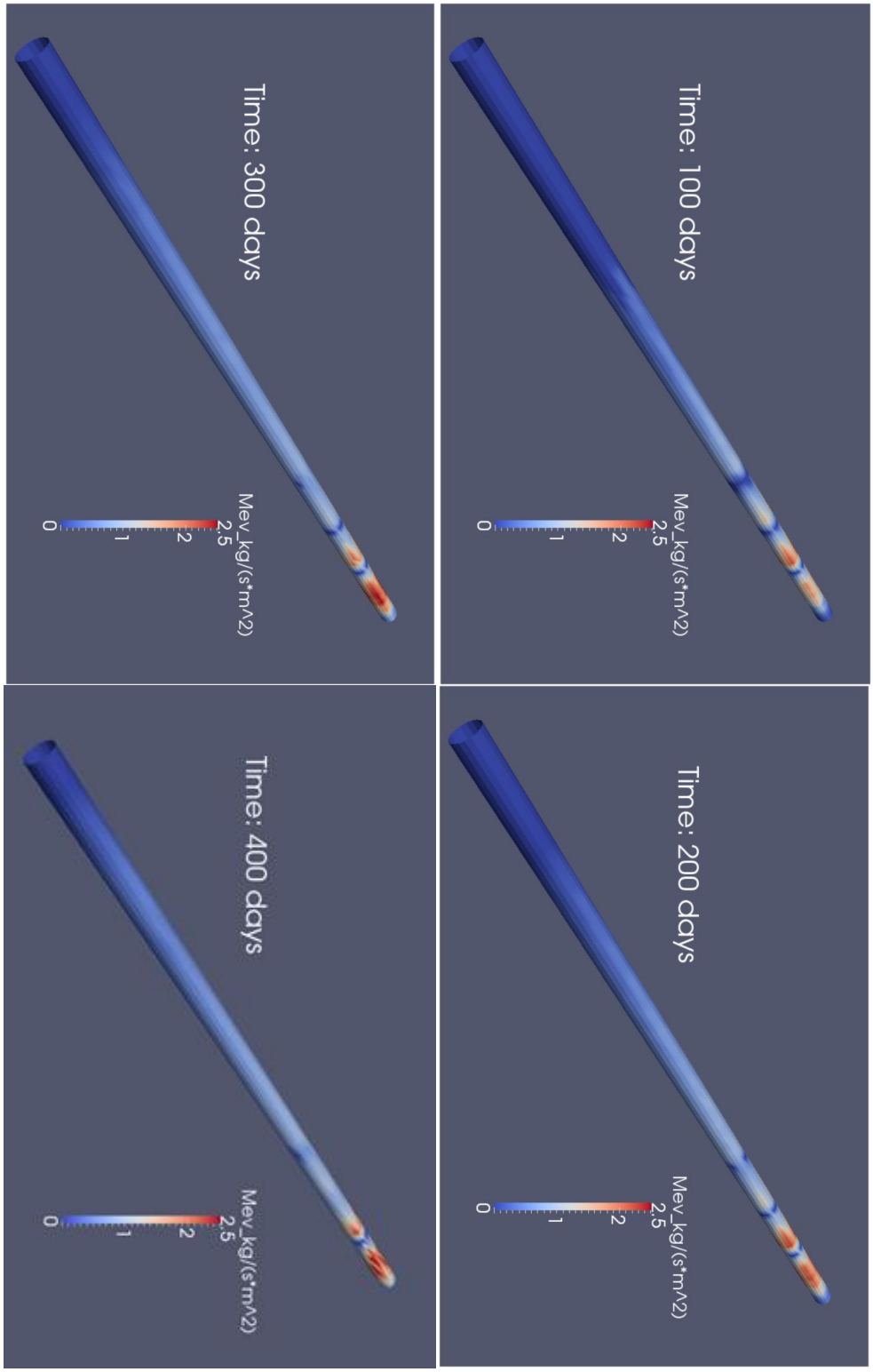

Figure 26 The mass evaporation rate is plotted at 100 day intervals for the coupled Mamba-DeCart-StarCCM+ simulation. The mass evaporation rate is largest for the thicker crud regions and it indicates the amount of boiling occurring within the crud layer.

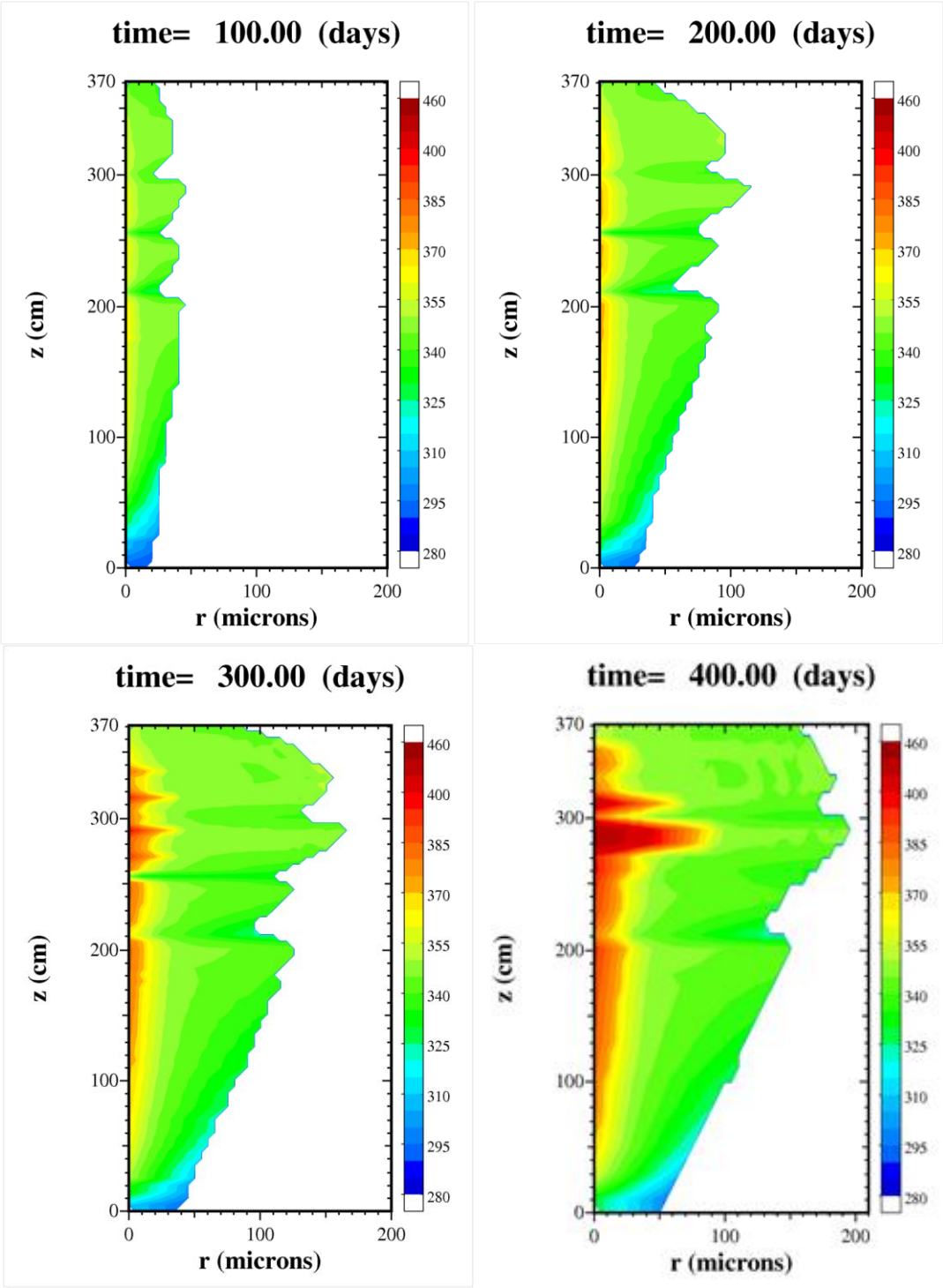

Figure 27 The temperature (in ^{o}C) distribution across the crud layer is plotted for a two-dimensional slice along the axial direction (azimuthal angle fixed at 0°) at 100 day intervals for the coupled Mamba/DeCart/StarCCM+ simulation. As the crud layer thickens and the porosity of the crud decreases, "hot spots" form at the cladding surface. Note: the cladding surface is along the left edge of the plot and the axial resolution for the 400 day plot is lower (10cm versus 5cm in the other plots). The coolant flow is from bottom z=0 to top z=370 cm.

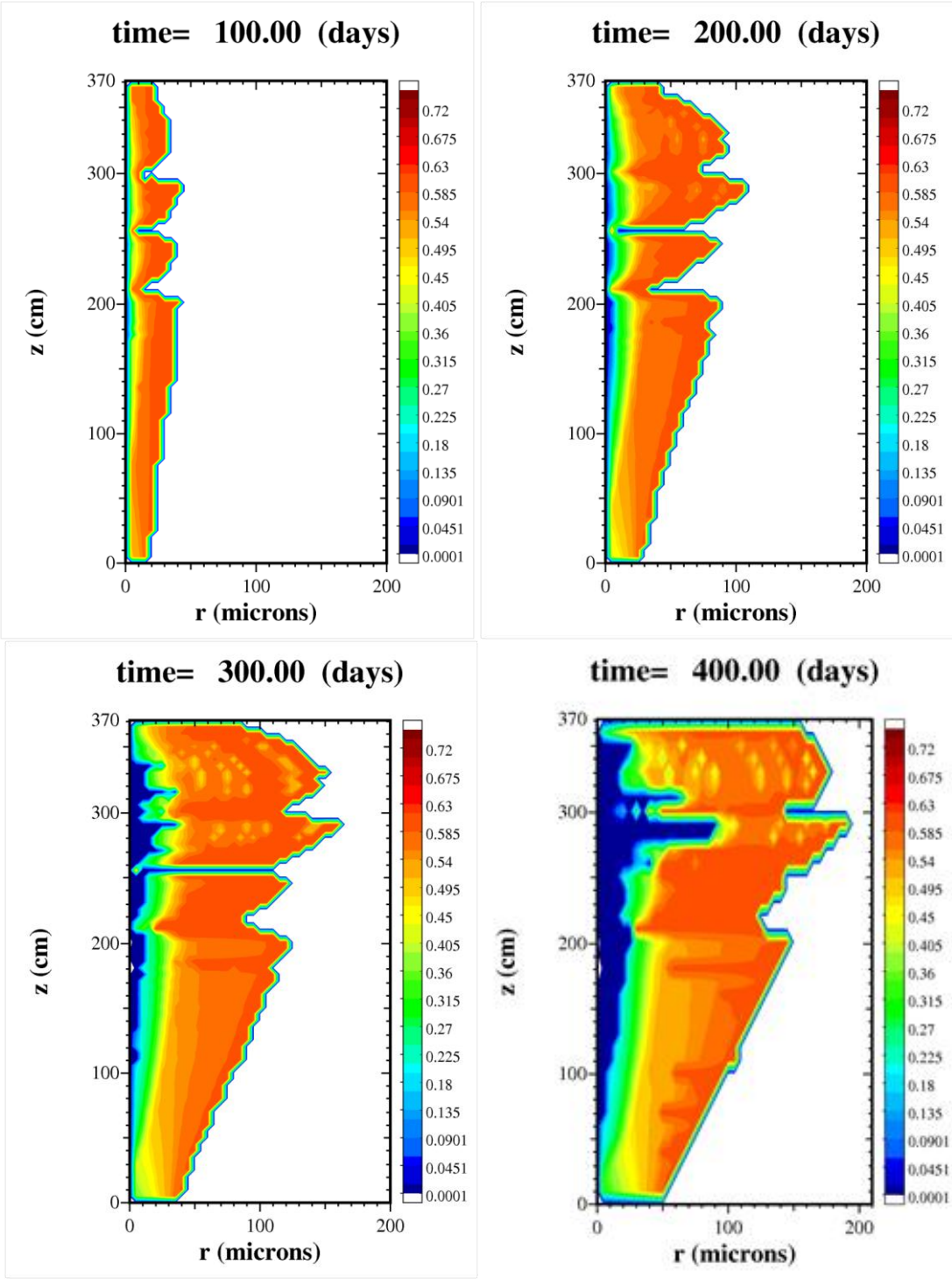

Figure 28 Same as in Figure 27 except that the porosity of the crud layer is plotted. The porosity decreases as nickel-ferrite (yellow-green) and lithium tetraborate (blue) precipitate and deposit within the crud's pores.

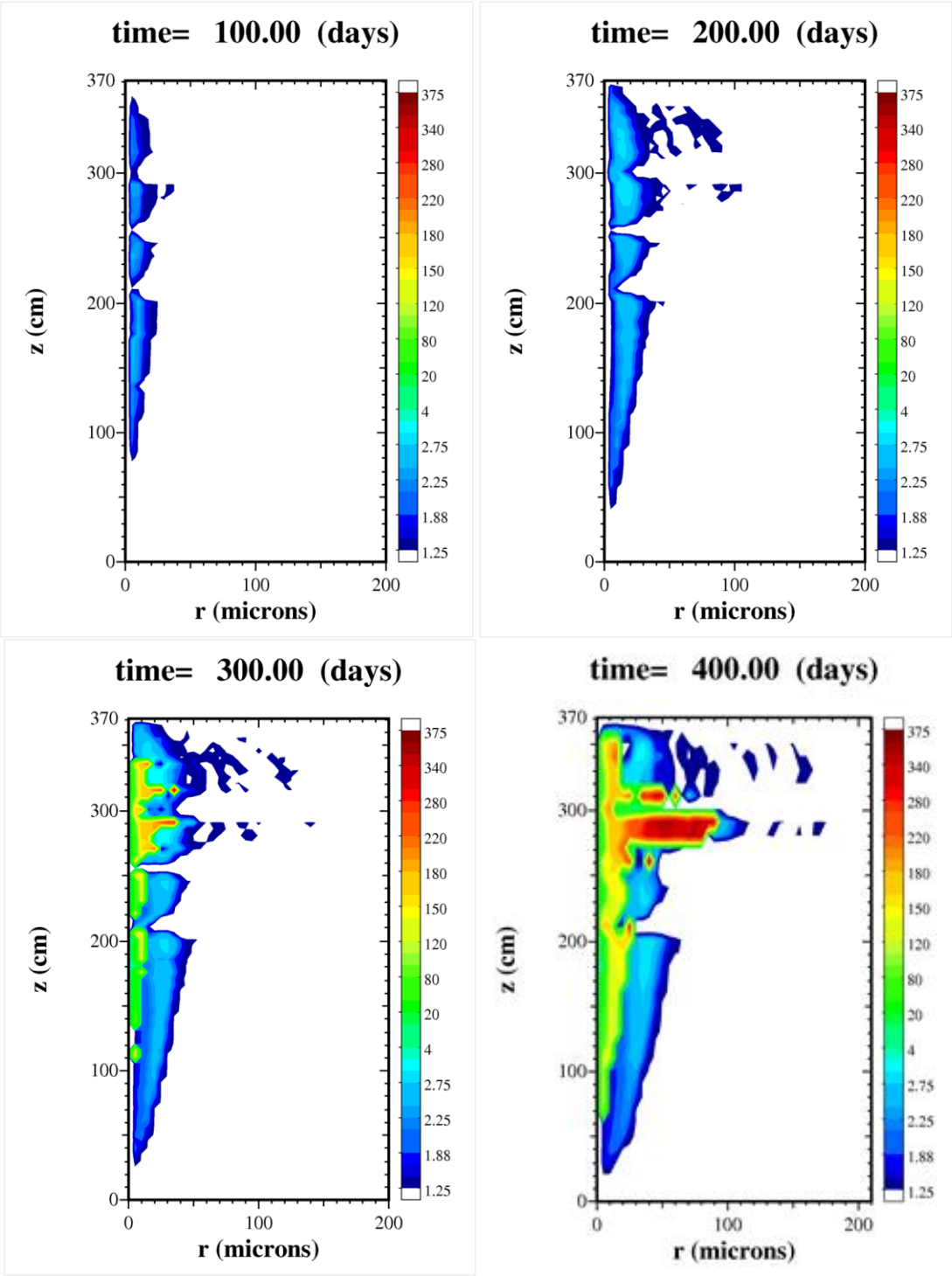

Figure 29 Same as in Figure 27 except that the boron concentration (mg/cm^3) within the crud layer is plotted. The lower concentration (blue) regions correspond to boron in the form of soluble boric acid while the higher concentration (green-yellow-red) regions correspond to boron in the form of solid lithium tetraborate.

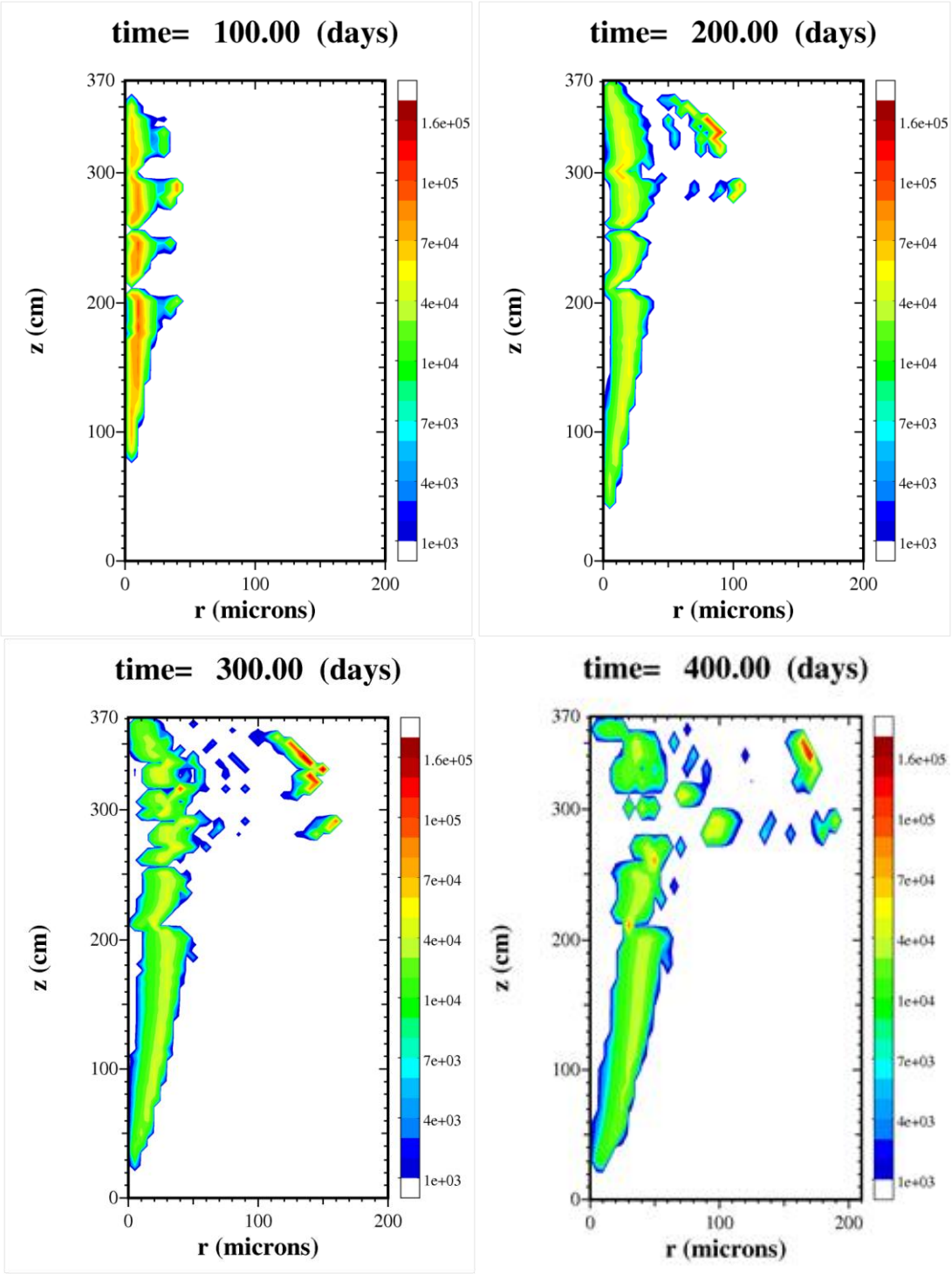

Figure 30 Same as in Figure 27 except that the local boiling heat power density (W/cm^3) is plotted. The heat power density is largest in the hottest regions typically near the cladding surface. Some superheating at the crud's surface is observed near z=290 and 330-360 cm.

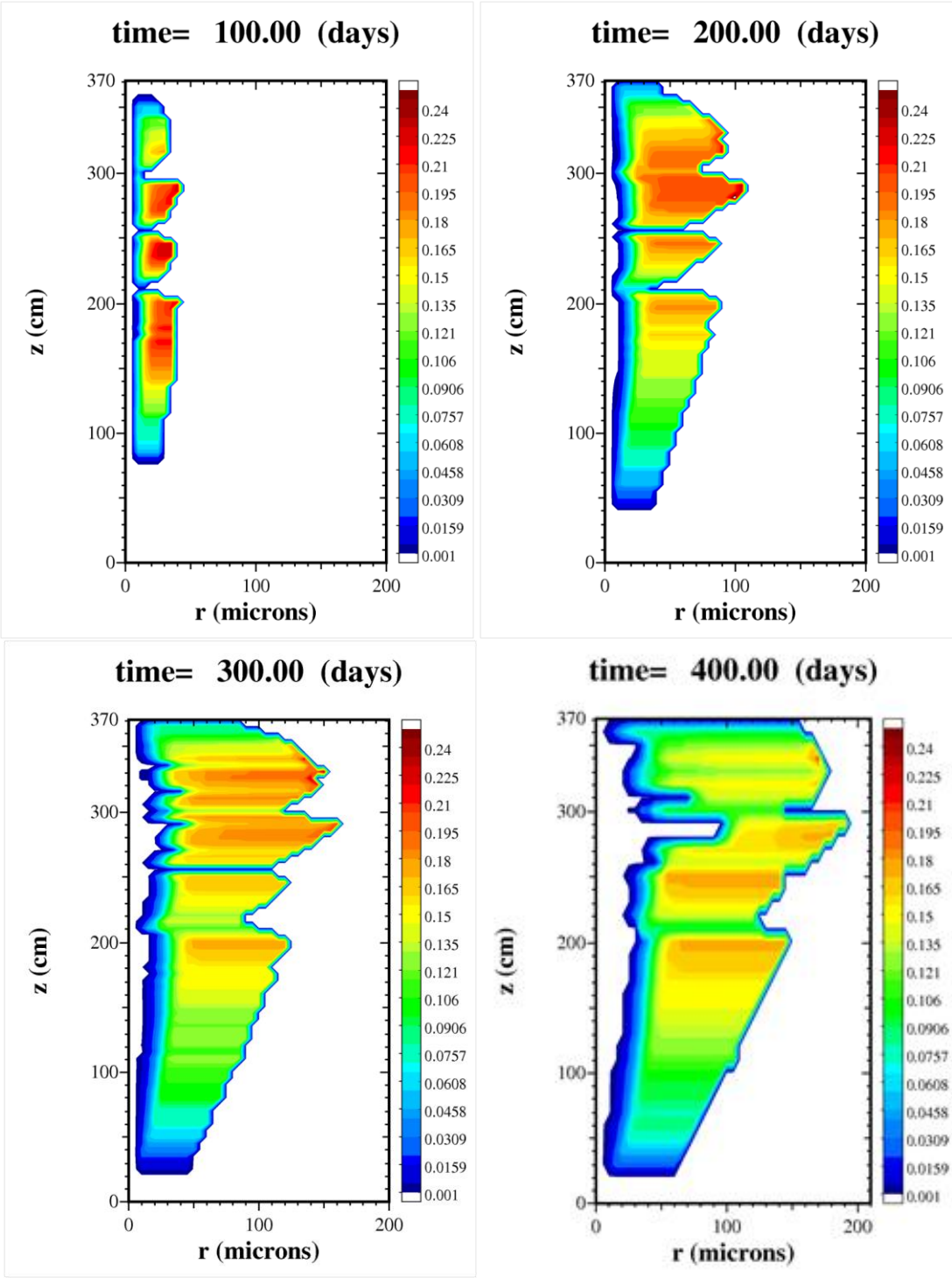

Figure 31 Same as in Figure 27 except that the boiling velocity (cm/s) is plotted. Internal boiling within the crud layer induces substantial flow of coolant into the crud's surface. This fluid flow represents an important mass transport mechanism for concentrating the various soluble species deep inside the crud layer.

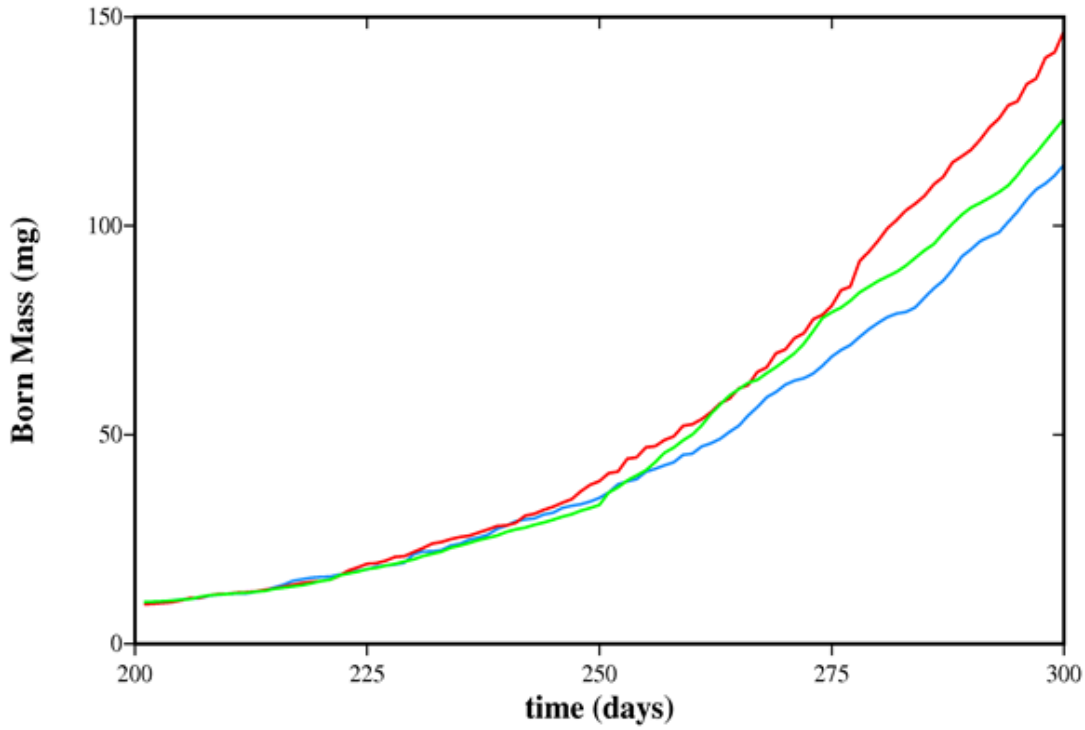

Figure 32 The total boron mass on the fuel rod is plotted as a function of time using three different grid resolutions. The green curve corresponds to the high resolution case (dz=5cm and dθ=20°). The red and blue curves correspond to larger values of dz=10cm and dθ=40°, respectively. Note that the high boron mass is a result of exaggerated assumptions on both boron concentration in the coolant and high crud surface deposition rates.

During the course of the 400 day simulation, the MAMBA grid resolution was decreased in order to keep the computational times reasonable. The high resolution grid was used through 200 days, the dZ=10cm grid was then used from 200-300 days, and a lower resolution grid with both (dZ=10cm and dθ=40°) was used for the final 300-400 days of the simulation. The CPU times (on a single 3.0 GHz Intel E8400 processor) for the first four 50 day intervals using the high resolution grid were 0.3, 2, 6, and 16.5 hours, respectively. The CPU time increases with simulation time due to the increasing crud thickness and number of active grid points. The corresponding grid sizes at the end of each of these first four 50 day intervals was 3658, 7151, 11357, and 16192, respectively. The CPU times for the 200-250 and 250-300 day intervals on the lower resolution dZ=10cm grid were 6.5 and 11 hours, respectively. The corresponding grid sizes were 10973 and 12788, respectively.

The CPU times for the 300-350 and 350-400 day intervals using the lower resolution dZ=10cm and dθ=40° grid were 8 and 10 hours, respectively. The corresponding grid sizes were 7208 and 7903, respectively. During the final 300-400 day interval, the calculations became much slower due to the thick crud layer and non-linear physics and chemistry that were occurring (i.e. rapid lithium tetraborate precipitation and increased boiling). These effects slowed convergence and required smaller internal time stepping by MAMBA.

In summary, the total MAMBA CPU time for the 400 day coupled simulation was 24.8 + 17.5 + 18 = 60.3 hours. It is important to note that the grid resolution was maintained as high as possible. In typical applications, this high grid resolution will probably not be required. A lower resolution MAMBA simulation utilizing a grid with both dZ=10cm and dθ=40° can complete a full rod, 400 day simulation in 6-8 hours (depending upon the crud thickness). A follow-up higher resolution simulation can then be continued overnight focusing on regions of interest (see for example Figure 22). In regards to treating multiple rods, an independent MAMBA calculation can be initiated for each fuel rod of interest using a separate processor (i.e. it is "embarrassingly parallel" with respect to the number of fuel rods). Thus, on a large computer, hundreds of fuel rods could be easily simulated within a matter of hours. It is also important to note that the current version of MAMBA has not yet been optimized for performance. It is anticipated that future algorithm improvements will reduce all of the simulation times by at least a factor of 2 to 4. Additional improvements might also include parallelizing the single rod calculation across groups of 2 to 8 CPUs (albeit with less than ideal scaling) to take advantage of shared-memory, multi-core architectures.

DeCART Neutronics Results

This section summarizes the DeCART results and includes comparisons of the axial offset (AO) and of the axial power profile to quantify the effect of crud deposition on the reactor physics. The AO percentage is calculated as the ratio of the difference between the integrated power in the top and bottom halves of the core and the sum of these integrated powers, which is multiplied by 100 to get in percent:

$$AOA\ (\%) = \frac{P_t - P_b}{P_t + P_b} * 100$$

DeCART cases were performed for each of three different resolutions of the axial and azimuthal discretization which were used in the MAMBA calculation. There were two primary reasons for altering the MAMBA mesh: (1) to perform mesh sensitivity studies on the AOA and power profiles; and (2) to control calculation run time. As the crud deposition and crud removal physics in MAMBA become increasingly non-linear and the calculation time increased considerably. As a result, the MAMBA mesh resolution was altered during the 400 day depletion to achieve reasonable run times. Refer to Table 3 for the different MAMBA discretizations, and refer to Table 4 for the three different cases and how the MAMBA discretization changes during depletion. The axial and azimuthal discretizations were modified, while the radial mesh was kept constant at 5 microns. It is important to note that only the MAMBA discretization was changed during the burnup. The DeCART and STAR-CCM+ meshing remained the same throughout the burnup cycle for all cases.

Table 3 - Summary of MAMBA axial, azimuthal, and radial discretizations

Resolution	Discretization		
	axial (cm)	azimuthal (deg)	radial (μm)
high	5.0	20.0	5.0
mid	10.0	20.0	5.0
low	10.0	40.0	5.0

Table 4 - Summary of the MAMBA meshing used in the three cases

Case	Resolution used within Depletion Range (EFPD)		
	0-200	225-300	325-400
A	high	mid	low
B	high	mid	mid
C	high	high	high

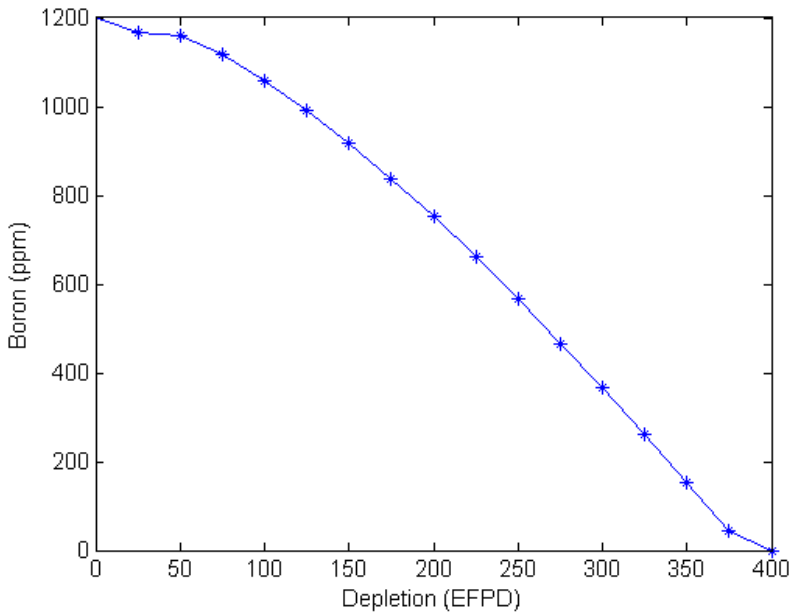

Figure 33 Boron letdown curve for 0 to 400 days depleted

The MAMBA mesh shown in Case A was used to generate the primary results, which are included in the following section. Case B results are included within the Appendix 2. Case C will be completed in future work, and will provide comparisons of all three resolutions and their impact on the results. In the case A that is shown here the boron letdown curve was assumed linear from 1200 ppm at the beginning of cycle to 0 ppm at end of cycle as shown in Figure 33.

The axial offset anomaly with and without crud modeling for Case A is shown in Figure 34. Because the crud/boron mixture preferentially deposits along the upper third of the fuel rod, the power is shifted from the top of the core toward the bottom. As expected the power begins to shift at approximately 250 days, which corresponds to the time when the boron deposition rate within the crud layer increases significantly. The total boron mass in the crud deposit during the burnup cycle is shown in Figure 35. As indicated there is a substantial increase in the boron uptake in the crud starting at about 250 days.

As discussed previously, it is important to note the limitations of the results presented here. While the DeCART simulations are based on the typical boron letdown curve shown in Figure 10, the crud deposition rate predicted by MAMBA was obtained using a fixed boron concentration of 1600 ppm in the coolant. It should also be noted that the magnitude of the AO

for the case without crud shown in Figure 34 is larger than observed in operating PWRs. The simple pin model used here with reflective boundary conditions cannot be expected to accurately capture the axial power shape that would occur in a typical PWR.

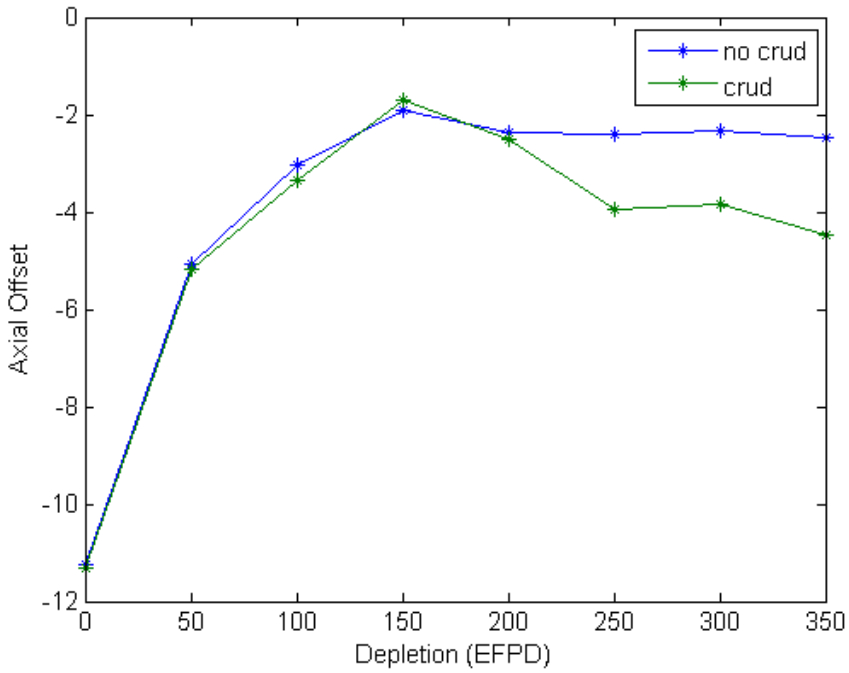

Figure 34 AO comparison of no crud and crud cases

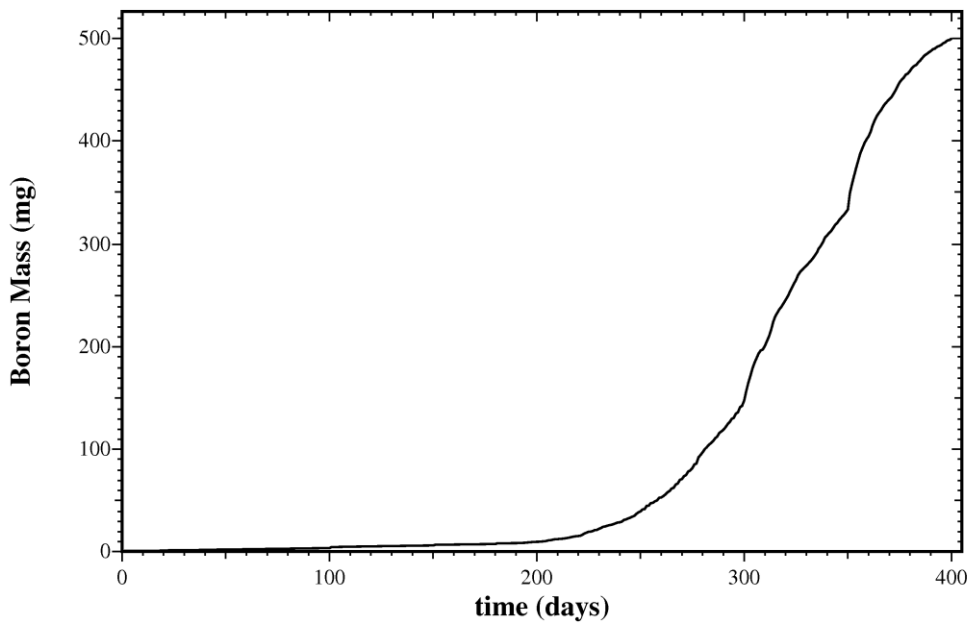

Figure 35 Total Boron in the crud deposit during the Burnup Cycle predicted by MAMBA

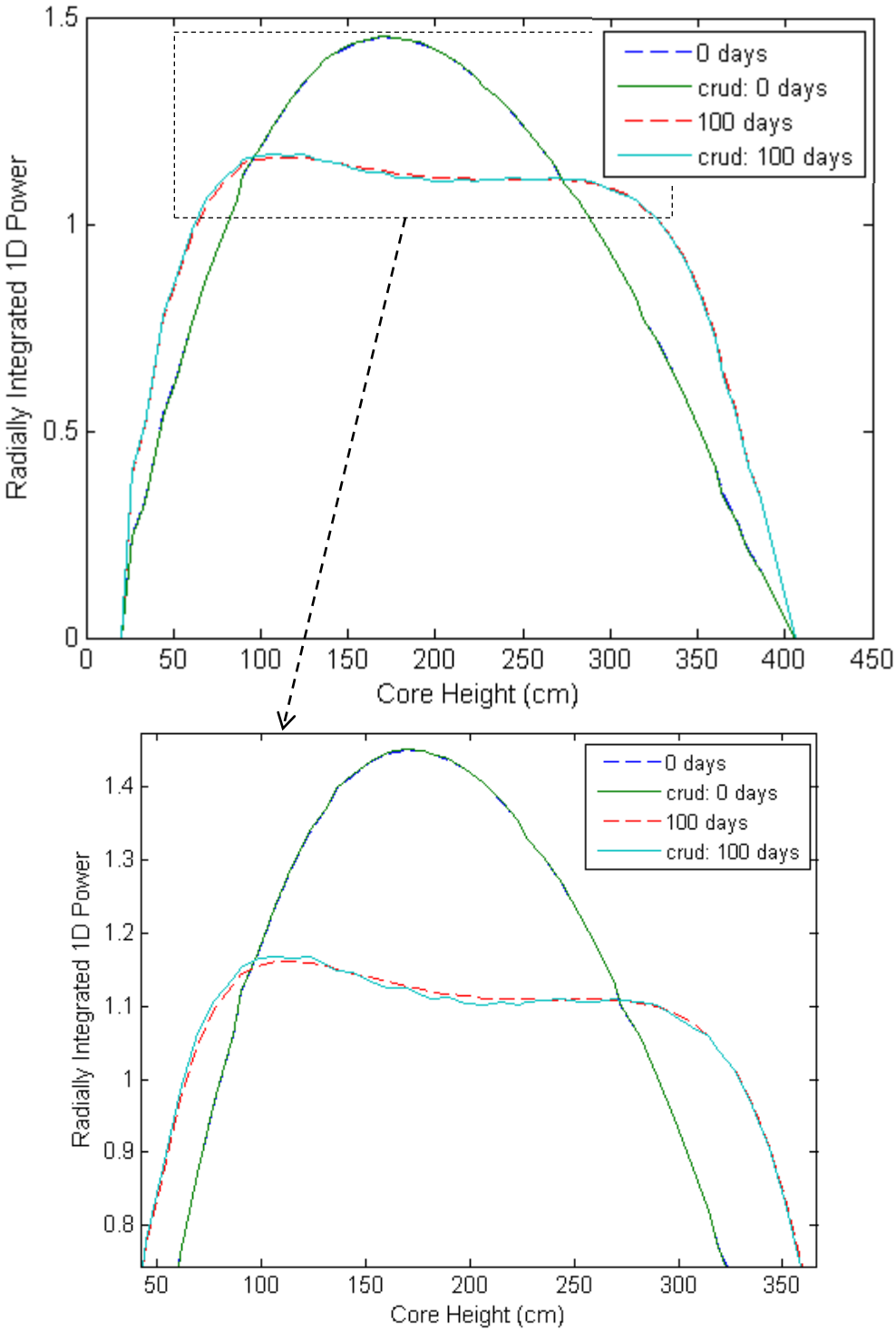

Figure 36 Axial power profile comparison of no crud and crud cases 0 and 100 effective full power days depleted.

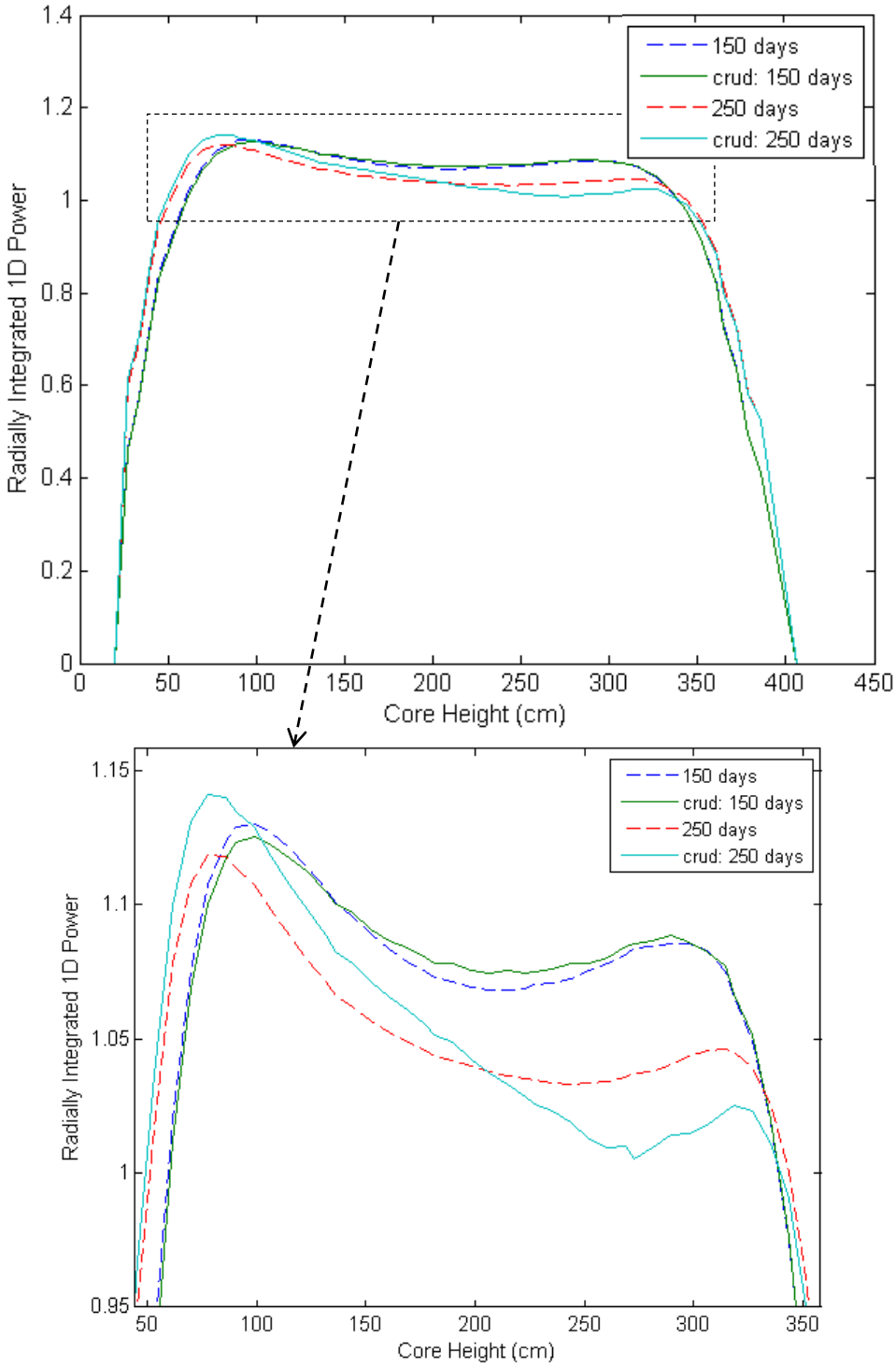

Figure 37 Axial power profile comparison of no crud and crud cases 150 and 250 effective full power days depleted.

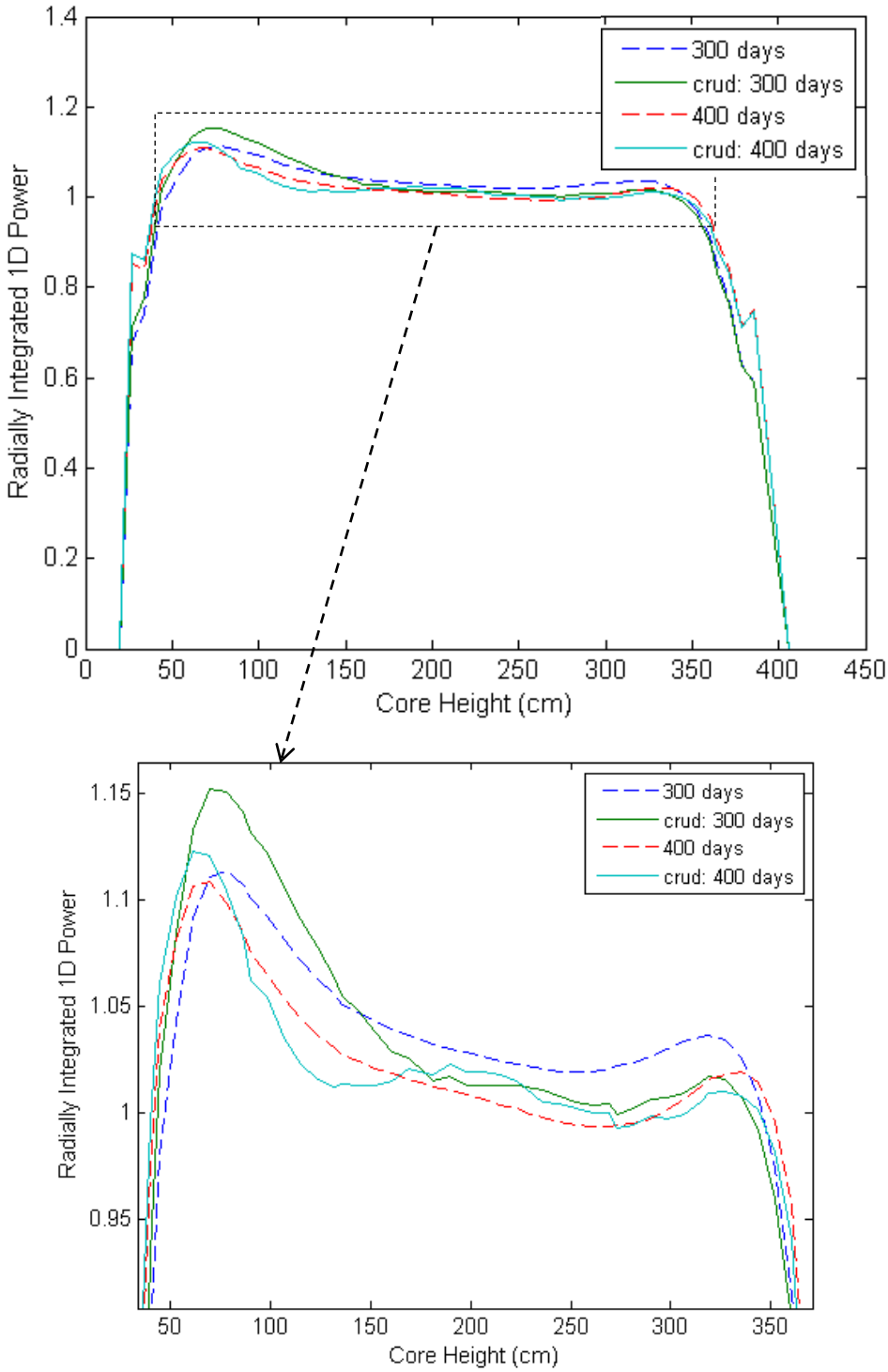

Figure 38 Axial power profile comparison of no crud and crud cases for 300and 400 effective full power days depleted.

The axial power shapes at several points in the burnup cycle for the cases with and without crud are shown in Figure 36 to Figure 38. Figure 36 shows the axial profiles for 0 and 100 days and as expected there is little difference early in the burnup cycle.

As shown in Figure 37, the crud deposition begins to have a neutronic impact by 150 days since a sufficient amount of boron is deposited in the upper regions of the core and the power shifts slightly to the bottom of the core. The power shift becomes even more noticeable by 250 days when the AO has increased to about 4%. Figure 38 shows the bottom-shifted power distribution late in the cycle. It should be noted that the discontinuities at each end of the core are due to the simplified modeling of the top and bottom water reflector regions in STAR-CCM+. More realistic reflector region representation will be used in subsequent models.

Summary and Conclusions

This report documents the completion of an initial (pin scale) multiphysics simulation of crud deposition by coupling the results of the codes MAMBA (crud), DeCART (neutronics), and STAR-CCM+ (thermal hydraulics). The objective of the work here was to satisfy the CASL Milestone L1.CASL.P4.02 with the primary goal of providing an initial demonstration of Crud deposition physics which included the computation of the thickness/composition of crud layer, temperature, heat flux in/out, and boron distribution within the crud layer along the surface (or selected surface regions) of a single pin from a 3D 3x3 geometry. The optional goals included an initial demonstration simulation with couplings between MAMBA and both CFD (STAR-CCM+) and neutronics (DeCART).

In summary, both the primary and optional goals of this L1 have been met using the initial advanced (pin scale) coupled DeCART/STAR-CCM+/MAMBA multiphyiscs simulation approach. Two-way coupling between each of the three codes has been implemented and applied to the assessment of CIPS risk for a 3D geometry consisting of a single fuel rod with three spacers (each spacer contains four mixing vanes). This particular geometry was chosen for the initial coupled demonstration simulation in order to minimize the computational requirements and to focus on the coupling interfaces. Future studies will include the treatment of additional spacers and multiple fuel rods within a larger sized sub-assembly (i.e. a 4x4 pin geometry).

The crud thickness and boron uptake within the three-dimensional crud layer along the entire surface of the pin was computed as a function of time by the MAMBA 3D v2.0 computer code. The cladding surface heat flux, crud surface temperature, and the surface turbulent kinetic energy required by MAMBA were computed by a coupled DeCART/STAR-CCM+ calculation. The resulting 3D boron distribution computed by MAMBA was used by DeCART to assess the effects of the boron layer on the power distribution along the length of the pin (i.e. the CIPS risk). The coupling (data exchanges) between the three codes was initiated at 25 and 50 day time intervals extending over a 400 day cycle. A high-resolution ("zoomed in") MAMBA/STAR-CCM+ coupled simulation for the region around the first spacer grid was also performed.

Interesting azimuthal variations due to the mixing vanes were observed. The swirling/turbulent flow through the mixing vanes leads to significant azimuthal temperature variations on the cladding surface as well as to increased surface erosion of the crud layer. Both of these fluid induced effects alter the local crud deposition rate and thickness giving rise to "streak" deposits which have been observed in operating PWRs. "Hot spots" on the cladding surface were also observed in regions of thicker crud deposits which increases the risk for CILC (Crud Induced Localized Corrosion). The impact of the crud deposition on the axial offset was clearly observed, with a noticeable increase in the AO at about 250 days into the burnup cycle when the crud deposition rate increases significantly. The preliminary results from this study demonstrate the importance of a coupled simulation approach for capturing observed reactor core phenomena leading to CIPS and CILC and most importantly for improving the risk assessment of these industrial relevant effects.

It is important to remember that the work performed here was intended to be a "Proof of Concept" of the ability to perform multiphysics, coupled code simulation of crud deposition, and therefore caution should be used in interpreting the quantitative results on crud deposition and AOA. An aggressive combination of a thick crud layer (generated by assuming a high crud surface deposition rate in the MAMBA model) and a high boron concentration in the coolant were used in this initial demonstration simulation to provide a noticeable boron deposition within the crud and to increase the likelihood of a detectable power shift in the single rod neutronics calculation. More realistic scenarios based on realistic plant data will be used in future work.

Future Work

It is proposed to continue the proof-of-concept activity illustrated in this report in six principle areas:

1. Software development
2. Investigation of the impact of thermal-hydraulic modeling (meshing and fidelity of grid spacers representation) on the prediction of crud deposition
3. Investigation of the impact of crud deposition on neutronics predictions due to DeCART meshing
4. Sensitivity study of crud deposition predictions on thermal-hydraulic parameters
5. Extended demonstration of full DeCART/STAR-CCM+/MAMBA coupling capabilities for the prediction of crud deposition
6. Validation of Crud deposition using WEC experimental facilities

It should be noted that while it is currently proposed to continue using STAR-CCM+ as the CFD code, the results and conclusions obtained in the proposed investigations are expected to apply to the CFD codes DREKAR and HYDRA-TH since all the proposed studies are based on single-phase RANS turbulence modeling. Similarly, while the neutronics effort proposed here in the near term is to continue to use the models developed in DeCART, the proposed investigations and any code modifications will be extended to the neutronics codes DENOVO and MPACT.

<u>1. Software development</u>

The following activities were determined necessary for the development of a RSICC quality computational tool for high-fidelity simulation of crud deposition:

a) development of MAMBA/STAR-CCM+ and MAMBA/DeCART interfaces for automatic data exchange within LIME; data exchange through files will be substituted with data exchange through data arrays memory storage. This will allow saving clock time needed for reading/writing access operations on hard drive.

b) development of time-stepping and convergence algorithms for full coupled simulations with the DeCART/STAR-CCM+/MAMBA code system;

c) development of ability to concurrently model crud and grid spacers in DeCART.

2. Impact of TH modeling (meshing and grid spacers) on the prediction of crud deposition

The study presented in this report has demonstrated that the impact of grid-spacer-induced flow swirling on the location of hot spots in the fuel cladding is a principle contributor to the formation of the characteristic crud striping patterns observed with crud deposits on the fuel rods surface. Other important contributors to the striping patterns are asymmetries in the azimuthal power distribution within a pin, and the erosion of the crud layer induced by the shear stress (or turbulent kinetic energy) exerted by the fluid on the crud surface. In order to systematically investigate these effects, it is proposed to model a 4x4 fuel pin sub-assembly region as depicted in Figure 39. Initially, it is proposed to use an imposed power distribution and then in a second phase to activate neutronics feedback. In this way it is possible to study first how the prediction of crud deposition is impacted by the resolution of the fluid-dynamic solution and by the fidelity used to represent the grid spacers, excluding the concurrent effect of neutronic feedback on the power distribution. The neutronics effect will be included in a second stage of the investigation.

For this study, it is proposed to select a 4x4 sub-assembly out of an existing quarter core simulation of a Combustion Engineering PWR previously performed at the University of Michigan by means of DeCART/STAR-CCM+ (Kochunas et al., 2012). It has to be noted that the STAR-CCM+ model in this simulation was very coarse and did not include explicit modeling of the grid spacers. The pin power distribution that was obtained for this problem is shown in Figure 39 (left), together with the 4x4 sub-assembly selected for the proposed study. The geometry of the grid spacer is presented in Figure 39 (right) and is again based on the specifications by Navarro and Santos (2011).

The 4x4 sub-region has been chosen such as to include hot pins, and to have strong power variations in space, both from pin to pin as well as azimuthally within a single pin (this is achieved by including pins located in the proximity of water rods and burnable absorbers).

The cladding temperature distribution will be calculated using the following modeling options:

- CFD solution (using STAR-CCM+)

  Mesh
  - coarse mesh
  - fine mesh

  Spacers modeling
  - explicit
  - porous body

- Subchannel solution (using COBRA-TF)

  Mesh
  - coarse mesh (one node per subchannel)
  - fine mesh (multiple nodes per subchannel)

The cladding temperature distributions obtained in this way will be transferred to MAMBA in order to systematically assess how the prediction of crud deposition is impacted by the level of resolution of the fluid-dynamic simulations.

By studying how the thermal/fluid-dynamic solution (azimuthal cladding temperature, etc.) is impacted by the approximations in the fluid-dynamic models (coarse mesh vs fine mesh, grid spacers vs porous body approach, CFD vs subchannel code), it will be possible to address other questions often raised during CASL meetings, namely in which cases a subchannel simulation is sufficiently good, when a CFD solution is needed instead, and in which cases a CPU-intensive explicit modeling of grid spacers is crucial for a correct representation of the problem under examination.

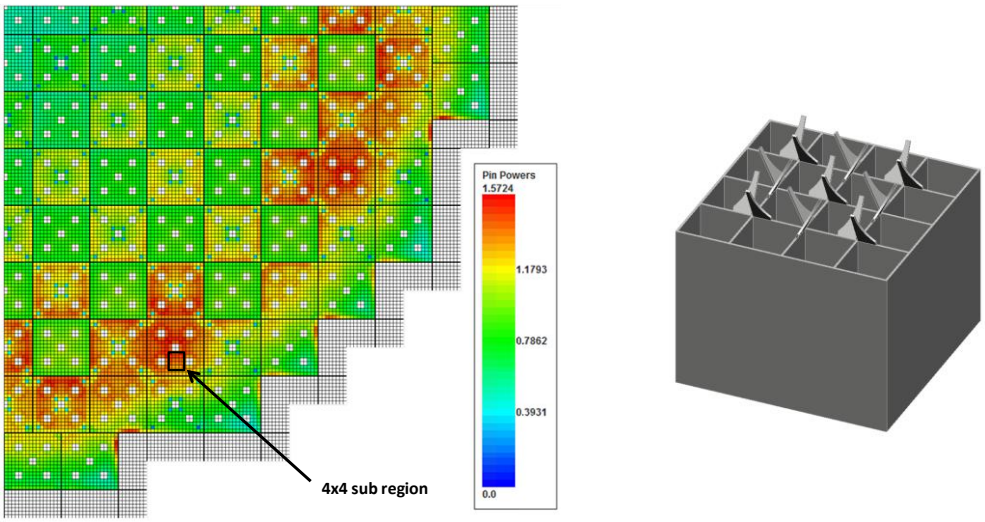

Figure 39 Selected 4x4 sub-region from quarter core simulation by Kochunas et al., 2012 (left), and fuel spacer adapted from Navarro et al., 2011 (right).

3. Sensitivity analysis of impact of neutronics modeling on crud deposition

Upon completion of the initial phase of the 4x4 pin cell analysis with only CFD/MAMBA coupling, the neutronics feedback will be activated and a study will be initiated on the impact of neutronics modeling parameters on the detailed neutronics/CFD analysis. This will include an analysis of (1) neutronics meshing, (2) boron depletion.

(1) In the current study, a single radial region and 16 azimuthal regions were used to model the crud deposition. The three-dimensional meshing effects on the crud are not well quantified and must be investigated to fully understand the approximation of homogenizing the crud within the DeCART flat source regions.

(2) Boron will be depleted throughout the cycle, which will directly impact the boron uptake within the crud; thus, it is important to quantify this relationship. Explicit modeling of the boron concentration (letdown) throughout the cycle depletion should be used in DeCART then passed to MAMBA at each file exchange or in the time stepping algorithm.

4. Sensitivity study of crud deposition predictions on thermal-hydraulic parameters

This investigation is focused on:

- sensitivity of the crud deposition predicted by MAMBA as function of fluid-dynamic parameters such as turbulent kinetic energy, azimuthal temperature distributions, etc.
- sensitivity of the CFD solution on changes of wall roughness caused by crud deposition. Depending on the obtained results, it might be necessary to include the modeling of wall roughness in the data exchange between MAMBA and STAR-CCM+.
- detailed investigation of the convergence properties, accuracy, and consistency of the MAMBA and STAR-CCM+ coupling approach.

  A MAMBA computed effective thermal resistance will be used by STAR-CCM+. A coupled DeCART/STAR-CCM+ calculation will provide the cladding heat flux to MAMBA. The accuracy of the MAMBA/STAR-CCM+ coupling will be quantified by comparing the MAMBA computed cladding temperature to the coupled DeCART/STAR-CCM+ computed cladding temperature as a function of time stepping (10, 25, 50 days) and crud thickness for the first 100 day period of a cycle. Two approaches will be investigated for setting the boundary conditions at the crud/coolant interface for MAMBA: (1) using the STAR-CCM+ computed crud surface temperature and (2) using a STAR-CCM+ computed heat transfer coefficient at the crud/coolant boundary. The optimal set of parameters (time step) and coupling approach (i.e. 1 vs 2) will be determined. This study is critical for scaling the calculations up to larger sized sub-assemblies (4x4, etc) and ultimately full core simulations. Another goal of this study is to make the time stepping automatic by having the coupling algorithm monitor the level of convergence and adjust the time step accordingly.

5. Extended demonstration of full DeCART/STAR-CCM+/MAMBA coupling capabilities

In order to demonstrate the capabilities of the coupled DeCART/STAR-CCM+/MAMBA tool within the LIME platform, a depletion simulation including modeling of crud deposition will be performed for the 4x4 pin model with grid spacers described under task 3.

While running the DeCART/STAR-CCM+/MAMBA tool, 16 separate instances of MAMBA will be run in parallel, each associated to a single pin of the 4x4 subassembly model, respectively. The demonstration problem is selected in such a way that all aspects of the code coupling are challenged and all physical effects are taken into account:

- the fuel heterogeneity and the presence of a water rod will ensure strong pin-by-pin and azimuthal power variations within the fuel assembly;
- the explicit modeling of the grid spacers in the DeCART model, will provide accurate descriptions of the power dips appearing in the axial power profile in proximity of the grid spacers;
- the explicit modeling of the spacers in the CFD model will allow capturing the azimuthal and axial variation of cladding temperature and heat transfer coefficient, important for the

prediction of the "striping" effect observed in crud deposits on fuel rods extracted from nuclear power plants.

The pin type positions that will be used in the coupled depletion model are shown in Table 5. The compositions of the pins are summarized as follows: pin 10 contains UO_2 fuel with 2.87 wt% enriched U-235; pin 13 contains a burnable absorber and is a mixture of 3.37 wt% enriched UO_2 and 6 wt% Gd_2O_3; the center pins (modeled as four quarter pins) makeup a guide tube (water rod). The 4x4 pin array geometry specifications are shown in Table 6.

Table 5: Pin type positions within 4x4 array; includes water rod position.

13	10	10	13
10	water rod		10
10			10
13	10	10	13

Table 6: 4x4 pin array specifications.

Parameter	Value (cm)
Pin pitch	1.285
Fuel rod outer radius	0.48515
Fuel pellet outer radius	0.42165
Guide tube outer radius	0.6125
Guide tube inner radius	0.5625
Active fuel height	393.02353

6. Validation of Crud deposition using WEC experimental facilities

This task is focused on the validation of the MAMBA/STAR-CCM+ coupled code against experimental data on crud deposition obtained at the WEC experimental facility (EPRI, 2011). An outcome of this activity will be recommendations for future experimental designs better suited for the validation of the coupled MAMBA/CFD code (such as the inclusion of a mixing vane and detailed azimuthal temperature measurements).

References

EPRI, 2011. Simulated fuel crud thermal conductivity measurements under pressurized water reactor conditions. EPRI, Palo Alto, CA: 2011. 1022896.

Hursin, M., Kochunas, B., Downar, T., 2009. DeCART v2.05 User's Manual. School of Nuclear Engineering and Radiological Sciences, University of Michigan.

Kochunas B., Stimpson, S., Collins, B., Downar, T., Brewster, R., Baglietto, E., 2012. Coupled Neutron Transport/CFD simulations of whole core pressurized water reactor. Proc. of Int. Conf. On Advances in Reactor Physics, PHYSOR 2012, Knoxville, Tennessee, USA, April 15 - 20.

Navarro, M.A., Santos, A.A.C., 2011. Evaluation of a numeric procedure for flow simulation of a 5x5 PWR rod bundle with a mixing vane spacer, *Progress of Nuclear Energy*, **53**, pp. 1190-1196.

NEI (Nuclear Engineering International), 2012, Heavy crud loading on fuel assemblies in a PWR. http://www.neimagazine.com/graphic.asp?sc=2050914&seq=2

APPENDIX 1 - STAR-CCM+ results

Results at t = 0 days

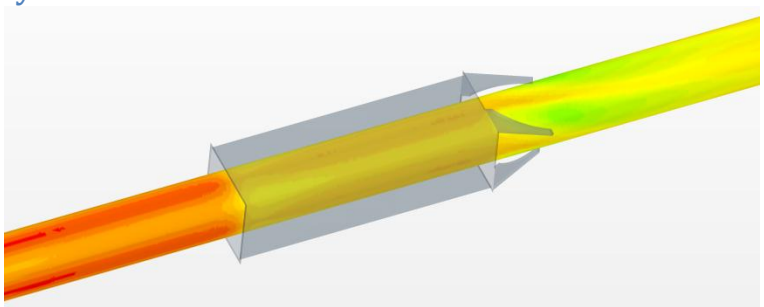

Spacer 1

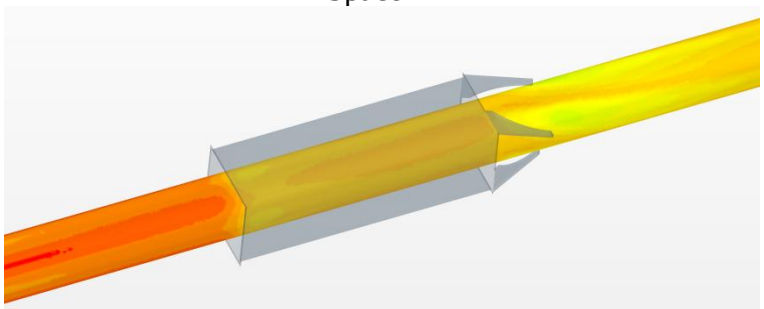

Spacer 2

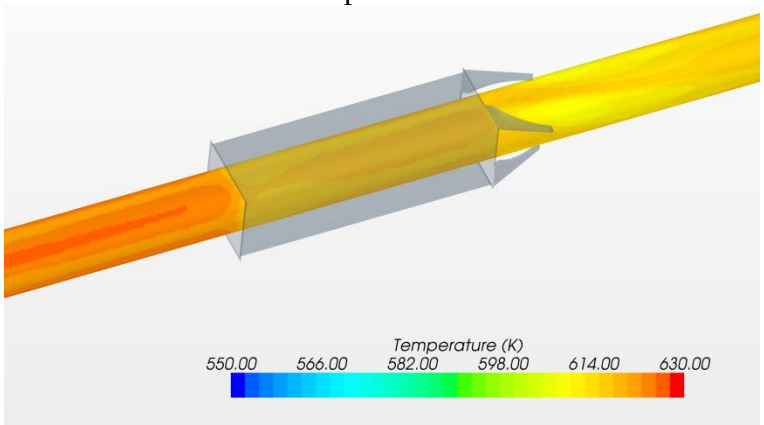

Spacer 3

Figure 40 Crud (cladding) surface temperature at 0 days

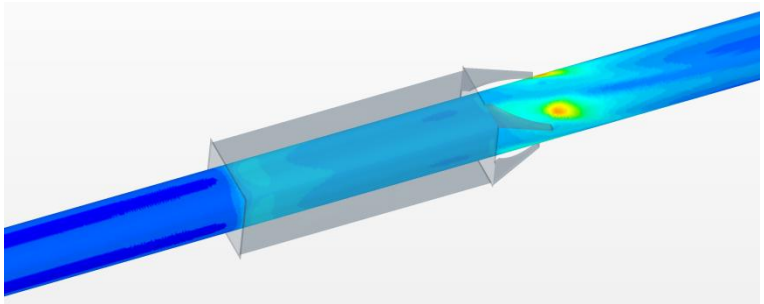

Spacer 1

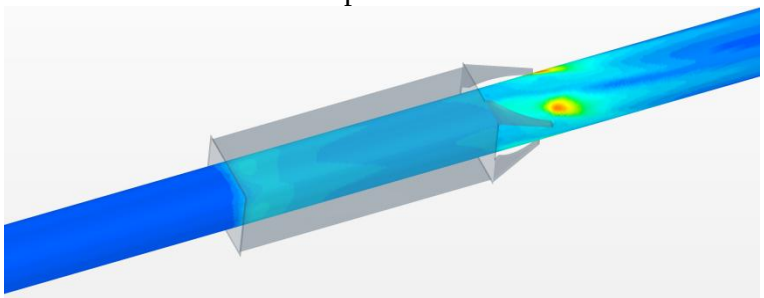

Spacer 2

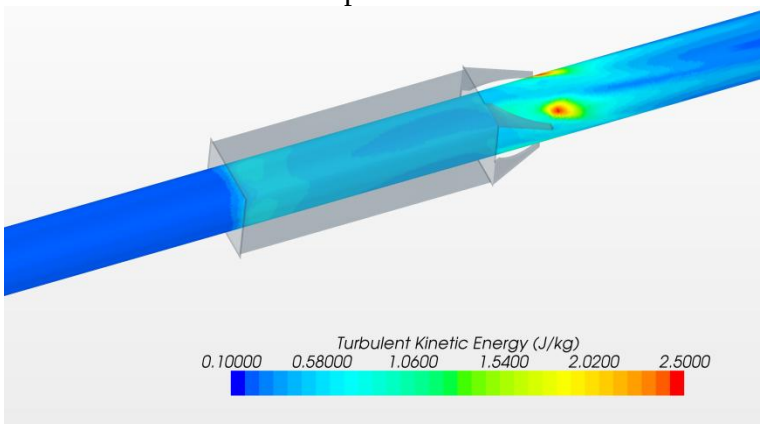

Spacer 3

Figure 41 Turbulence kinetic energy in the boundary layer at 0 days

(a)

(b)

(c)

(d)

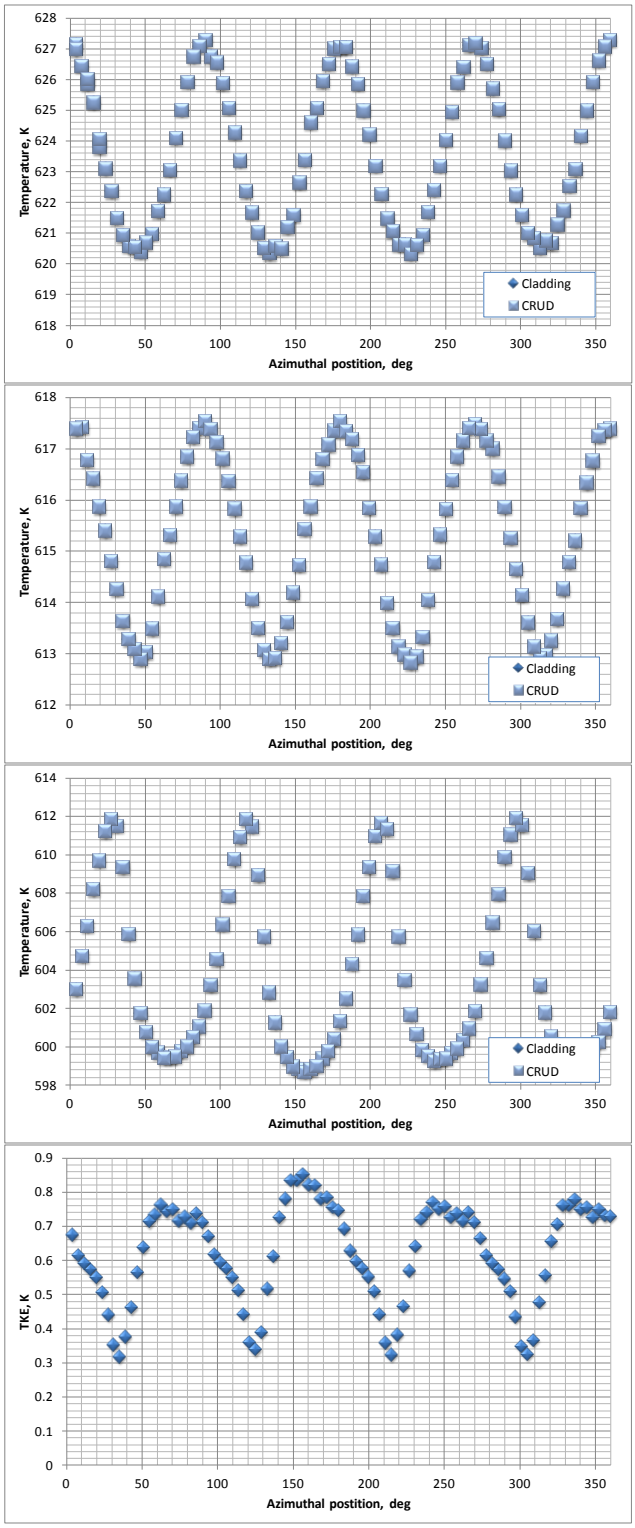

Figure 42 Azimuthal cladding and crud surface temperatures (a) before spacer (b) at the spacer (c) after spacer, and (d) turbulent kinetic energy in the boundary layer after grid spacer - spacer 1. Results at t = 0 days.

(a)

(b)

(c)

(d)

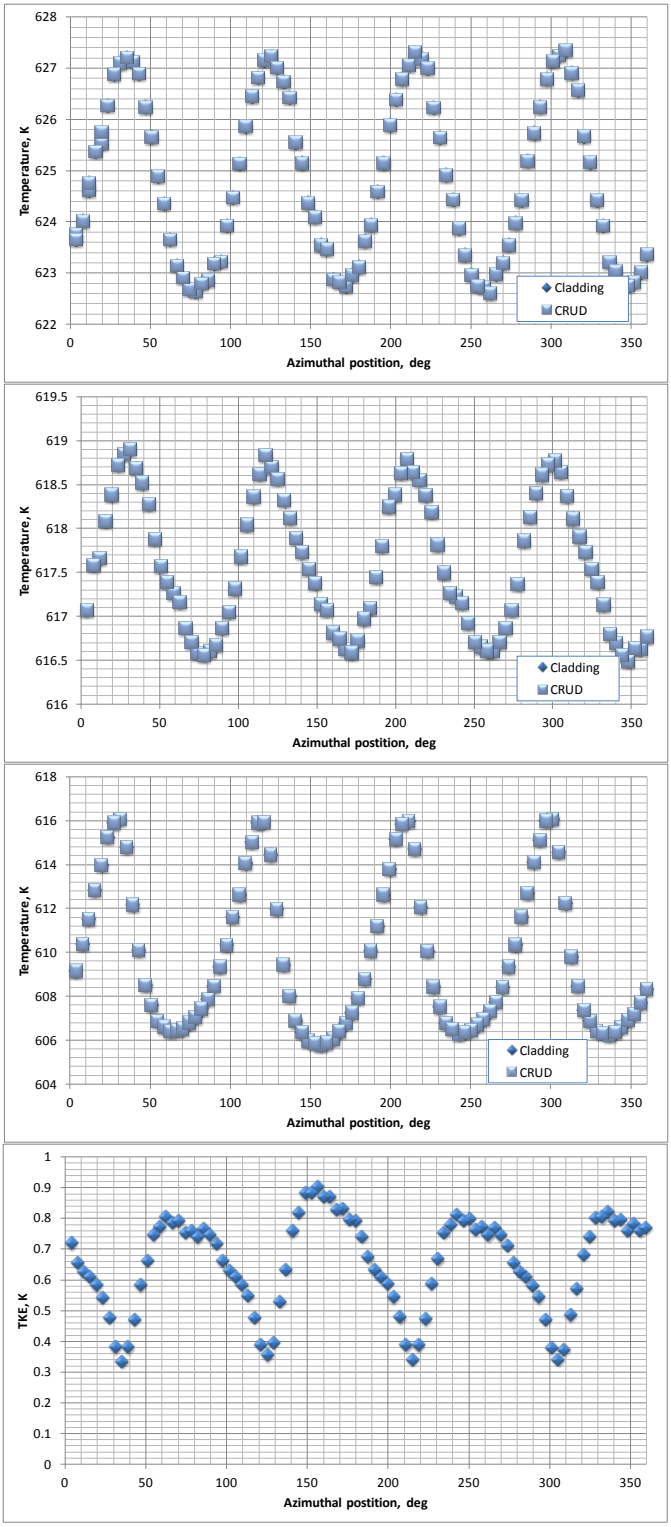

Figure 43 Azimuthal cladding and crud surface temperatures (a) before spacer (b) at the spacer (c) after spacer, and (d) turbulent kinetic energy in the boundary layer after grid spacer - spacer 2. Results at t = 0 days.

(a)

(b)

(c)

(d)

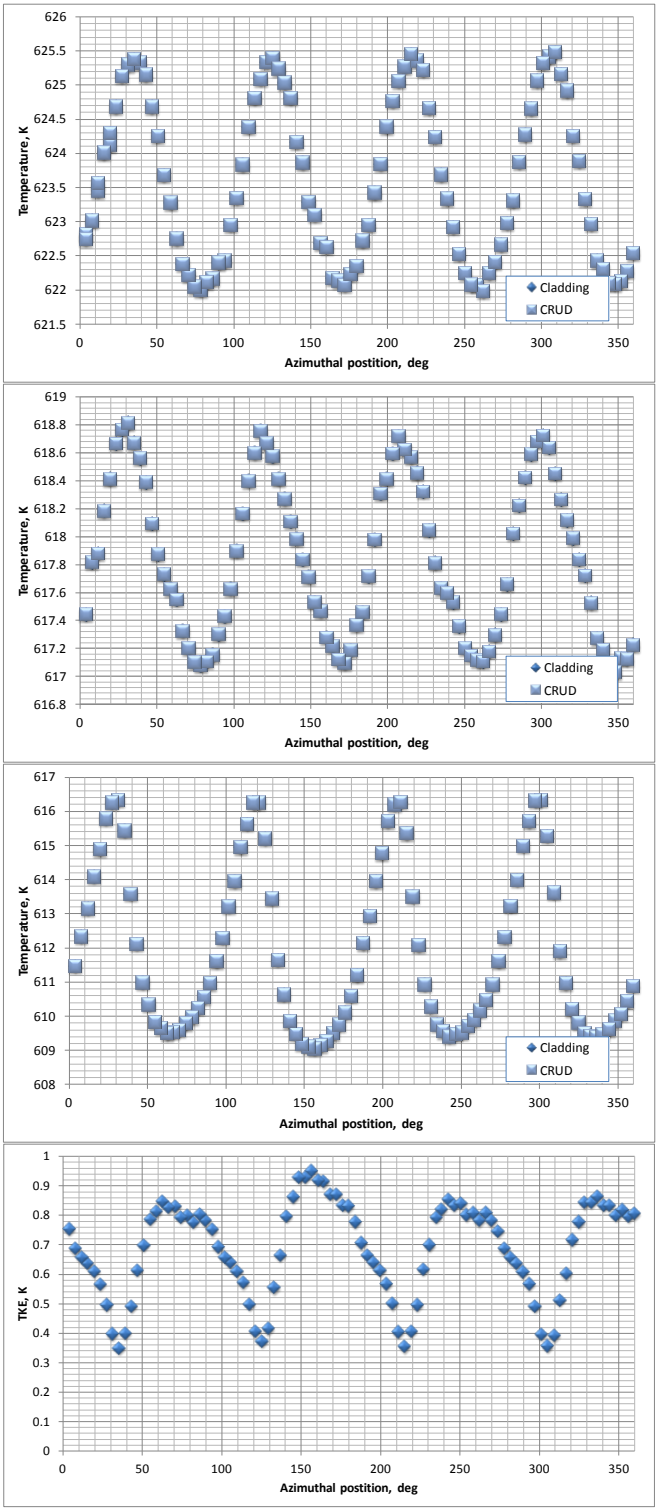

Figure 44 Azimuthal cladding and crud surface temperatures (a) before spacer (b) at the spacer (c) after spacer, and (d) turbulent kinetic energy in the boundary layer after grid spacer - spacer 3. Results at t = 0 days.

Results at t = 100 days

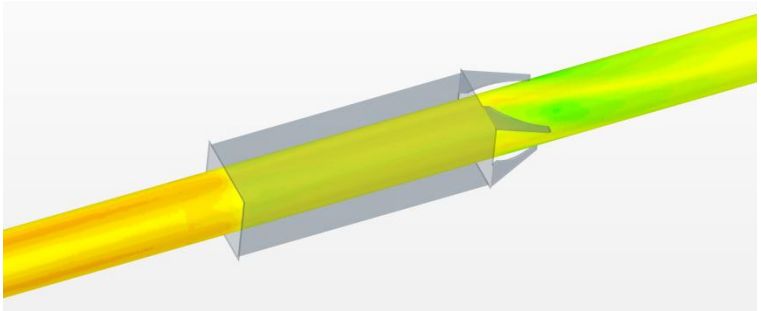

Spacer 1

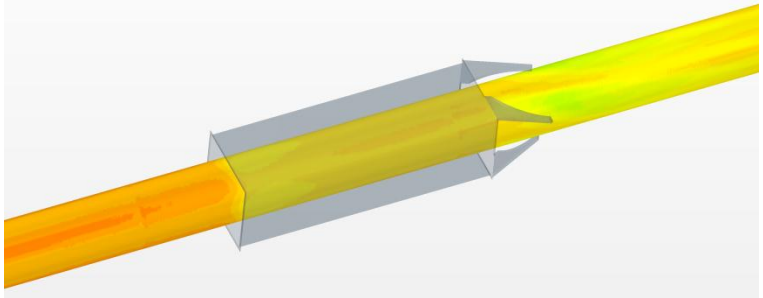

Spacer 2

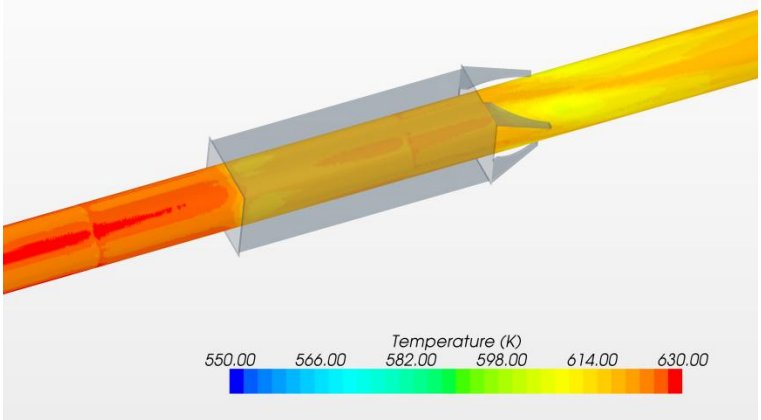

Spacer 3

Figure 45 Crud surface temperature at 100 days

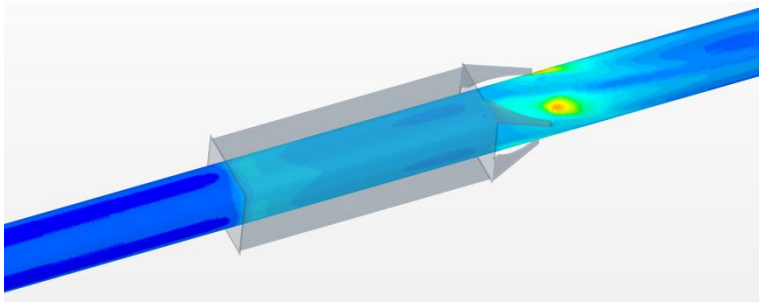

Spacer 1

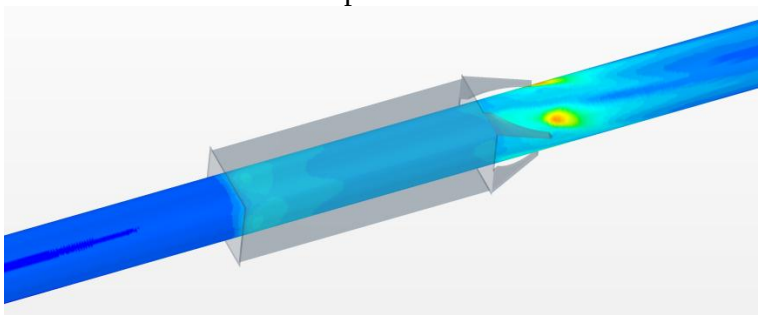

Spacer 2

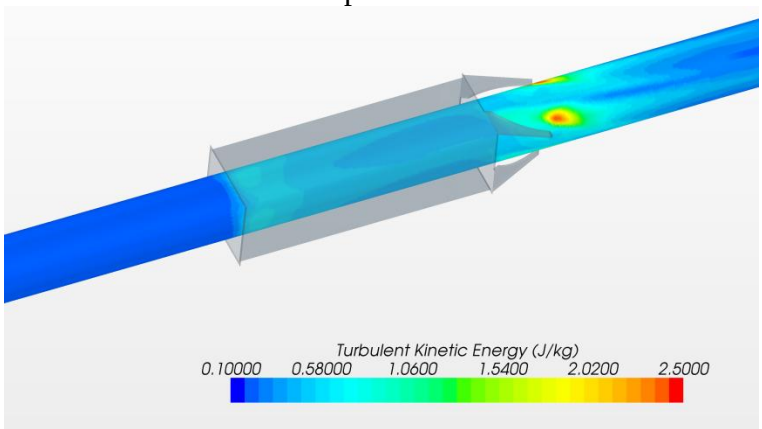

Spacer 3

Figure 46 Turbulence kinetic energy in the boundary layer at 100 days

(a)

(b)

(c)

(d)

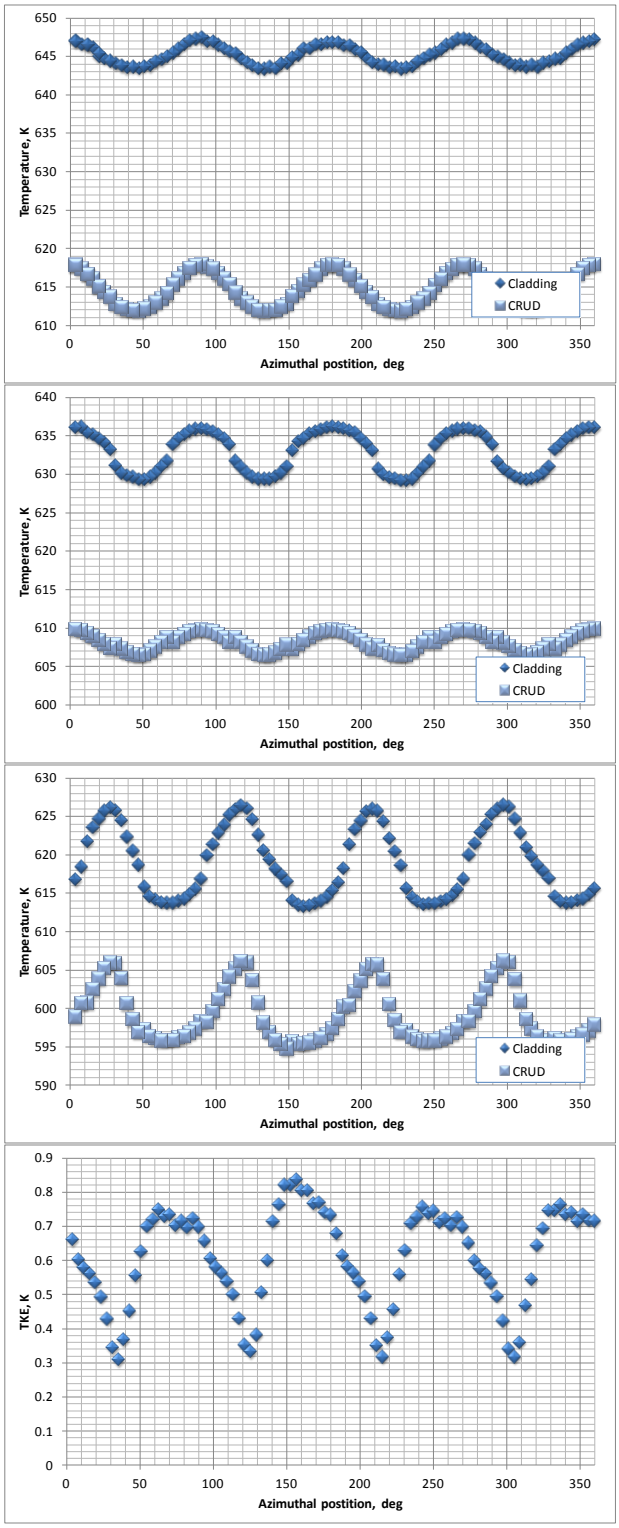

Figure 47 Azimuthal cladding and crud surface temperatures (a) before spacer (b) at the spacer (c) after spacer, and (d) turbulent kinetic energy in the boundary layer after grid spacer - spacer 1. Results at t = 100 days.

(a)

(b)

(c)

(d)

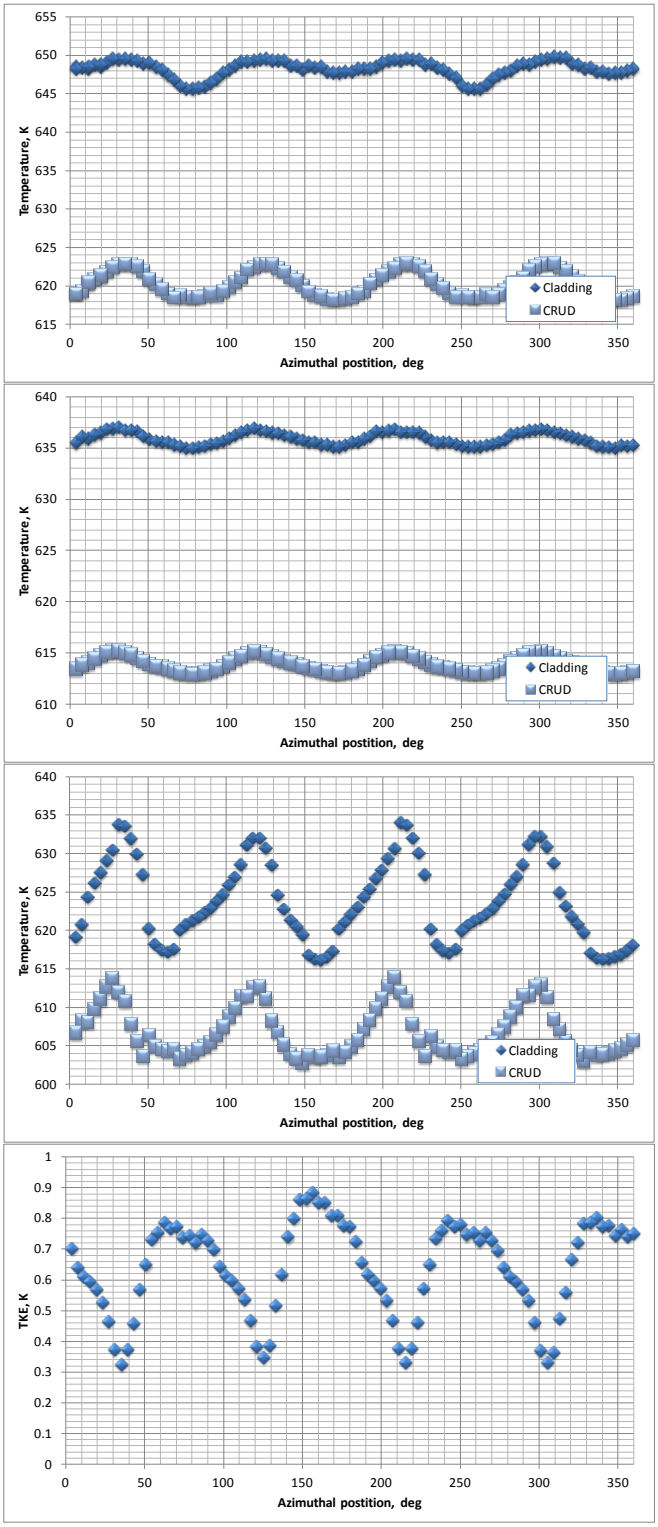

Figure 48 Azimuthal cladding and crud surface temperatures (a) before spacer (b) at the spacer (c) after spacer, and (d) turbulent kinetic energy in the boundary layer after grid spacer - spacer 2. Results at t =100 days.

(a)

(b)

(c)

(d)

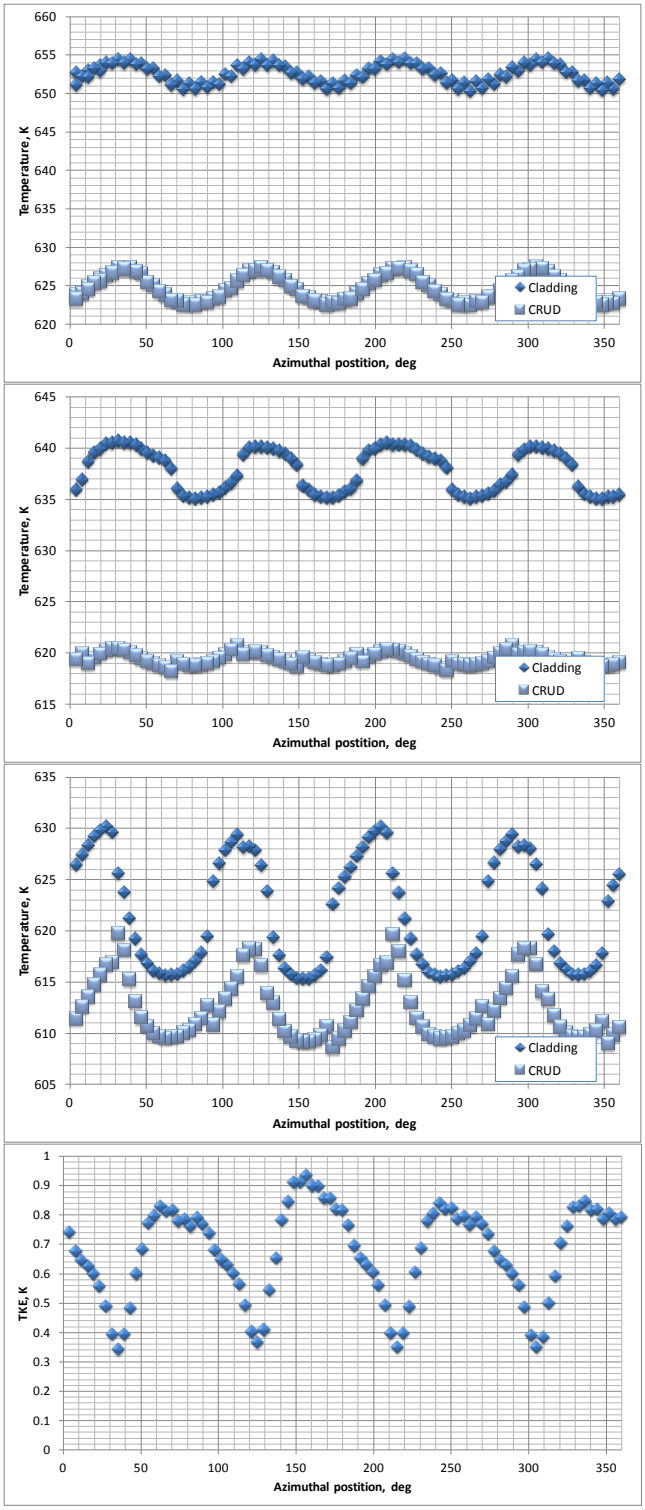

Figure 49 Azimuthal cladding and crud surface temperatures (a) before spacer (b) at the spacer (c) after spacer, and (d) turbulent kinetic energy in the boundary layer after grid spacer - spacer 3. Results at t = 100 days.

Results at t = 200 days

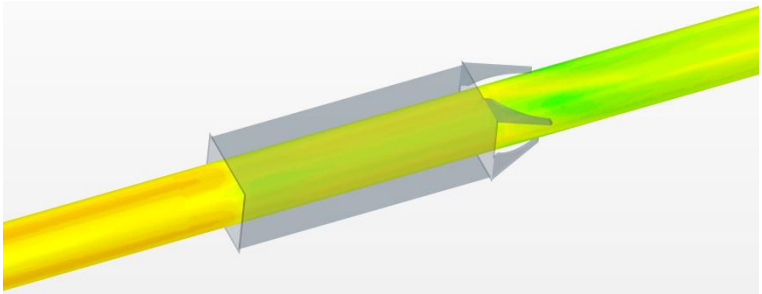

Spacer 1

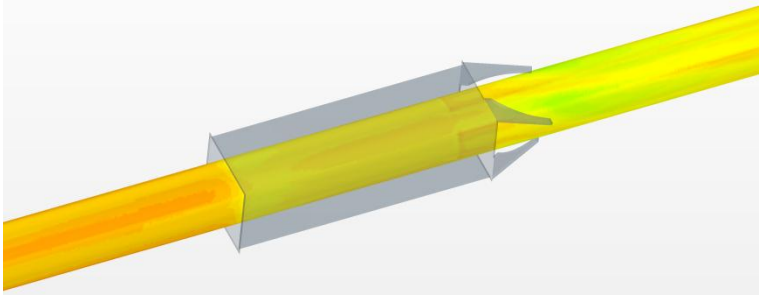

Spacer 2

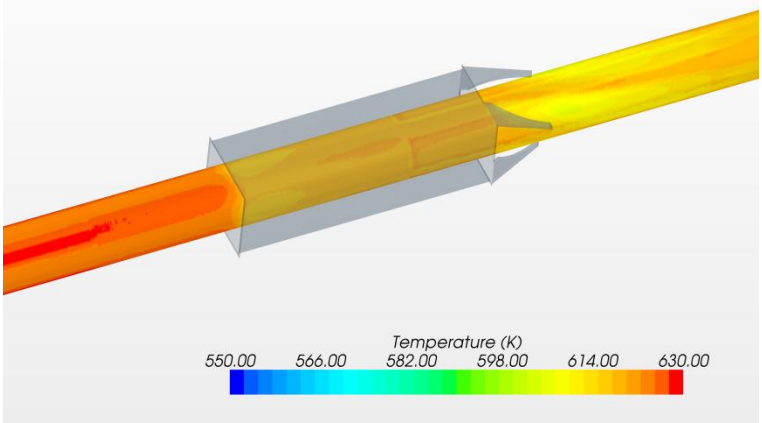

Spacer 3

Figure 50 Crud surface temperature at 200 days

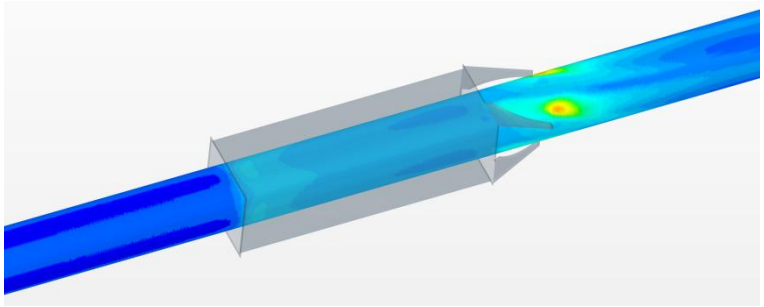

Spacer 1

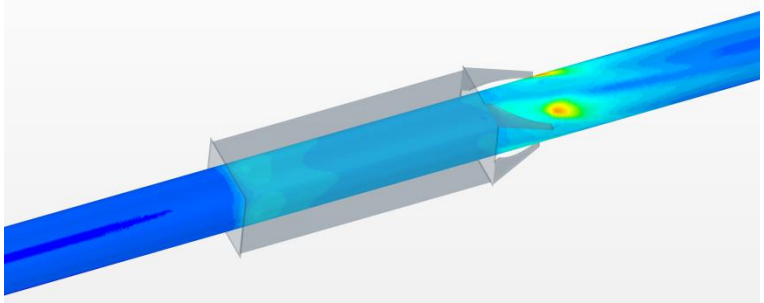

Spacer 2

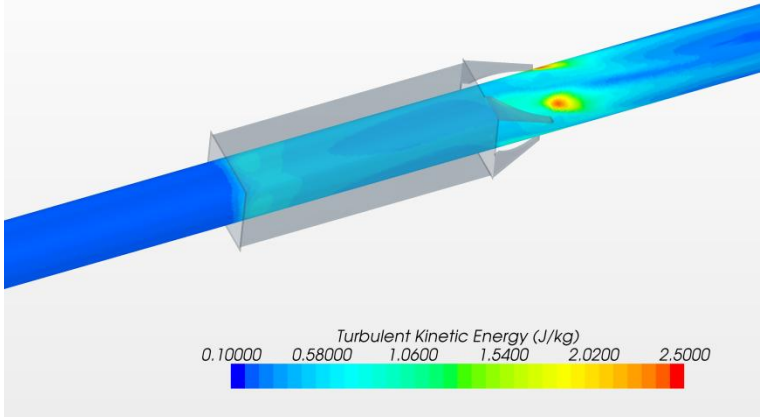

Spacer 3

Figure 51 Turbulence kinetic energy in the boundary layer at 200 days

(a)

(b)

(c)

(d)

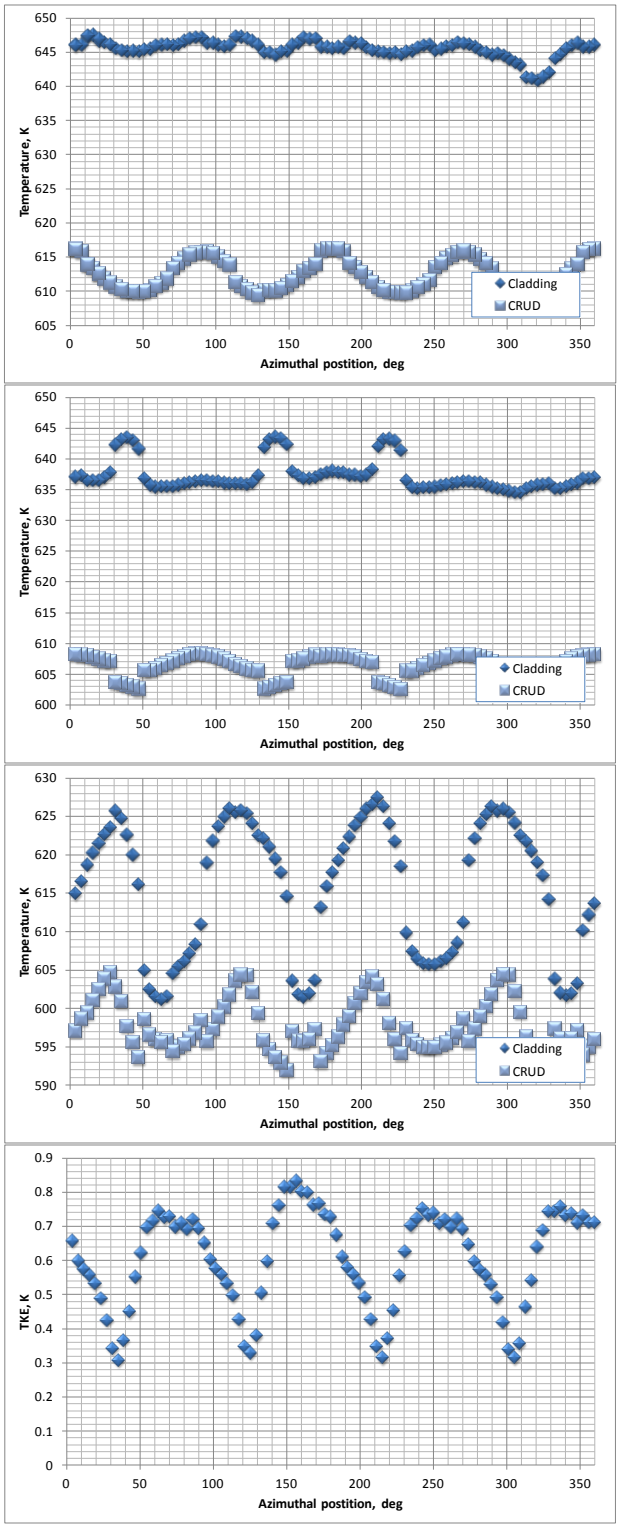

Figure 52 Azimuthal cladding and crud surface temperatures (a) before spacer (b) at the spacer (c) after spacer, and (d) turbulent kinetic energy in the boundary layer after grid spacer - spacer 1. Results at t = 200 days.

(a)

(b)

(c)

(d)

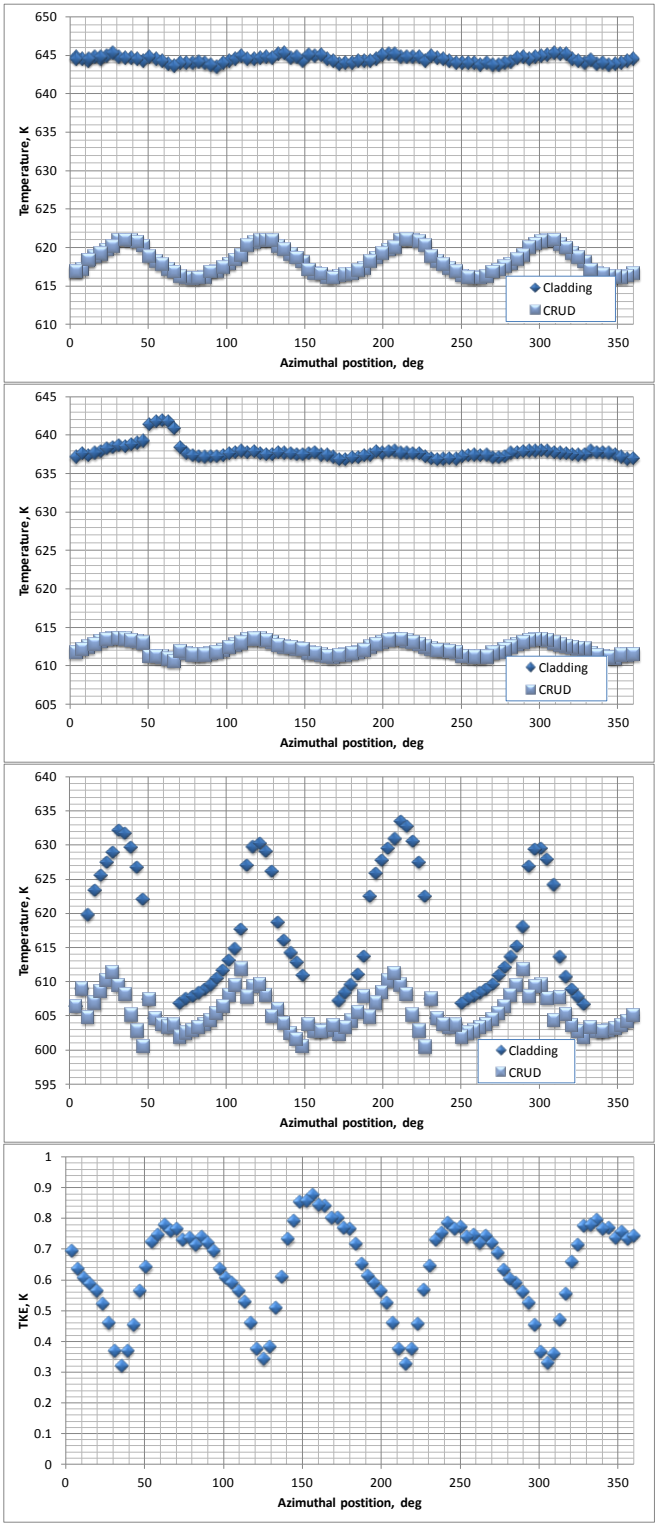

Figure 53 Azimuthal cladding and crud surface temperatures (a) before spacer (b) at the spacer (c) after spacer, and (d) turbulent kinetic energy in the boundary layer after grid spacer - spacer 2. Results at t =200 days.

(a)

(b)

(c)

(d)

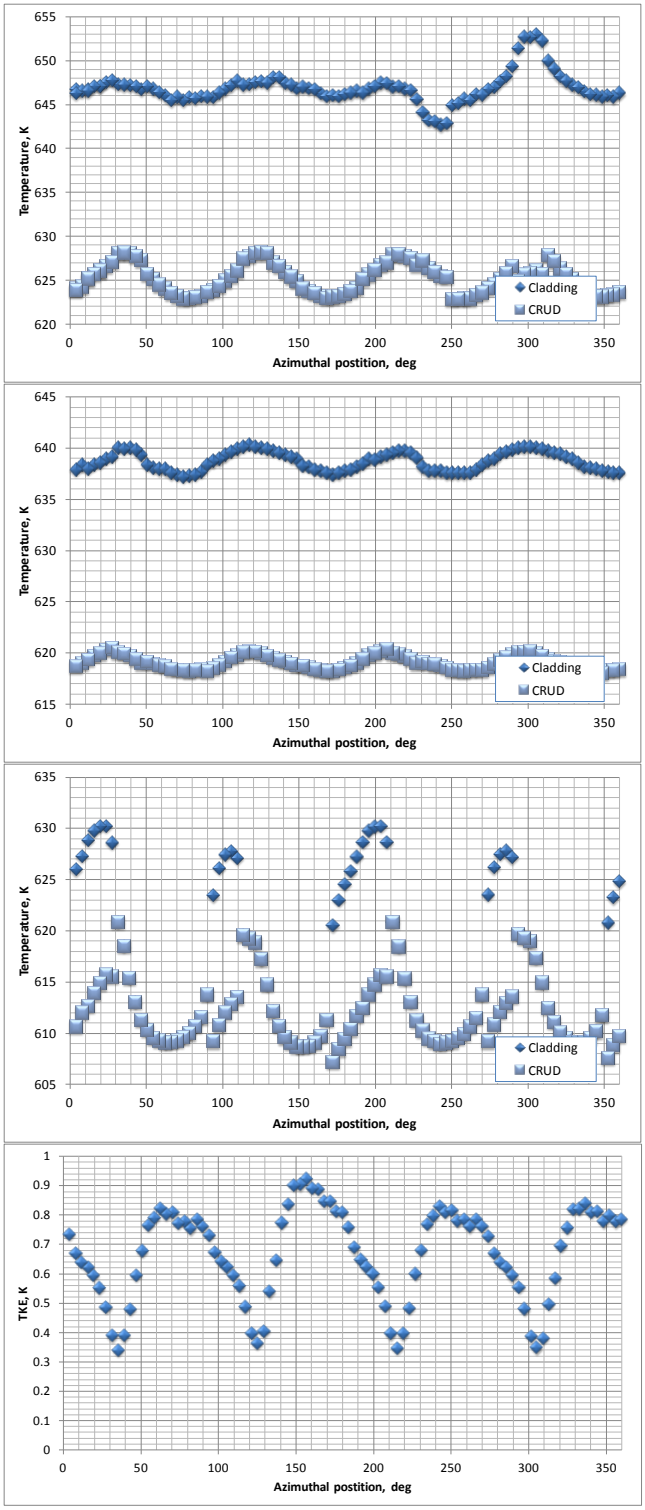

Figure 54 Azimuthal cladding and crud surface temperatures (a) before spacer (b) at the spacer (c) after spacer, and (d) turbulent kinetic energy in the boundary layer after grid spacer - spacer 3. Results at t = 200 days.

Results at t = 300 days

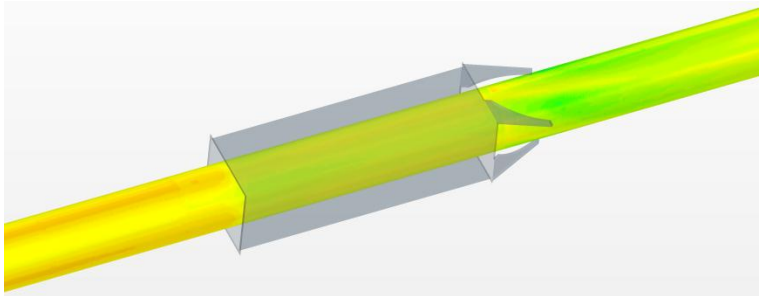

Spacer 1

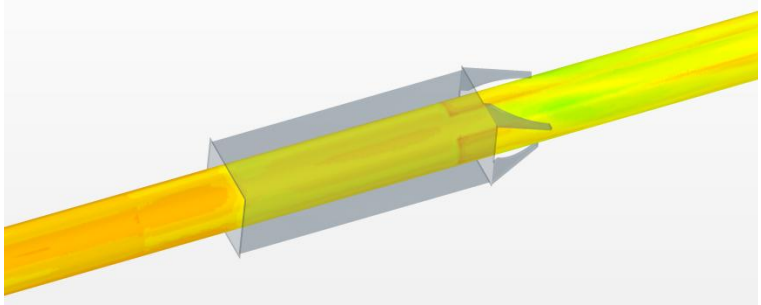

Spacer 2

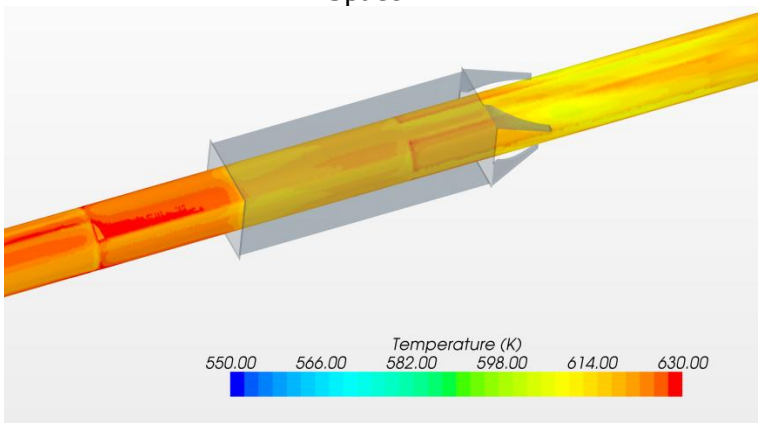

Spacer 3

Figure 55 Crud surface temperature at 300 days

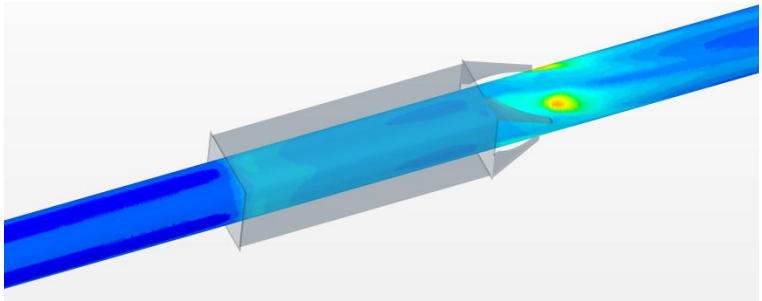

Spacer 1

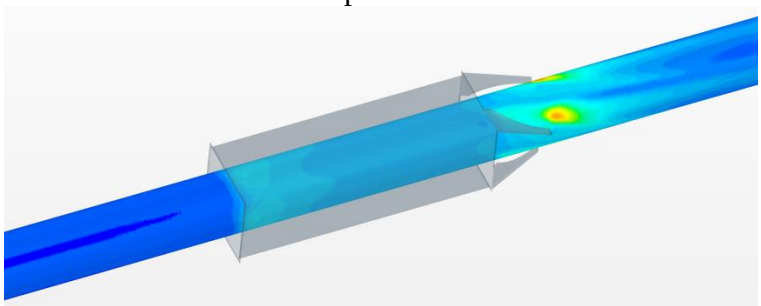

Spacer 2

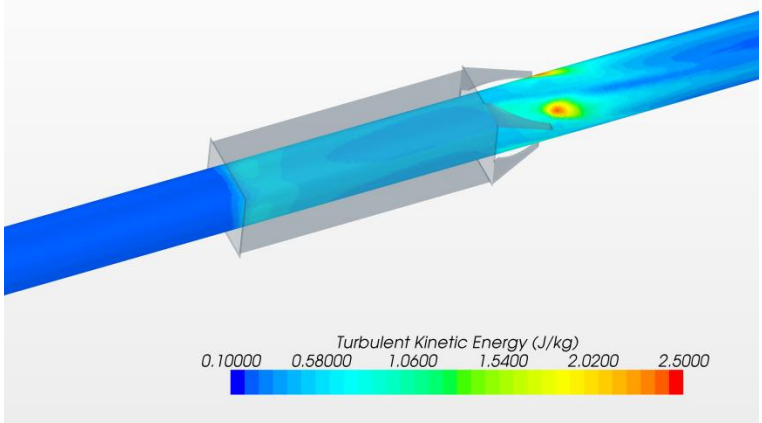

Spacer 3

Figure 56 Turbulence kinetic energy in the boundary layer at 300 days

(a)

(b)

(c)

(d)

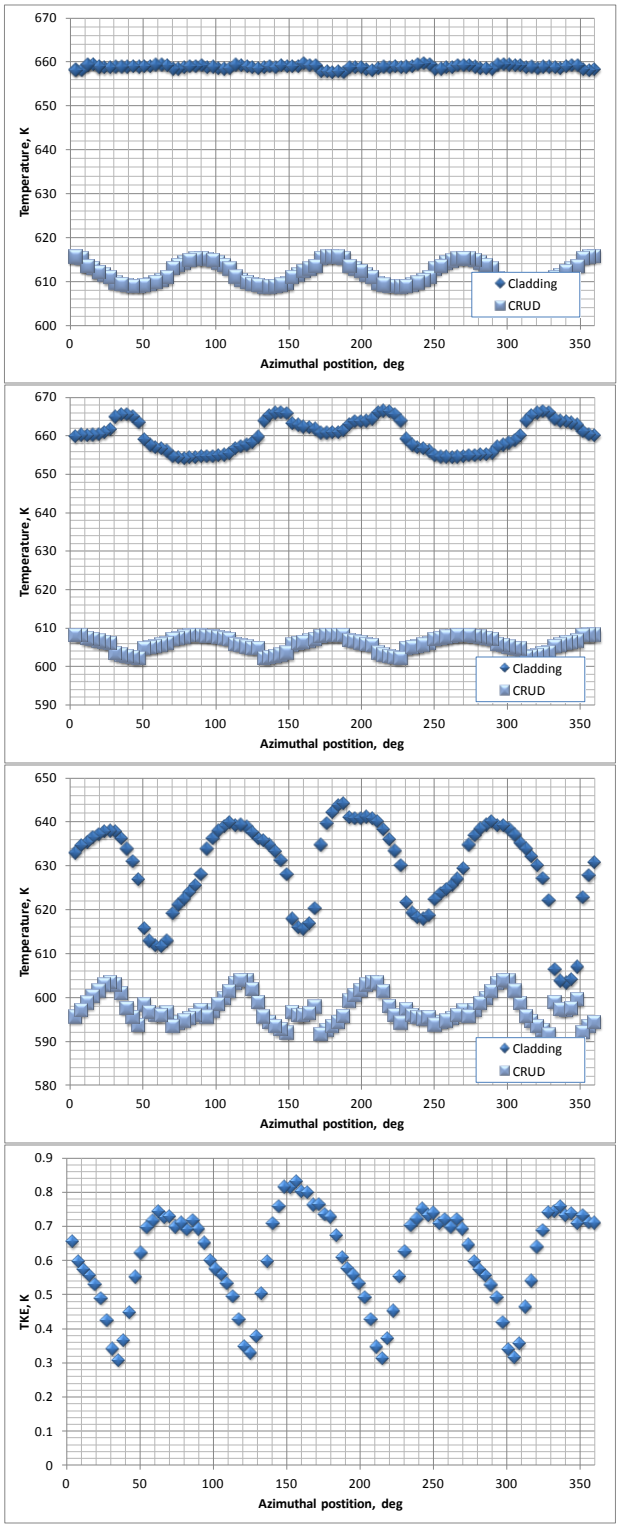

Figure 57 Azimuthal cladding and crud surface temperatures (a) before spacer (b) at the spacer (c) after spacer, and (d) turbulent kinetic energy in the boundary layer after grid spacer - spacer 1. Results at t = 300 days.

(a)

(b)

(c)

(d)

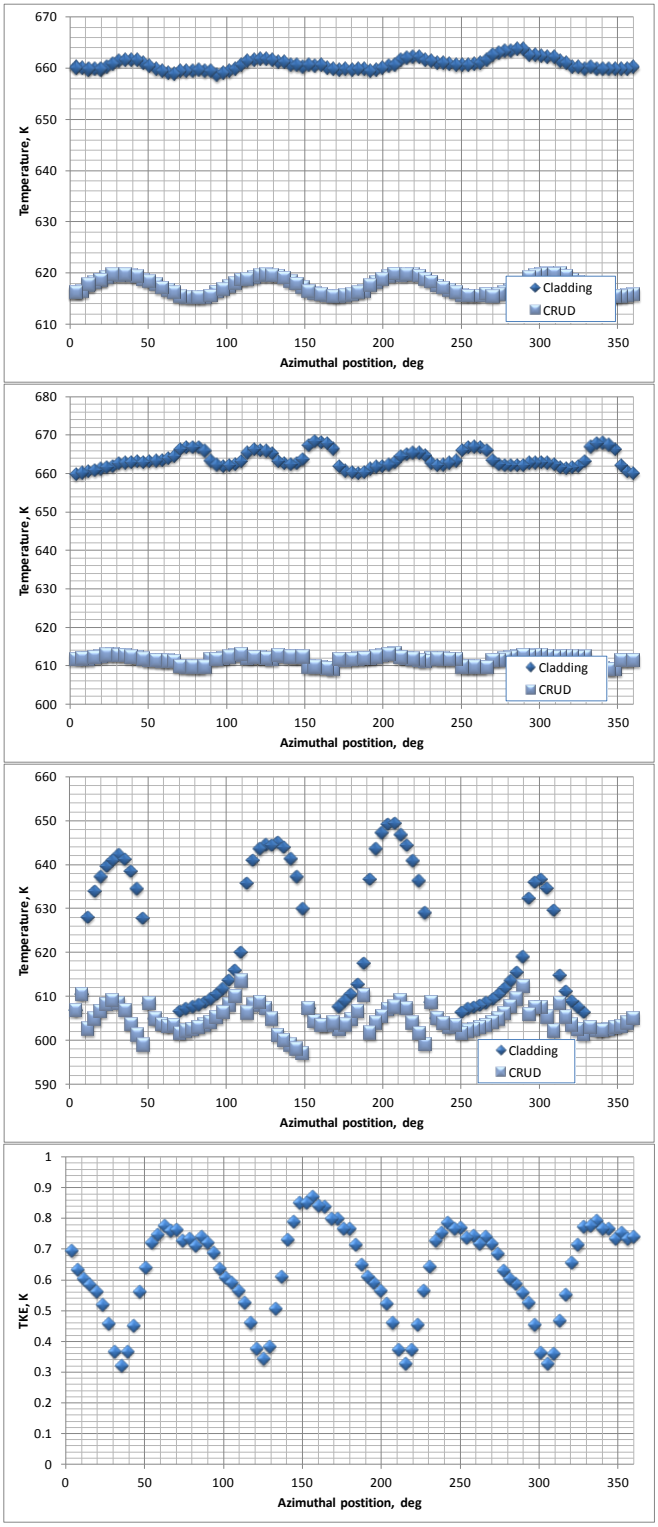

Figure 58 Azimuthal cladding and crud surface temperatures (a) before spacer (b) at the spacer (c) after spacer, and (d) turbulent kinetic energy in the boundary layer after grid spacer - spacer 2. Results at t =300 days.

(a)

(b)

(c)

(d)

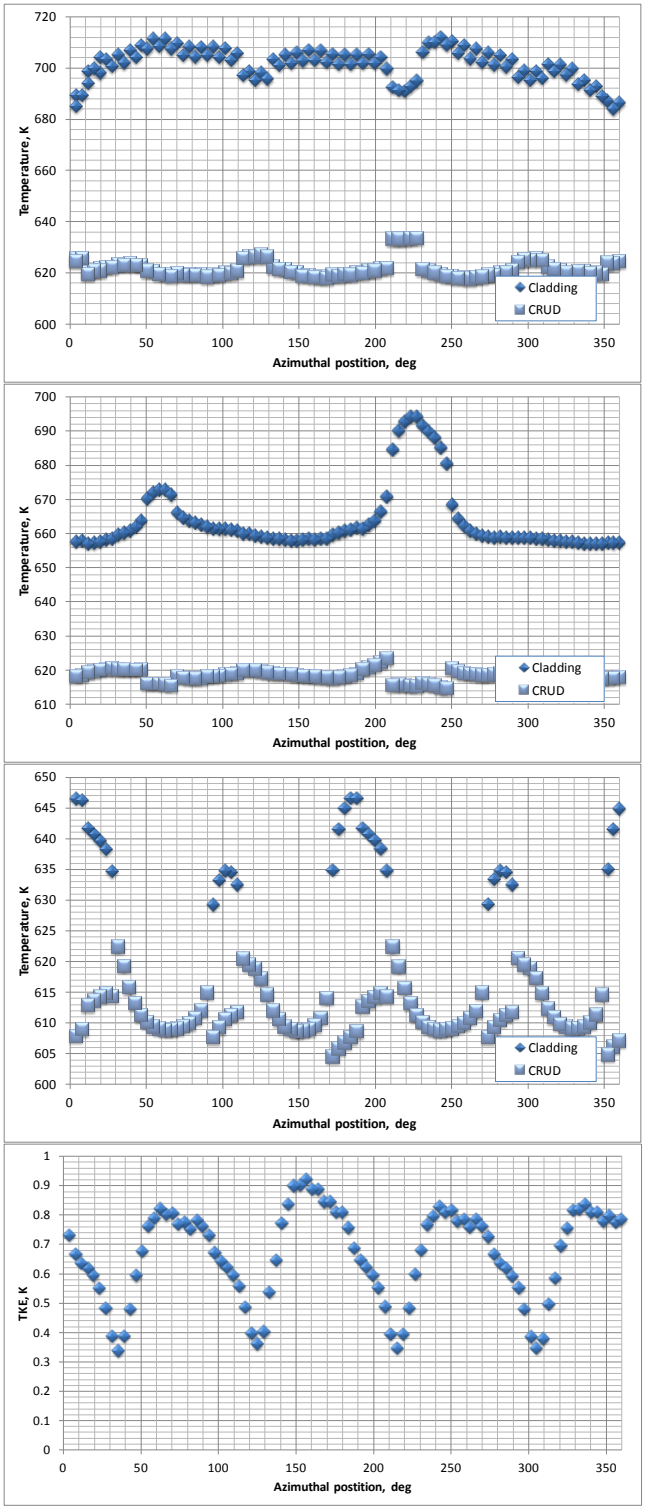

Figure 59 Azimuthal cladding and crud surface temperatures (a) before spacer (b) at the spacer (c) after spacer, and (d) turbulent kinetic energy in the boundary layer after grid spacer - spacer 3. Results at t = 300 days.

Results at t = 400 days

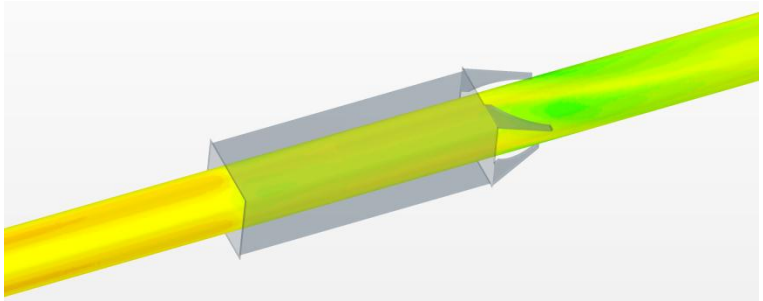

Spacer 1

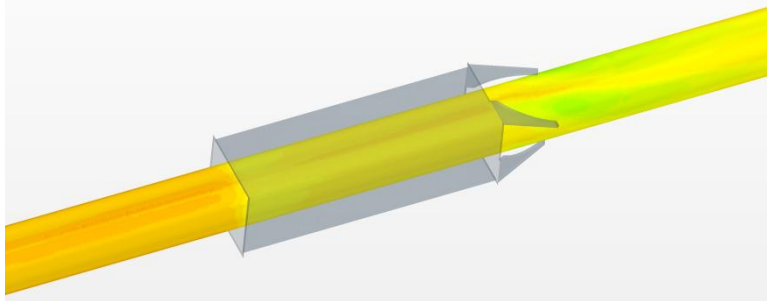

Spacer 2

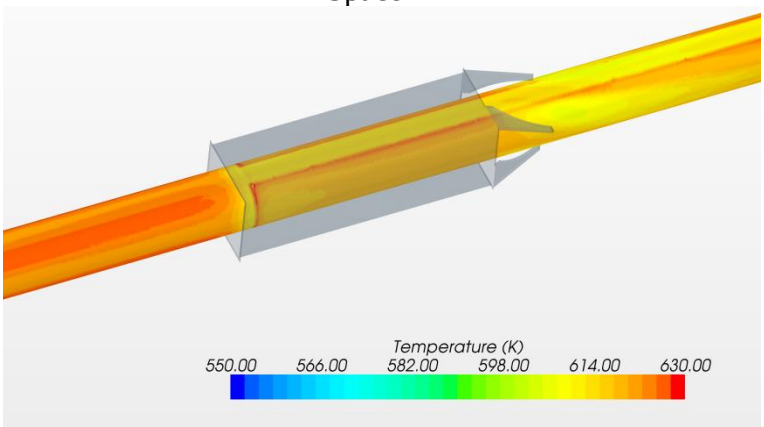

Spacer 3

Figure 60 Crud surface temperature at 400 days

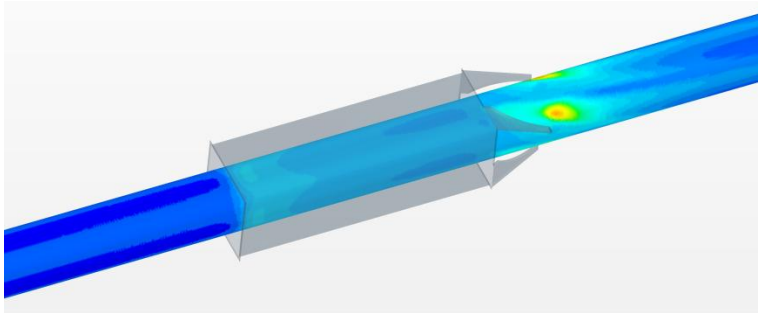

Spacer 1

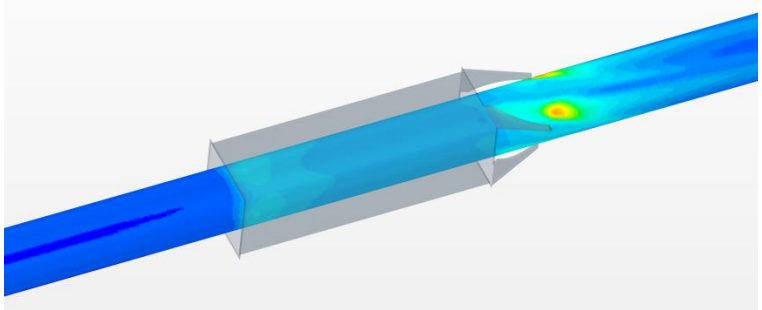

Spacer 2

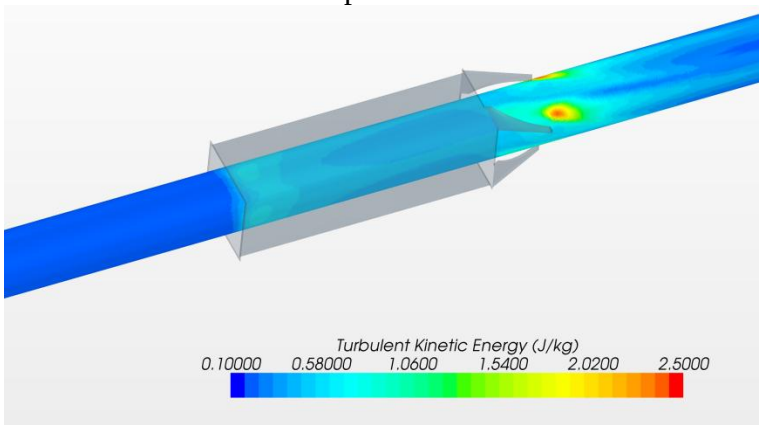

Spacer 3

Figure 61 Turbulence kinetic energy in the boundary layer at 400 days

(a)

(b)

(c)

(d)

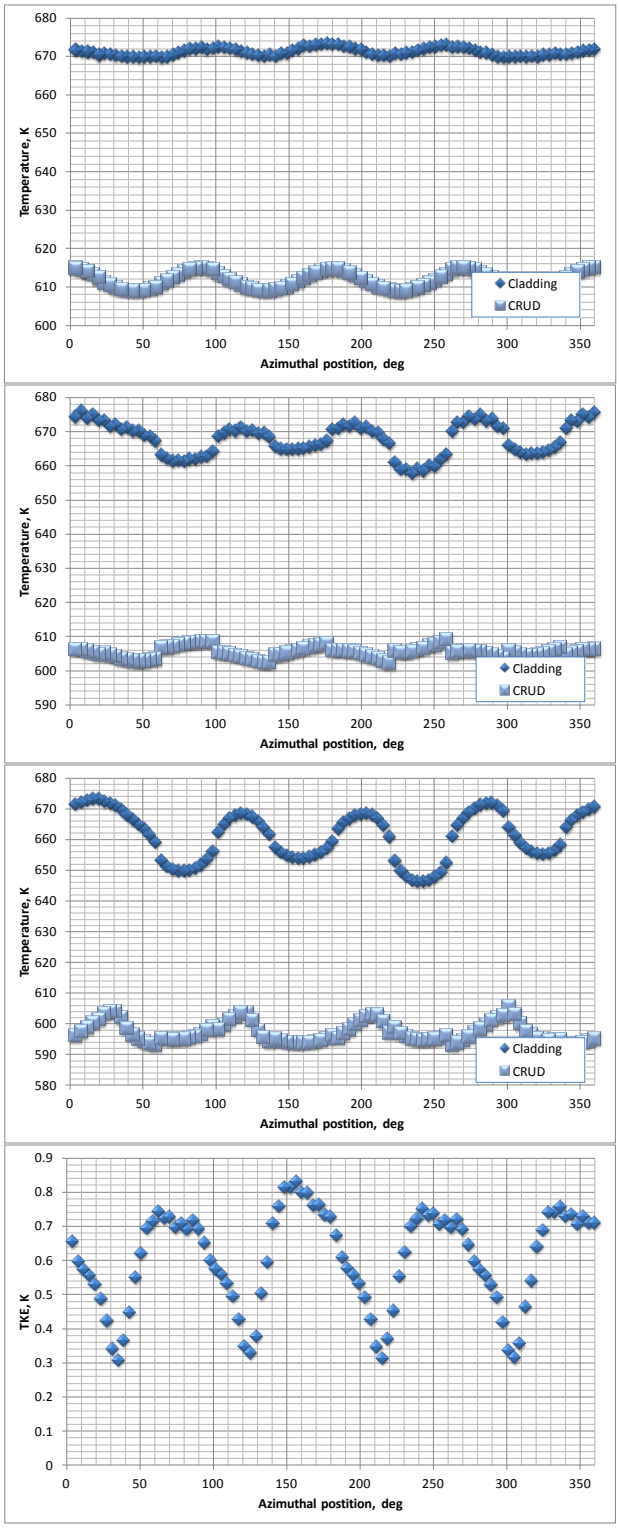

Figure 62 Azimuthal cladding and crud surface temperatures (a) before spacer (b) at the spacer (c) after spacer, and (d) turbulent kinetic energy in the boundary layer after grid spacer - spacer 1. Results at t = 400 days.

(a)

(b)

(c)

(d)

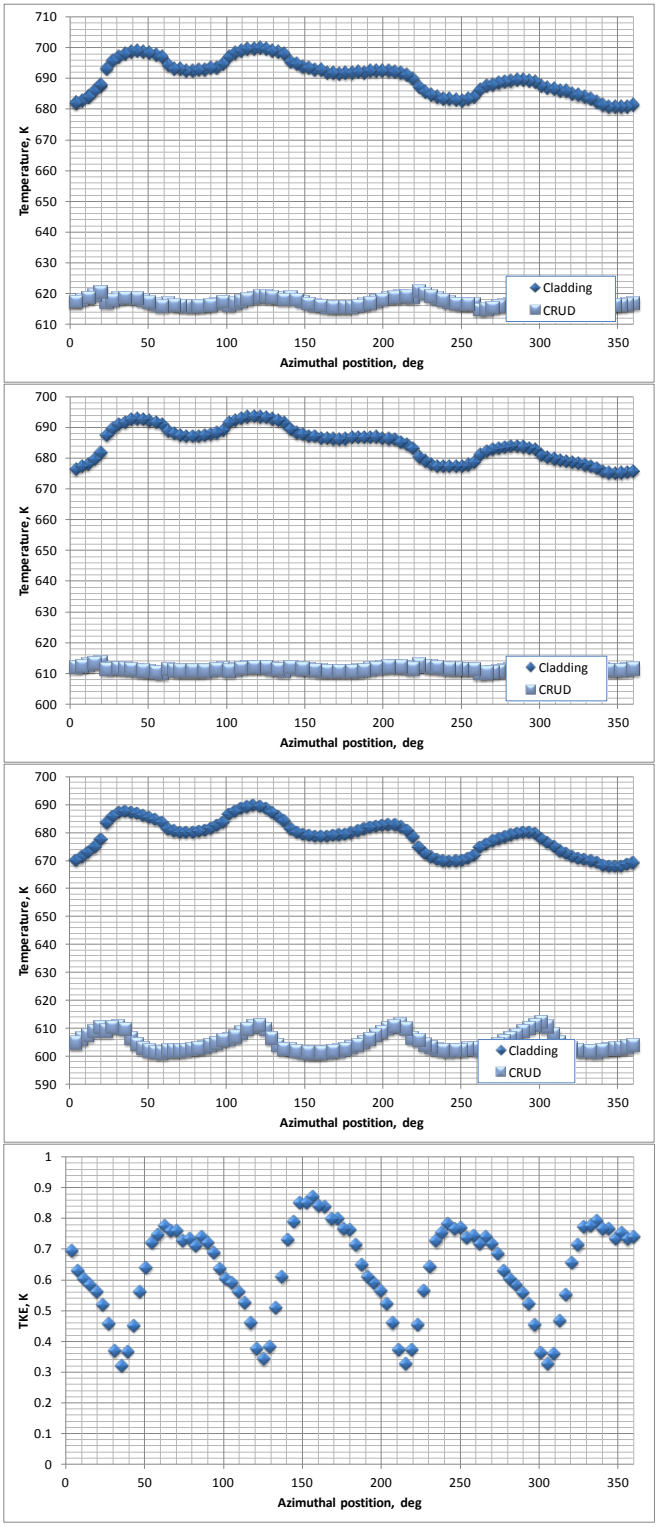

Figure 63 Azimuthal cladding and crud surface temperatures (a) before spacer (b) at the spacer (c) after spacer, and (d) turbulent kinetic energy in the boundary layer after grid spacer - spacer 2. Results at t =400 days.

(a)

(b)

(c)

(d)

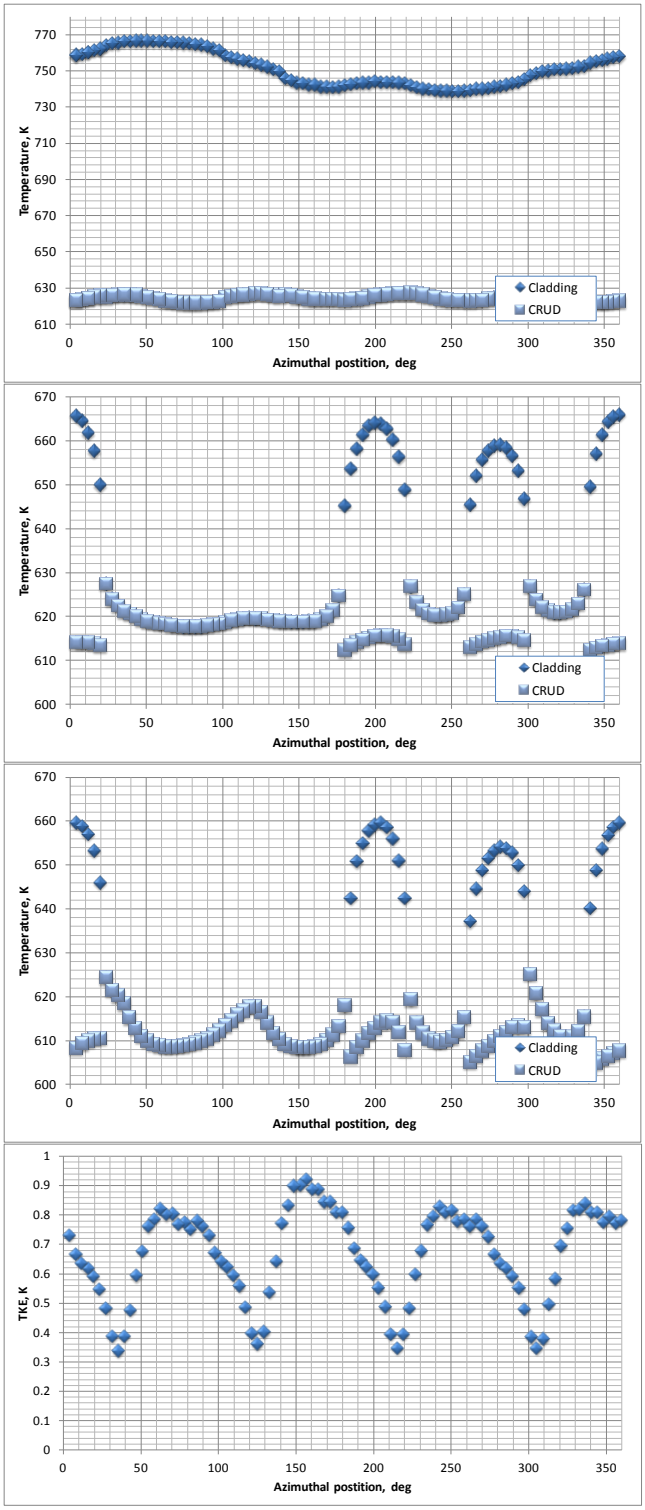

Figure 64 Azimuthal cladding and crud surface temperatures (a) before spacer (b) at the spacer (c) after spacer, and (d) turbulent kinetic energy in the boundary layer after grid spacer - spacer 3. Results at t = 400 days.

APPENDIX 2 - DeCART results

Case B with Boron Letdown Model

The case B resolution is described in Table 4. In this case, the azimuthal discretization in MAMBA is 20 degrees rather than 40 degrees (as in case 1) during the 300-400 day range of the depletion cycle.

The axial offset anomaly magnitudes of the higher and lower resolution cases at 350 days are compared in Figure 65. Case 2 with crud shows a reduction in the magnitude of the AOA at the 350 days depleted state point; (300 days used the lower resolution MAMBA data, so it is the same magnitude). Despite the reduced AOA, the power axial power distributions comparing cases 1 and 2 show that the profile shape is more distorted. It further develops the peaks and valleys—moving further from the common "double-humped" profile seen at end of cycle to a "triple-humped" profile. This development is seen in Figure 66 which compares case 1 and 2 at 350 days depleted. The triple-humped profile is more pronounced in Figure 67, comparing the power profiles at 400 days.

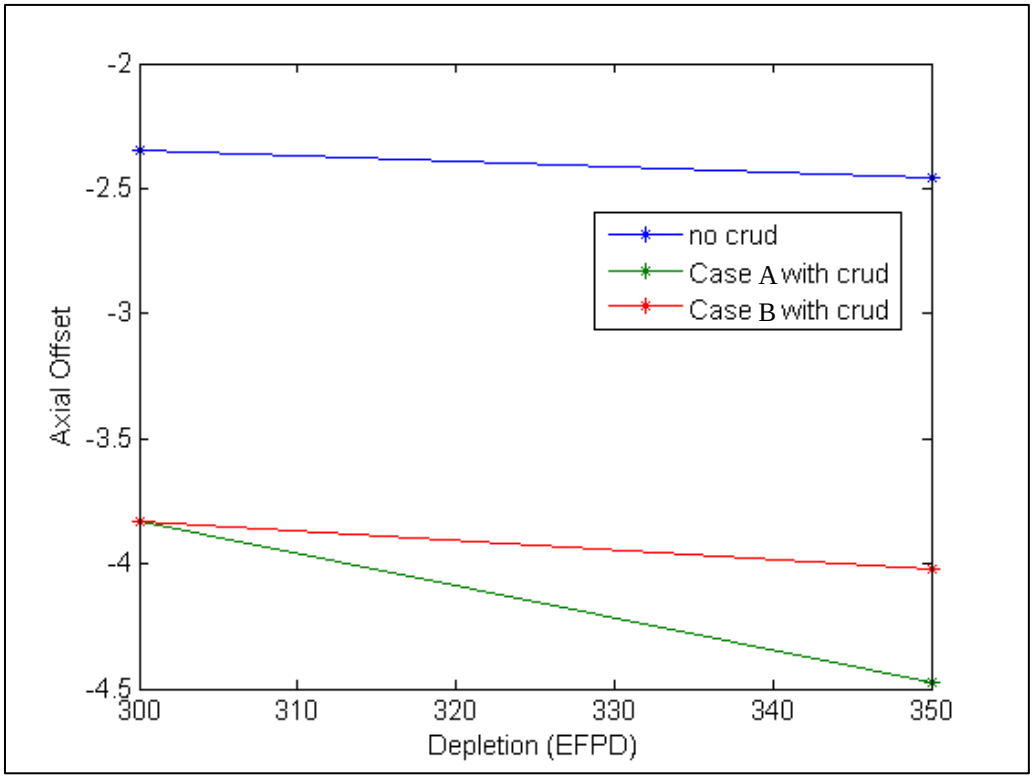

Figure 65 AOA comparison of effect of MAMBA mesh resolution on the AOA magnitude at 350 days depleted.

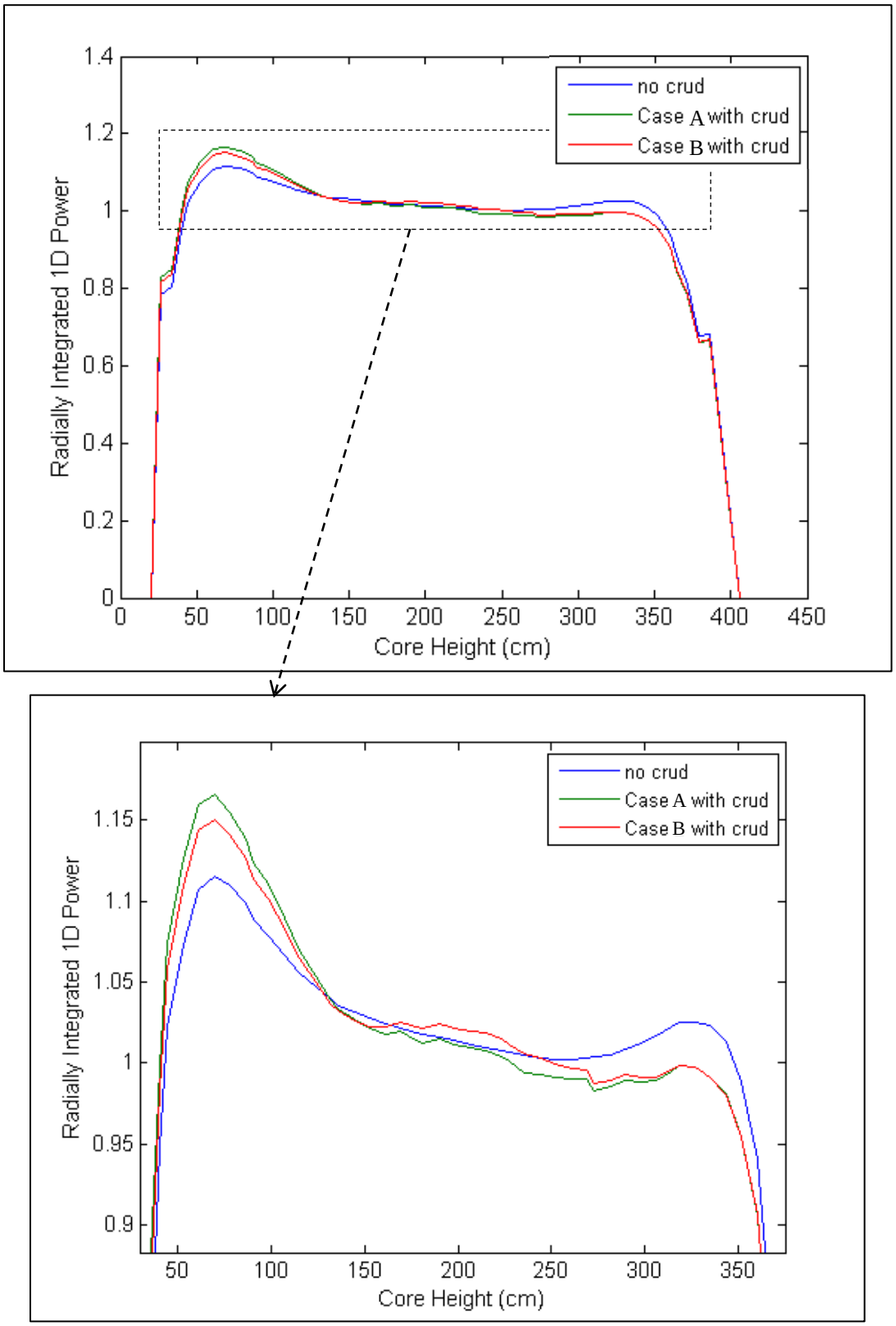

Figure 66 Axial power profile comparison at 350 days of the no crud and two different cases representing to different MAMBA meshes.

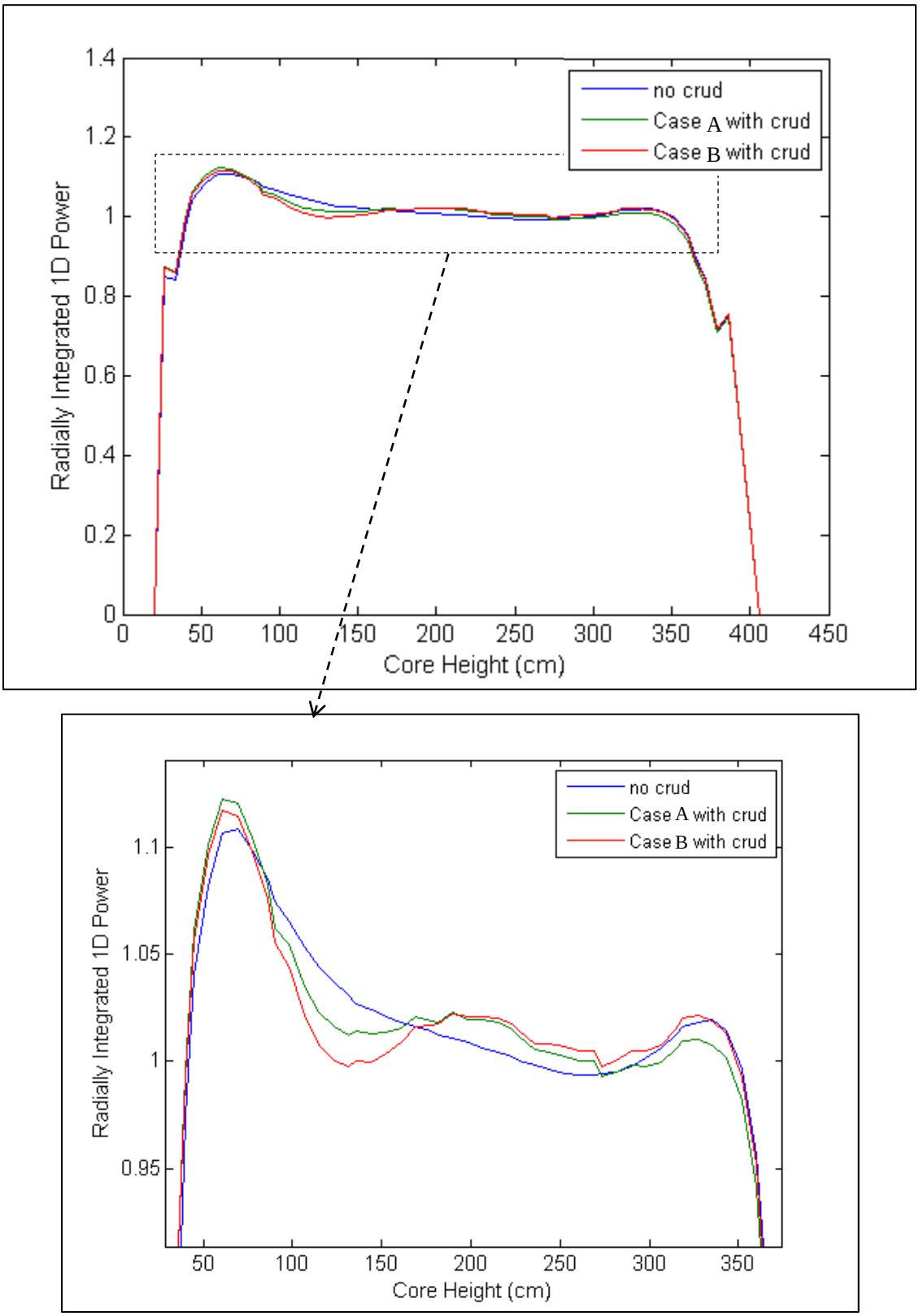

Figure 67 Axial power profile comparison at 400 days of the no crud and two different cases representing to different MAMBA meshes.